Confirmation of Sgr A* Using the Event Horizon Telescope Data as Extreme Binary of the Supermassive Black Holes Concluded by Decameter Radio Wave Pulse Observations

Hiroshi Oya*

Geophysical Department, Graduate School for Science, Tohoku University and Space and Astrophysics Research Task, Seisa University, Japan.

*Corresponding Author
Hiroshi Oya, Geophysical Department, Graduate School for Science, Tohoku University and Space and Astrophysics Research Task, Seisa University, Japan.

Abstract
We analyzed the time variation of the visibilities in the publicly released event horizon telescope (EHT) data provided by the EHT Collaboration, who carried out observations of Sgr A on April 6 and 7, 2017. The EHT consists of the 1.3 mm wavelength very long baseline interferometry (VLBI) system associated with globally distributed six stations with eight antennas. The analyses were not intended to make image of Sgr A*; instead, we searched for periodic time variations in the observed individual baseline data of the EHT by applying a method to compare with the model visibility, for 1.3 mm VLBI detection that was constructed to reflect the effects of the supermassive black hole binary (SMBHB) concluded from the study on the observation of the decameter radio wave pulses from Sgr A*. The SMBHB, orbiting with a period of 2200 ± 50 sec and an orbit size of 4.1×10^7 km, is observable with an observation angle width of 32.6 μas in a plane nearly parallel to the Galactic equatorial plane. After confirming the possible correspondence between the visibilities of EHT data and constructed model via direct comparison in real-time space, we applied the modified Fourier transformation to confirm the coincidence between observation data and model visibilities. The modified Fourier transformation was uniquely restructured in this paper to eliminate the artificially modulated data sampling time interval by utilizing Fourier transformation of the random noises distributed over time synchronized with data sample timing of the EHT data. We identified significant periodic time variations in the radiation within a range below 70 μas with an orbiting period of 2193.3±27.5 sec that is associated with an eclipse cycle period of 1096.5 sec caused by the SMBHB orbiting motion.*

1. Introduction

Studies on the time variation of radio wave fluxes from Sgr A* have expanded, starting from investigations of the intermittently occurring flares detected by millimeter-range radio wave telescopes [1-4]. In time variation studies in millimeter range wavelength radio wave fluxes, short time variations with periods ranging around half hour have gradually emerged in the Sgr A* emissions not only in times of flare as well as in the quiescent structure [5,6], suggesting some periodicity [7].

Alongside the studies of time variations of SgrA* by observations of radio telescope including the very long baseline interferometry (VLBI), decameter wavelength radio wave pulse (DRWP) observations of Sgr A* have been continued since 2000. These observations seek to identify the spin signatures of the event horizons of possible supermassive black holes [8]. The DRWP observations at 21.86 MHz are characterized by lowness of observation frequencies, of radio waves, which allow to identify source positions extremely close to the event horizon

of rotating Kerr black holes where the time passage becomes slow through the effects of general relativity. The observation frequency is much lower than the plasma frequencies surrounding Sgr A*. Due to the structured magnetic field in the plasma environment around Sgr A*, DRWPs can propagate in the form of whistler mode waves; these can be converted into ordinary mode radio waves at suitable points satisfied by the plasma environment conditions. This is commonly understood in the field of planetary radio-wave science [9-15]. Inhomogeneous emission intensities at the source points of decameter radio-waves become the origin of pulses coinciding with the spin period. In 2019 [8], the first principal results were published stating the detection of two kinds of DRWPs with intrinsic pulse periods of 173±1 and 148±1 sec, exhibiting sinusoidal variations with a common period of 2,200 ± 50 sec. By attributing the pulses periods to spin periods of two Kerr black holes (BHs) together with other parameters related the orbital motions[8] , we posited the existence of two supermassive BHs. Using the physics of Kerr space time and orbital theory for a binary system with an

orbital period of 2,200 ± 50 sec,the BH masses were deduced; these BHs were temporarily called Gaa and Gab with masses of $(2.27\pm0.02)\times10^6$ $M_\odot$ and $(1.94\pm0.01)\times10^6$ $M_\odot$,respectively (resulting in a total mass of $(4.21\pm0.03)\times10^6$ $M_\odot$). The orbital velocities of Gaa and Gab were measured from the Doppler effects as 18% and 22%, of the speed of light, respectively.

In terms of confirming the results of the DRWP observations, the key issue is whether gravitational waves are radiated from the SMBHB or not. To this end, we published a theoretical result in 2023 [16]; the matter distribution of the extremely high-energy and dense plasma inside a supermassive rotating BH was theoretically investigated. For a model of equal-rotation velocity of matter, where the main component of plasma rotates around a common axis at a constant velocity close to the speed of light; that is, with a high Lorentz factor (gamma rate), the matter distribution is condensed to a region with a much smaller radius than that of the event horizon in Kerr spacetime. The gravitational waves generated from the condensed matter region ,via orbital motion of the binary, return towards the source after halting at the critical sphere in the vacuum region of the spinning Kerr spacetime. When returning waves encounter the outgoing ones, the gravitational waves are deformed to standing waves that carry no energy beyond the event horizon. We concluded that no gravitational waves are radiated from the supermassive BH binary (SMBHB).

However, it has not yet been experimentally confirmed whether gravitational waves are generated from SMBHBs or not. It is extremely important to confirm the presence of a SMBHB concluded from DRWP observations by comparison to the data observed by millimeter wavelength VLBI, that can approach to the sources size equivalent to the possible orbit of investigating SMBHB. To this end, our first study has been made taking the approach to the 1.3mm wavelength VLBI results by Fish et al observed in 2009 [5]; we have interpreted the observed data via the orbiting effects of the existing SMBHB [17]. Because the objects observed by DRWP observations and 1.3 mm radio-wave VLBI systems provide different categories of observation data, we constructed the model visibility (DRWP-Model) according to SMBHB parameters obtained via DRWP observations [8], to facilitate comparison against the amplitudes of the visibility data observed via the 1.3 mm radio-wave VLBI system, as reported by Fish et al. The concept of a variation with short characteristic time (VSCAT) for millimeter-range radio waves from Sgr A* is clarified by this work [17] ; and it is concluded that the VSCAT exhibits a period of 2150±2.5 sec; this is consistent with the orbital period of SMBHB proposed by the DRWP study.

As the second step towards confirmation of the proposed SMBHB, we are allowed to approach to the publicly released observation data of the event horizon telescope (EHT) project. As far as we understand, the establishment of EHT activities were based on the work of Fish et al. [5]; through 1.3 mm wavelength VLBI observations, which are characterized by a resolution of a few 10 μs , approaching to the imagined Schwarzschild radius, at SgrA*,corresponding to 4.28×10^6 $M_\odot$ [18].

Succeeding to an image of the event horizon of the super-massive BH M87* at the center of the elliptical galaxy in the Vir-go constellation[19-24], the EHT collaboration (EHTC) has reported the image of the BH shadow of Sgr A*, at the center of the Milky Way Galaxy [25-30]. The image of Sgr A* was published in 2022, three years after the release of the image of M87* shows a single BH shadow associated with a bright ring; it closely resembles the M87* image. The present study was regretfully unable to accept this image without resolution to the serious two problems. The first problem is that the image of Sgr A* is essentially identical to that of M87* which has been pointed out by Miyoshi et al. [31] as to be erroneous; they indicated that a portion of the BH shadow is an artifact result produced by a lack of visibility data corresponding to the visible angle of the BH shadow around 40 μas. The second problem is discussed in the present study: it is the problem of the time variation of the observed visibilities. During the gap period of about three years between the reports of the two BHs M87* and Sgr A*, it has been currently told that the difficulties of taking images of the shadow of Sgr A*, which is subjected to complicated time variations in the VLBI visibilities [32], are attributable to the intense scattering of radio waves by electron turbulence in dense plasma. In this situation, it seems that the EHTC avoids the time variation by applying a method to mitigate the variability in the data [26,27] and arrive at a static image of a single BH. There are, however, research activity concerning about time variation of radiations around Sgr A*; by Wielgus et al. [33], a detailed investigation of the spectra of the time variation for 1.3 mm wavelength radiation are performed from the perspective of variations exhibiting widely distributed characteristic times in the Sgr A* emissions. Wielgus et al. [34] also reported upon the orbital rotation of hot plasma spots with periods of ~4200 sec in the inner accretion region around the imagined single BH, associated with flares of Sgr A*. We understand that these types of time variation commonly occur around Sgr A* but do not persist as the effects of orbiting SMBHBs.

The aim of the present study is, therefore, to investigate the VS-CATs from the perspective that VSCATs are not only random variations caused in generation processes and through the propagating paths of mm wavelength radio-waves, owing to the turbulent plasma media; that is, we seek VSCATs produced by the orbital motions of SMBHBs [17]. To confirm the orbital motion of the SMBHB, with a period of 2,200 ± 50 sec, as concluded by the DRWP observations [8], we try to identify the periodicity in the observation results from the 1.3 mm-radio-wave VLBI system, which have been provided by the EHTC as public data [35].

In analyzing the EHT visibility data (hereafter, EHT-Data), we do not use for mapping the radio source onto (u,v) coordinates but instead analyze the time variation for individual EHT baselines. Because objects observed by DRWP observations and 1.3 mm radio wave VLBI systems are not identical, we construct the model visibility (DRWP-Model) from the SMBHB parameters concluded via DRWP observation [8], to compare them with the visibility data observed by the 1.3 mm-radio-wave VLBI system. The details of the DRWP-Model construction are presented in Sec. 3.

The EHT-Data and DRWP-Model are compared in two fundamental ways. The first is the method of direct correlation between the EHT-Data and DRWP-Model, as described in Sec. 5. Because of the low signal-to noise ratio and intermittent sampling of the EHT-Data, the confirmation of the coincidence

between the EHT-Data and DRWP-Model is limited to within a given range of coincidence index; however, we can confirm that a certain range of the correlation index that reveal the orbital motion of the SMBHB. We take this direct comparison as a guide for searching for SMBHB effects within the EHT-Data. The second way of the comparison is the use of the Fourier transformation. To more effectively confirm the orbital motion of the SMBHB, we employ a Fourier transformation for both the EHT-Data and DRWP-Model, as described in Secs. 6 and 7. The original EHT-Data released to the public consisted of data which are intermittently sampled by switching between periods of observation and calibration with a period of around 1000 sec to 1100sec, meanwhile, the present work is intending to search for phenomena with a period of around ~1100 sec and a period of double that. To compensate for this problem of the intermittent "data sampling time window" (hereafter, DSTW) in the results of the Fourier transformation, we have employed method of compensation of the (DSTW) applying Fourier transformations to groups of random noises whose time series are synchronized with that of the EHT-Data (quasi-random noise synchronized with the EHT-Data series; hereafter, QRN-EHT), along with Fourier transformations of the EHT-Data and DRWP-Model which is also sampled under DSTW constraints.

As details are presented in Secs.6 and 7, we can eliminate the effects of intermittent data sampling upon the results of the Fourier transformation, by dividing these results by the Fourier-transformed results for the QRN-EHT, hereafter referred to as the modified Fourier transformation (MDFT). After eliminating the effect of the DSTW, we compare the results with those for the MDFT of the EHT-Data for the corresponding baseline VLBI pairs, with the MDFTs of the DRWP-Model to identify the orbiting period of the possible SMBHB.

The key principle maintained throughout this comparison is that we never change the physical parameters obtained from the DRWP observations, in terms of physics matters such as the orbiting period range (2200±50 sec), orbiting speed, and size of orbits; the only thing we do change is the tilt of the orbital plane in the direction perpendicular to the observation direction, which cannot be determined from the DRWP observations. The adjustment of parameters in the DRWP-Model is only performed for numerical components, e.g., the amplitude (related to the
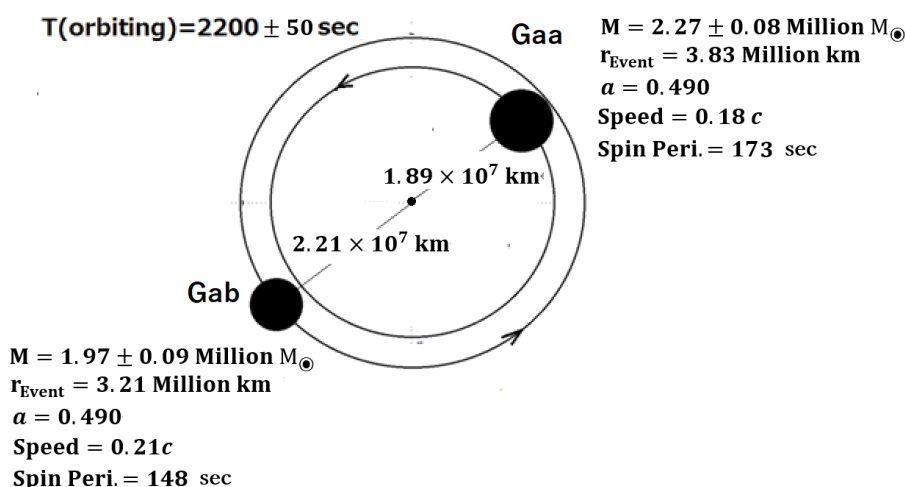
flux density), starting time used to determine the initial timing, and level in the model that is to satisfy the level of EHT-Data. The only exception to this is the sweeping of the SMBHB orbiting period; this sweep is not applied to identify a suitable period from the EHT-Data, but simply to confirm how well the DRWP-Model fits the EHT-Data.

2. Outlines of the DRWP [8] and EHT Observations [25–30]
2.1 Summary of DRWP observations [8]

Details of the DRWP observations and results were presented in the original paper [8], and a brief review was given in a related article [17]. We summarize the DRWP observations and results here, to construct a DRWP-Model suitable for comparison against the EHT-Data.

At Tohoku University by using a long baseline interferometer for decameter wavelength radio waves, consisting of three antenna sites with baseline lengths ranging from 44 to 83 km at 21.86 MHz, we observed the DRWPs from Sgr A* at our Galaxy's center, primarily in June 2016 and June 2017. Because of the extremely low signal to noise (S/N) ratio (i.e., the background noise levels were 300–500 times larger than the signal levels), the observed interferometer data were analyzed by applying a unique method to analyze the pulse components of signals from Sgr A*, the directions of which were detected using the Earth's rotation. Separation of the signal from the background noise was accomplished by applying the interferometer fringe function correlation method (see [8]), in which the aperture synthesis method for the interferometer data obtained from the Earth's rotation was modified to eliminate any local phase shift ambiguities in the system as well as phase shifts attributable to ionosphere propagation; this was performed by sacrificing phase information. Pulse forms in the signal were confirmed in the Fourier transformed domain by applying fast Fourier transform (FFT) operations to the time series data obtained via the interferometer fringe function method. By taking an average of the FFT results over 2016 independent sets, the pulse frequency spectra were discriminated from the background white noise. We denote the final FFT results, as separated from background noise, as the BH Code. The BH Code from the source within ±6 arc min of Sgr A* indicates two intrinsic pulse periods of 173±1 and 148±1 sec; which are

$T(orbiting) = 2200 \pm 50 \text{ sec}$

Gaa

$M = 2.27 \pm 0.08 \text{ Million M}_{\odot}$
$r_{Event} = 3.83 \text{ Million km}$
$a = 0.490$
$Speed = 0.18\,c$
$Spin\ Peri. = 173 \text{ sec}$

$1.89 \times 10^7 \text{ km}$

$2.21 \times 10^7 \text{ km}$

Gab

$M = 1.97 \pm 0.09 \text{ Million M}_{\odot}$
$r_{Event} = 3.21 \text{ Million km}$
$a = 0.490$
$Speed = 0.21c$
$Spin\ Peri. = 148 \text{ sec}$

Figure 1: Configuration of the SMBHB confirmed from the FFT spectra for the decameter wavelength radio waves from Sgr A*, assuming that the pulse frequencies are synchronized with the spins of SMBHs Gaa and Gab subjected to the Doppler effect produced via orbital motion. The distance between two SMBHs is 2.84 R_{ss} with respect to the Schwartzschild radius Rss if we assume a single BH.(After Oya [8,17])

subjected to a sinusoidally periodic modulation with common periods of 2,200±50 s. By attributing the detected pulses to spins of two Kerr BHs which are subjected to the common period modulation due to orbital motions of the Kerr BHs, we concluded the existence of the binary BH at SgrA* which are orbiting with the period of 2,200±50 s.

Following Kerr BH physics, the two intrinsic pulse periods of (173±1) and (148±1) sec detected from the BH Code resulted in BH masses of $(2.27\pm0.02)\times10^6$ $M_\odot$ for Gaa and $(1.94\pm0.01)\times10^6$ $M_\odot$ for Gab in the case of a maximal rotation parameter, assuming the direction of the orbiting plane to be parallel to the observation direction. From the BH Code, we can identify the orbiting velocities of the two BHs by measuring the relative levels of sidebands associated with each principal spin period spectra of Gaa and Gab; these are generated as manifestations of frequency modulations attributable to Doppler effects of the orbital motion; that is, Gaa and Gab have orbital velocities 18% and 21% of the speed of light, respectively. Furthermore, by assuming circular orbits for both Gaa and Gab, we can determine the orbit radii from Newtonian dynamics with information of orbiting period of 2,200± 50 sec, as 1.89×10^7 km and 2.21×10^7 km for Gaa and Gab, respectively. The obtained results for the SMBHB system are depicted in Figure 1.

Finally, by applying the simulation to produce BH Code for the resulted SMBHB system given in Figure 1, we have confirmed the coincidence of the FFT spectra (observed BH Code) with the simulated BH Code. The matching of FFT spectra between the simulation and observation results gives confirmation that the two kinds of pulses represent the two BHs Gaa and Gab forming the SMBHB system, where two spinning Kerr BHs radiate decameter radio waves whose time variations are synchronized with spins subjected to frequency modulations (from the Doppler effects produced by orbital motions). Regarding the assumption of the orbital plane direction when deducing the BH masses, we are required a slight correction for the observation angle of the orbital motions; this is described in Sec. 3.

2.2 Outline of EHT Visibility Data for Sgr A*

The EHT data to be compared with the DRWP-Model in the present work have been publicly released; they cover the EHT observations for April 6 and 7, 2017. The details of the EHT observation system and calibration for the observed data are described in the EHT reports [25–30] and references. Here, we present the outline necessary to compare the DRWP-Model, with reference to EHTC activities.

The first campaign of EHT observations for 1.3 mm-wavelength VLBI was carried out with eight observation antennae located at globally distributed six stations, as shown in Table 1 that is given by selecting information from the original table, shown in Table 2 [20].

At each station, observations were made at 227.1 and 229.1 GHz; these are referred to as "Low/Lo" and "High/Hi" respectively. The observed data (32 Gbits/sec) formed array data and were sent to a common location where the complex cross correlations were computed for the data from each corresponding pair observation station. Following computation of the correlation, the residual phase and band-pass errors were corrected via two independent data processing pipelines EHT-HOPS and rPICARD (called HOPS and CASA, respectively) for labelling and analysis.

The released data consisted of two days' observations for 24 pair baselines, with eight datasets for each baseline pair. For the sake of maintaining the observation conditions, the station in Pico Velta, Spain operated only on April 7 (Day 97). In the following work, we refer to the EHT-Data as, for example, "96 Hi CASA SM-SP" or "SM-SP 96 Hi CASA," which refers to the data observed on April 6, 2017 at 229.1 GHz, with a baseline between the sub-millimeter array at Hawaii and the South Pole Telescope, and a correlation computed using the CASA (rPICARD) pipeline.

Table 1: From EHT Station Information [20]

Facility	Abbreviation	Location	Latitude	Longitude	Elevation (m)
ALMA	AA	Chile	$-23°01'45''.1$	$-67°45'17''.1$	5074.1
APEX	AP	Chile	$-23°00'20''.8$	$-67°45'32''.9$	5104.5
JCMT	JC	Hawaii USA	$+19°49'22''.2$	$-155°28'37''.3$	4120.1
LMT	LM	Mexico	$+18°59'08''.8$	$-97°18'53''.2$	4593.3
PV 30m	PV	Spain	$+37°03'58''.1$	$-3°23'33''.4$	2919.5
SMA	SM	Hawaii USA	$+19°49'27''.2$	$-155°28'39''.1$	4115.1
SMT	AZ	Arizona USA	$+32°42'05''.8$	$-109°53'28''.5$	3158.7
SPT	SP	Antarctica	$-89°59'22''.9$	$-45°15'00''.3$	2816.5

3 Construction of DRWP-Model to Fit VLBI Visibilities of EHT
3.1 Basic Concept for Construction of Visibility Model for VLBI Observations

The visibility V_{mn} determined for coherent observation signals of the electric field between VLBI stations m and n is expressed by

$$V_{mn} = \int_{SgrA} E_m(\hat{k})E_n(\hat{k}) \exp\{-i[\boldsymbol{k} \cdot (\boldsymbol{r_m} - \boldsymbol{r_n})] + \theta_{mn}\} d\boldsymbol{k}, \qquad (1)$$

where $E_m(\hat{k})$ and $E_n(\hat{k})$ are the electric field intensities arriving from sources in the direction given by the unit vector $\hat{k}$ of the wave number vector $\boldsymbol{k}$, and $\boldsymbol{r_m}$ and $\boldsymbol{r_n}$ are vectors expressing the locations of the VLBI observatories m and n, respectively. In eq,(1), θmn is the residual phase difference of the observation signals after calibration of the instrumental phase difference; these primarily arise through environmental factors (e.g., weather condition s affecting the propagation of the millimeter waves). The wave number vector $\boldsymbol{k}$ is given for wavelength λ of the observed radio waves as $\boldsymbol{k}=(2\pi\lambda)\hat{k}$, and $d\boldsymbol{k}$ is an infinites-

imal coverage of the source directions centered around the direction given by $\hat{k}$. Our searches for the VSCAT (Variation with Short Characteristic Time) emissions at Sgr A* are performed upon these visibilities for the baseline pair m and n. In the VLBI data from the EHT, the visibilities are expressed by taking the correlation around Sgr A* in the direction RA: 17 h 45 m 40 s and at Dec: −29° 00′ 20″. We define the direction of Sgr A* with the highest possible accuracy for VLBI as $\boldsymbol{k}_{Sg}$; thus, eq. (1) can be rewritten as

$$V_{mn} = \int_{SgrA} E_m(\hat{k})E_n(\hat{k}) \exp\{-i[\Delta\boldsymbol{k} \cdot (\boldsymbol{r_m} - \boldsymbol{r_n})] + \theta_{mn}\} d\boldsymbol{k}, \qquad (2)$$

where $\Delta\boldsymbol{k}=\boldsymbol{k}-\boldsymbol{k}_{Sg}$. Furthermore, the EHT Data are expressed by averaging over every 10 second interval; thus,

$$\overline{V_{mn}}(t_\eta) = \frac{1}{10} \int_{t_\eta}^{t_\eta+10} \int_{SgrA} E_m(\hat{k})E_n(\hat{k}) \exp\{-i[\Delta\boldsymbol{k} \cdot (\boldsymbol{r_m} - \boldsymbol{r_n})] + \theta_{mn}\} d\boldsymbol{k}\, dt, \qquad (3)$$

where $\overline{V_{mn}}(t_\eta)$ is the discrete visibility at time t_η averaged every ten seconds. From the mathematical expression given by eq. (3), we can deduce the physically observable quantity as

$$[\overline{V_{mn}}(t_\eta)]_r = \sum_j W_{mnj} \cos[\Delta\boldsymbol{k_j} \cdot (\boldsymbol{r_m} - \boldsymbol{r_n}) + \theta_{mn}], \qquad (4)$$

where $[\overline{V_{mn}}(t_\eta)]_r$ is the real component of the complex visibility $\overline{V_{mn}}(t_\eta)$; j is the number of the selected source region. In the EHT-Data, the visibility data are unified to one (i.e., j = EHT). To construct the DRWP-Model, we set W_{mnOrb} as the amplitude of the visibility and set Δk_{Orb} to give a phase of j = Orb in eq. (4), to express the rotation of the orbiting SMBHB.

3.2 Amplitude Function W_{mnOrb}
The amplitude function W_{mnOrb} was constructed in [17] and confirmed as suitable for investigating the fitting with the 1.3 mm VLBI observation data observed in 2009 for Sgr A*, as provided by Fish et al. [5]. In that work, the coincidence was studied with respect to the sampled clear visibilities without phase terms, using the DRWP-Model (which consists of only the amplitude function); the approach of neglecting the phase variation of visibility was permittable because the visibility data were not continuous, as in the case of the EHT observations. However, we can apply the same amplitude function in the present case for comparing with EHT-Data. Because details are described in a previous paper [17], we here only summarize the amplitude function for the DRWR-Model.

3.2.1 Eclipse effects due to the orbital motion of the SMBHB
In the present study, we are at the standing point that the origin of the VSCAT in the VLBI-Data is primarily related to the motion of the SMBHB, except for the time of flare [1–4]; in the case of a gradual variation in background conditions [5–7], the model remains applicable. One significant effects of generating VSCAT emissions is the eclipse effects which can be predicted

morphologically from the orbiting conditions of the SMBHB. That is, the direction of the orbital plane indicate angle almost parallel to
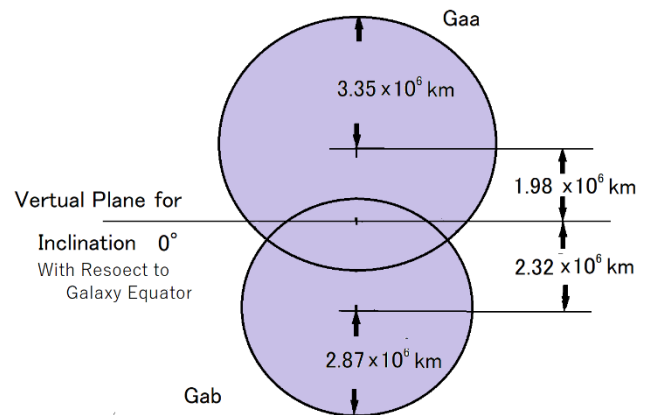
Figure 2: Geometrical configuration of the view from the observation points at maximal eclipse phase for the two SMBHs, Gaa and Gab. The orbital plane surface of the SMBHB is tilted by 6° from the direction parallel to the line of sight from the observation point. (After Oya [17])

the direction of the vector towards observation points, with a slight tilt of 6°[17]. This tilt is concluded by tracing the processes of obtaining the masses of the SMBHBs from the result of the DRWP observations. That is, the DRWP study concluded the total mass of the SMBHB as $M_D= (4.21\pm0.03)\times10^6$ M$_\odot$, by

assuming the direction of the orbital plane surface to be parallel to the observation direction (i.e., the inclination angle θ_I of the orbital plane with respect to Galactic equatorial plane is 0°). From long term observations of the stars around Sgr A*, the total mass is inferred as $M_{CD} = (4.28\pm0.31)\times10^6$ M$_\odot$ by Gillessen et al. [18]. When we attribute the difference between M_D and M_{CD} to inclination of the orbital plane in the mass reduction processes, we can deduce the correction angle $\Delta\theta$ with respect to θ_I (= 0°) as $\Delta\theta = 0.105$ radians (6.0 °).

As shown in Figure 2, the orbiting radii of Gaa and Gab are 1.89×10^7 km and 2.21×10^7 km, respectively. As effects of the deduced shift of inclination of (6.0°) an upward shift of 1.98×10^6 km is verified ,for the center of Gaa whose radius of the event horizon is 3.35×10^6 km from the virtual orbital plane assumed as a purely parallel to the line of sight. A downward shift of 2.32×10^6 km, also arising from the virtual plane, is deduced for the center of Gab whose event horizon radius is 2.87×10^6 km (see Figure 2). The upper and lower positions of both partner BHs in the SMBHB system, with respect to the virtual plane, are alternatively switched at each approaching maximal phase of the eclipse. Then, we observe twice the decrease of emission power for every orbiting period of 2200±50 sec. Based on the 6.0° tilt of the SMBHB orbit plane surface from the pure parallel direction with respect to the line of sight, we construct $E_c(t)$ as a function of the DRWP-Model, to facilitate comparison with the EHT-Data. That is,

$$E_c(t) = 1 - k_e \left[\frac{1 - cos2\Omega(t - t_0)}{2} \right]^{n_e}, \qquad (5)$$

where n_e is an index used to control the effective interval of the eclipse, and k_e is the rate of emission shaded by the partner SMBH at the eclipse's maximal phase. In principle, the n_e value is varied to identify the optimal fitting case in the processes, to identify the correlation between the EHT-Data and DRWP-Model; however, we fixed n_e as 4, following previous work [17].

3.2.2 Intensity variation due to spectral shift caused by Doppler effects
Though the effects of time variations in the observed EHT-Data are weak compared with the eclipse effect of the SMBHB, the possibility of time variation in the EHT-Data can be considered as spectra variations arising through orbital motions. With the exception of flares, the power law spectra of the radio emissions from Sgr A* are known to have an index of 0.3 [36]. In the regular state of the average condition of the accretion of the plasma, we assume that the radio wave emission spectra $P_j(\omega)$ for SMBH- j (j = Gaa or Gab) is

$$P_j(\omega) = K_j f^{0.3}, \qquad (6)$$

where f is the emission frequency at the source, and K_j is a constant coefficient that reflects all electromagnetic environments related to the radio wave emissions from each member j of the SMBHB. The observed frequency f_{ob} is related to the source frequency f, which is subjected to the Doppler effects of orbiting SMBH-j, as

$$f_{ob} = f \cdot \left[1 - \frac{v_j}{c} sin\theta_I cos\Omega(t - t_0) \right], \qquad (7)$$

where v_j and t_0 are the orbiting velocity and an arbitrary time, respectively, when SMBH Gaa is at the zero Doppler effect position for SMBH-j. The angle θ_I is defined between the line of sight and the normal direction of the orbital plane (determined to be 84.0°; see Sec. 3.2.1). Details are presented in the "interpretation" paper [17] of Fish et al.'s results [5]; the emission power $P_{dj}(f_{ob})$ detected at observation frequency f_{ob} for each SMBH-j is expressed as

$$P_{dj}(f_{ob}) = K_j f_{ob}^{0.3} \left[1 + \frac{0.3v_j}{c} sin\theta_I cos\Omega(t - t_0) \right]. \qquad (8)$$

3.2.3 Total model function W_{mnOrb} to express effects of SMBHB orbital motion
The emissions from partner SMBH-j that are shaded by the eclipse are switched alternatively between Gaa and Gab. In the equation, to express the time-varying power, we define a switching function ; thus, the model of the time dependent emission power $W_T(t)$ from the SMBHB at Sgr A* is given by

$$W_T(t) = \left\{ K_{Gaa} f_{ob}^{0.3} \left[1 + \frac{0.3v_{Gaa}}{c} sin\theta_I cos\Omega(t - t_0) \right] S_{Gaa}(t) \right.$$

$$\left. + K_{Gab} f_{ob}^{0.3} \left[1 - \frac{0.3v_{Gab}}{c} sin\theta_I cos\Omega(t - t_0) \right] S_{Gab}(t) \right\} E_c(t), \qquad (9)$$

where $S_{Gaa}(t)$ and $S_{Gab}(t)$ are defined as

$$S_{Gaa}(t) = \begin{cases} 1 & for \ 2m\pi \leq \Omega(t - t_0) < (2m + 1)\pi \\ 1/E_c(t) & for \ 2(m + 1)\pi \leq \Omega(t - t_0) < (2m + 2)\pi, \end{cases}$$

and

$$S_{Gab}(t) = \begin{cases} 1/E_c(t) & for \ 2m\pi \leq \Omega(t - t_0) < (2m + 1)\pi \\ 1 & for \ 2(m + 1)\pi \leq \Omega(t - t_0) < (2m + 2)\pi \end{cases}, \quad (10)$$

respectively, with m as an arbitrary integer.

The ratios between the radio wave emission powers of Gaa and Gab at the 1.3-mm wavelength is strictly related to the environment, where the source energy is provided by accreting plasma from the outside; the ratio is related to the efficiency with which the energy of accreting plasma is converted into radio-wave emissions. In this context, we can conclude that no apparent difference arises in the accreting plasma conditions between the two SMBHs, owing to their similarity of orbits in the SMBHB. Regarding the conversion efficiency, the slight differences in the masses and sizes of the two SMBHs may affect the processes by which the radio waves are generated. However, we assume no significant difference from a macroscopic estimation perspective. Based on this assumption and, the already presented v_{Gaa}/c and v_{Gab}/c values, together with $\theta_I = 90° - 6.0°$, we can express eq. (9) in a simplified form, as

$$\overline{W_T(t)} = \{[1 + 0.0537 cos\Omega(t - t_0)]S_{Gaa}(t)$$
$$+ [1 - 0.0626 cos\Omega(t - t_0)]S_{Gab}(t)\}E_c(t), \quad (11)$$

where $\overline{W_T(t)} \equiv W_T(t)/(K_{Gaa}f_{ob}^{0.3})$.

At this point, we recognize that the effects of time variation when observing emission spectra are minor, with a rate of ~20% compared with the effects of the eclipse upon the time variation, which indicates a rate of k_e (= 0.3) for shading the observing emissions from one of the SMBHs.
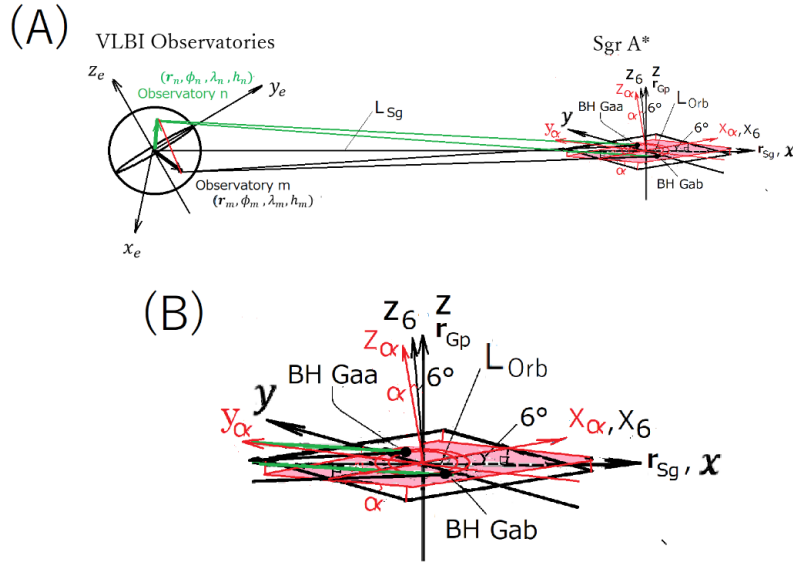
Figure 3: Geometrical relations between the rotating SMBHB at SgrA* and EHT VLBI observatories at (m) and (n). (A) Over all description. The orbiting SMBH Gaa and Gab are described in the Cartesian coordinate with the origin at the center of SgrA* ; the direction of x axis coincides with the unit vector $\hat{k}_{Sg}$ that is defined to coincide with the direction to connect between the earth's center and the center of SgrA*.The y axis of the reference coordinate prepared to describe the SMBHB orbital plane is set to be vertical to x axis and also to the Galactic north pole direction to be in parallel with the Galactic plane. The location of the VLBI observatories of EHT are described in the regular astronomical coordinate of the equatorial spring equinox system whose z_e axis coincides with the axis of the earth rotation with parameters $r_m, \varphi_m, \lambda_m$ and h_m for observatory m, respectively for the distance between the earth center, longitude, latitude and the height from the sea surface. The distance from the earth center and the center of the SgrA* is given by L_{sg} meanwhile the distance between SMBH Gaa and Gab is expressed by L_{Orb}. (B) Fine description of SMBHB plane. With respect to the reference coordinate. The orbital plane of SMBHB is set with two inclination steps ; these are the 6 degree inclination of SMBHB orbital plane looking from the Earth and inclination which is described as tilt of the normal direction of the SMBHB orbital plane from the Galactic north pole direction by the angle α (see red vector) ; the new y direction in the inclined SMBHB plane is defined as y_α. The real case of inclined angle α is searched by finding maximum correlation between the EHT Data and DRWP Model.

3.3 Construction of the Phase Function $\Delta k_{Orb} \cdot (r_m - r_n)$
3.3.1 Decision of the orbital plane of SMBHB to construct Δk_{Orb}

Corresponding to the phase $\Delta k_j \cdot (r_m - r_n)$ in eq. (4) (j = Orb), we consider the phase function $\mathcal{F}$ defined by

$$\mathcal{F} = \cos[\Delta k_{Orb} \cdot (r_m - r_n)]. \qquad (12)$$

That is, the source covering the orbit range of the SMBHB is expressed by taking j to be "Orb." For description of Δk_{Orb}, we consider the geometrical relationship given in Figure 3, where we set relationships between the orbiting SMBHBs at Sgr A* and the VLBI observatories of EHT. The orbiting plane of SM-BHs Gaa and Gab are described setting the coordinate center at the Galaxy center Sgr A* with the reference vector whose direction coincide with the direction of SgrA* observed from the earth (see eq.(13)). To describe the geometry of the orbital plane of SMBHB, we have selected the Galactic equatorial plane as the reference to decide the normal direction of the orbital plane. Within the two dimensional freedom to decide the normal direction of the orbiting plane we are required a constraint that the orbital plane surface is inclined by 6 degree (INCL hereafter) from the direction of the SgrA*. There remains, however, one freedom to fix the orbital plane of SMBHB; that is, within the constrain of the direction towards SgrA* with inclination of 6 degree ,the possible orbital plane can be selected by rotating (ROTE hereafter) in the direction by taking the vector towards SgrA* as an axis. Then we describe the possible orbital plane by the two steps after setting the reference by using the Cartesian coordinate, x, y, z with unit vectors $\hat{x}, \hat{y}$ and $\hat{z}$, respectively ,which are given in the astronomical equatorial-spring equinox coordinate system , as,

$$\hat{x} = \cos\delta_{Sg}\cos\phi_{Sg}\hat{x}_e + \cos\delta_{Sg}\sin\phi_{Sg}\hat{y}_e + \sin\delta_{Sg}\hat{z}_e. \qquad (13)$$

$$\hat{y} = (\cos\delta_{Gp}\sin\delta_{Sg}\sin\phi_{Gp} - \cos\delta_{Sg}\sin\delta_{Gp}\sin\phi_{Sg})\hat{x}_e + (\cos\delta_{Sg}\sin\delta_{Gp}\cos\phi_{Sg} - \sin\delta_{Sg}\cos\delta_{Gp}\cos\phi_{Gp})\hat{y}_e + (\cos\delta_{Sg}\sin\phi_{Sg}\cos\delta_{Gp}\cos\phi_{Gp} - \cos\delta_{Sg}\cos\phi_{Sg}\cos\delta_{Gp}\sin\phi_{Gp})\hat{z}_e \qquad (14)$$

and

$$\hat{z} = \cos\delta_{Gp}\cos\phi_{GP}\hat{x}_e + \cos\delta_{GP}\sin\phi_{GP}\hat{y}_e + \sin\delta_{GP}\hat{z}_e. \qquad (15)$$

where ϕ_{Sg} and δ_{Sg} are the right ascension and declination of SgrA* respectively; and ϕ_{Gp} and δ_{Gp} are the right ascension and declination of North Galactic pole. The vectors $\hat{x}_e, \hat{z}_e$ and $\hat{y}_e$, in eqs.(13) to (15) are the unit vector directed toward the sun at spring equinox at 0h UT, the unit vector parallel to the earth rotation axis and the unit vector perpendicular to both $\hat{x}_e$ and $\hat{z}_e$, respectively.

The selection which process we take as the first step between the INCL and ROTE reveals different results in general: but as has been described in Appendix A , we are able to have approximately same results in the case of small angle deviation such as the case smaller than 10° for an example, both for INCL and ROTE. Then we take the ROTE process as the first step.

a) T he first step.
We define a new Cartesian coordinate ($x_\alpha, y_\alpha, z_\alpha$) for the ROTE of the orbital plane by rotating angle $\pm\alpha$ (takes + for the rotation towards +y direction) . The unit vectors for corresponding coordinate axis $\hat{x}_\alpha, \hat{y}_\alpha$, and $\hat{z}_\alpha$ are then expressed by

$$\hat{x}_\alpha = \hat{x}, \qquad (16)$$
$$\hat{y}_\alpha = \cos\alpha\hat{y} - \sin\alpha\hat{z}, \qquad (17)$$

$$\hat{z}_\alpha = \sin\alpha\hat{y} + \cos\alpha\hat{z}. \qquad (18)$$

It should be noted that this ROTE angle is unknown at the present stage. The decision of α is then made in the processes to find the best fit value between EHT-Data and DRWP-Model as will be described in Sec 5.

b) The second step
We define the Cartesian coordinate (x_p, y_p, z_p) with corresponding unit vector $\hat{x}_p, \hat{y}_p$, and $\hat{z}_p$ for the finally decided orbital plane by INCL angle β=6° . That is, unit vectors are

$$\hat{x}_p = \cos\beta \, \hat{x}_\alpha + \sin\beta\hat{z}_\alpha ,$$
$$\hat{y}_p = \hat{y}_\alpha$$
$$\hat{z}_p = -\sin\beta \, \hat{x}_\alpha + \cos\beta\hat{z}_\alpha . \qquad (19)$$

By inserting eqs(16),(17) and (18) into corresponding equations in eq.(19), we have the relations between ($\hat{x}, \hat{y}, \hat{z}$) and ($\hat{x}_p, \hat{y}_p, \hat{z}_p$), as

$$\hat{x}_p = \cos\beta\hat{x} + \sin\alpha \cdot \sin\beta \, \hat{y} + \cos\alpha \cdot \sin\beta\hat{z} . \qquad (20)$$
$$\hat{y}_p = \cos\alpha \, \hat{y} - \sin\alpha\hat{z} . \qquad (21)$$

and

$$\hat{z}_p = -\sin\beta\hat{x} + \sin\alpha \cdot \cos\beta \, \hat{y} + \cos\alpha \cdot \cos\beta\hat{z} . \qquad (22)$$

As given by eqs.(9) and (11), there are two causes to give variation of the brightness of the emitted millimeter radio waves; those are Doppler effects to vary the radiating spectra that vary with orbiting angular velocity Ω_{Orb} ,and the eclipse effects of two orbiting SMBHs which evolve with the twice of the orbiting angular velocity as $2\Omega_{Orb}$.

The DRWP-Model purposed to search for the identity with the EHT observation results, then, consists of two unit vectors corresponding to above described two effects; that is, we describe $\Delta\mathbf{k}_{Orb}$ as

$$\Delta\boldsymbol{k}_{Orb} = (2\pi/\lambda)\left(L_{Orb}\,./L_{Sg}\right) \cdot \left(\hat{k}_1 + \kappa_r\hat{k}_2\right). \qquad (23)$$

where $\hat{k}_1$ and $\hat{k}_2$ are unit vectors which rotate with orbiting angular velocity Ω_{Orb} and rotate with the angular velocity of $2\Omega_{Orb}$ forming a bar connecting geometry between SMBH Gaa and Gab that results ecliptic effects for observation points; κ_r is a rate

for giving the weight to eclipse effect compared with effects of spectra modulation due to the Doppler effects . Then two unit vectors are expressed by

$$\hat{k}_1 = cos(\Omega_{Orb}t + \varphi_{Orb})\hat{x}_p + sin(\Omega_{Orb}t + \varphi_{Orb})\hat{y}_p \,. \qquad (24)$$

and

$$\hat{k}_2 = cos(2\Omega_{Orb}t + \varphi_{Orb})\hat{x}_p + sin(2\Omega_{Orb}t + \varphi_{Orb})\hat{y}_p \,. \qquad (25)$$

Thus, $\hat{k}_1 + \kappa_r \hat{k}_2$ term that is essential to obtain $\Delta\boldsymbol{k}_{Orb}$ as given by eq.(23) is expressed (see Appendix A) by

$$
\begin{aligned}
\hat{k}_1 + \kappa_r\hat{k}_2 = &\{[cos(\Omega_{Orb}t + \varphi_{Orb}) + \kappa_r cos(2\Omega_{Orb}t + \varphi_{Orb})]A_x \\
&+ [sin(\Omega_{Orb}t + \varphi_{Orb}) + \kappa_r sin(2\Omega_{Orb}t + \varphi_{Orb})]B_x\}\hat{x}_e \\
&+ \{[cos(\Omega_{Orb}t + \varphi_{Orb}) + \kappa_r cos(2\Omega_{Orb}t + \varphi_{Orb})]A_y \\
&+ [sin(\Omega_{Orb}t + \varphi_{Orb}) + \kappa_r sin(2\Omega_{Orb}t + \varphi_{Orb})]B_y\}\hat{y}_e \\
&+ \{[cos(\Omega_{Orb}t + \varphi_{Orb}) + \kappa_r cos(2\Omega_{Orb}t + \varphi_{Orb})]A_z \\
&+ [sin(\Omega_{Orb}t + \varphi_{Orb}) + \kappa_r sin(2\Omega_{Orb}t + \varphi_{Orb})]B_z\}\hat{z}_e
\end{aligned}
$$
$$(26)$$

where A_i (i=x,y,z) and B_j (j=x,y ,z) are given as follows (see Appendix A for details):

$$. A_x = cos\beta\,cos\delta_{Sg}cos\phi_{Sg} + sin\alpha \cdot sin\beta\left(cos\delta_{Gp}sin\delta_{Sg}sin\phi_{Gp} - cos\delta_{Sg}sin\delta_{Gp}sin\phi_{Sg}\right)$$
$$+cos\alpha \cdot sin\beta cos\delta_{Gp}cos\alpha_{GP}, \qquad (26-1)$$

$$A_y = cos\beta cos\delta_{Sg}sin\phi_{Sg} + sin\alpha sin\beta\left(cos\delta_{Sg}sin\delta_{Gp}cos\phi_{Sg} - sin\delta_{Sg}cos\delta_{Gp}cos\phi_{Gp}\right)$$
$$+cos\alpha \cdot sin\beta cos\delta_{GP}sin\alpha_{GP} \quad , \qquad (26-2)$$

$$A_Z = cos\beta sin\delta_{Sg} + \; sin\alpha\,sin\beta\left(cos\delta_{Sg}sin\phi_{Sg}cos\delta_{Gp}cos\phi_{Gp} \; - cos\delta_{Sg}cos\phi_{Sg}cos\delta_{Gp}sin\phi_{Gp}\right)$$
$$+cos\alpha \cdot sin\beta sin\delta_{GP}, \qquad (26-3)$$

$$B_x = cos\alpha \cdot \left(cos\delta_{Gp}sin\delta_{Sg}sin\phi_{Gp} - cos\delta_{Sg}sin\delta_{Gp}sin\phi_{Sg}\right) - sin\alpha cos\delta_{Gp}cos\alpha_{GP},$$
$$(26-4)$$

$$B_y = cos\alpha \cdot \left(cos\delta_{Sg}sin\delta_{Gp}cos\phi_{Sg} - sin\delta_{Sg}cos\delta_{Gp}cos\phi_{Gp}\right) - sin\alpha \cdot cos\delta_{GP}sin\alpha_{GP} \,,$$
$$(26-5)$$

and

$$B_z = cos\alpha \cdot \left(cos\delta_{Sg}sin\phi_{Sg}cos\delta_{Gp}cos\phi_{Gp} \; - cos\delta_{Sg}cos\phi_{Sg}cos\delta_{Gp}sin\phi_{Gp}\right) - sin\alpha sin\delta_{GP}.$$
$$(26 \text{-} \; 6)$$

The distance L_{sg} from the earth center and the center of the SgrA* given in eq.(23), is estimated to be 2.57×10^{22} cm corresponding 8.3 kpc, while the distance of the orbiting SMBH Gaa and Gab (see Figure 1) expressed by L_{Orb} (also given in eq.(18)

is given by 4.10×10^{12} cm. The spreading of the wave number vector $\Delta\mathbf{k}_{Orb}$ with respect to direction of the unit vector $\hat{x}\equiv\hat{k}_{sg}$ provides order of magnitude as

$$|\Delta \boldsymbol{k}_{Orb}| = (2\pi/\lambda)\left(L_{Orb}/L_{sg}\right) = 1.6 \times (2\pi/\lambda) \times 10^{-10}. \qquad (27)$$

. Then using this expression we have phase function $\mathcal{F}$ corresponding to eq.(12) as

$$\mathcal{F} = cos\Theta \ . \qquad (28)$$

where Θ is given by

$$\Theta = 2\pi \frac{L_{Orb}}{L_{Sg}}\left(\hat{k}_1 + \kappa_r \hat{k}_2\right) \cdot \frac{(\boldsymbol{r}_m - \boldsymbol{r}_n)}{\lambda} \ . \qquad (29)$$

3.3.2 Time dependent characteristics of phase function $\mathcal{F}$

The locations of the VLBI observatories of EHT are described in the regular astronomical coordinates of the equatorial–spring equinox system whose z_e axis coincides with the axis of the Earth's rotation; that is, locations of observatories are given by parameters $r_m, \varphi_m, \lambda_m$, and h_m for observatory m; these denote the distance from the Earth's center, longitude, latitude, and height above sea level, respectively. Then, $\boldsymbol{r}_m$ - $\boldsymbol{r}_n$ vector is expressed in the equator–spring equinox coordinate system as

$$\begin{aligned}\boldsymbol{r}_m - \boldsymbol{r}_n = &\{(r_e + h_m)cos\delta_m cos[\Omega_e(t - t_0) + \phi_m] - (r_e + h_n)cos\delta_n cos[\Omega_e(t - t_0) + \phi_n]\}\hat{x}_e \\ &+\{(r_e + h_m)cos\delta_m sin[\Omega_e(t - t_0) + \phi_m] - (r_e + h_n)cos\delta_n sin[\Omega_e(t - t_0) + \phi_n]\}\hat{y}_e \\ &+[(r_e + h_m)sin\delta_m - (r_e + h_n)sin\delta_n]\hat{z}_e, \qquad (30)\end{aligned}$$

where r_e, and Ω_e are Earth's radius and angular velocity of the Earth, respectively; t and 0 are the time passage and the initial time respectively. Using eq. (30), therefore , we can calculate the phase Θ of the phase function [eq. (12)] (12) as detail is explained in Appendix B where expressions are made by approximating the level of the observatory as $r_e \gg h_m$ to make the mathematical manipulation tractable from the perspective of investigating the time dependent characteristics of VLBI visibilities. By defining C_{mn} and D_{mn} as

$$C_{mn} = cos\delta_m cos\phi_m - cos\delta_n cos\phi_n \ , \qquad (31)$$

and

$$D_{mn} = cos\delta_m sin\phi_m - cos\delta_n sin\phi_n \ , \qquad (32)$$

then

Θ is expressed by

$$\begin{aligned}\Theta = \pi \frac{L_{Orb}}{L_{Sg}} \cdot \frac{r_e}{\lambda} [\![K_c\{cos[(\Omega_{Orb} + \Omega_e)\tau + \xi_{Orb}] + \kappa_r cos[(2\Omega_{Orb} + \Omega_e)\tau + \eta_{Orb}]\} \\ + K_s\{sin[(\Omega_{Orb} + \Omega_e)\tau + \xi_{Orb}] + \kappa_r sin[(2\Omega_{Orb} + \Omega_e)\tau + \eta_{Orb}]\} \\ + L_c\{cos[(\Omega_{Orb} - \Omega_e)\tau + \xi_{Orb}] + \kappa_r cos[(2\Omega_{Orb} - \Omega_e)\tau + \eta_{Orb}]\} \\ + L_s\{sin[(\Omega_{Orb} - \Omega_e)\tau + \xi_{Orb}] + \kappa_r sin[(2\Omega_{Orb} - \Omega_e)\tau + \eta_{Orb}]\} \\ + M_c[cos(\Omega_{Orb}\tau + \xi_{Orb}) + \kappa_r cos(2\Omega_{Orb}\tau + \eta_{Orb})] \\ + M_s[sin(\Omega_{Orb}\tau + \xi_{Orb}) + \kappa_r sin(2\Omega_{Orb}\tau + \eta_{Orb})]]\!] \qquad (33)\end{aligned}$$

where coefficients K_c, K_s, L_c, L_s, M_c and M_s are given as follows:

$$\begin{aligned}K_c &= \left[(A_x - B_y)C_{mn} + (A_y + B_x)D_{mn}\right] & (33-1) \\ K_s &= \left[(A_y + B_x)C_{mn} - (A_x - B_y)D_{mn}\right], & (33-2) \\ L_c &= \left[(A_x + B_y)C_{mn} + (A_y - B_x)D_{mn}\right] & (33-3) \\ L_s &= \left[(-A_y + B_x)C_{mn} + (A_x + B_y)D_{mn}\right] & (33-4) \\ M_c &= (sin\delta_m - sin\delta_n)A_z & (33-5) \\ M_s &= (sin\delta_m - sin\delta_n)B_z & (33-6)\end{aligned}$$

In eq. (33), we see six pairs of cosine and sine functions, with angular frequencies $\Omega_{Orb}-\Omega_e, \Omega_{Orb}, \Omega_{Orb}+\Omega_e, 2\Omega_{Orb}-\Omega_e, 2\Omega_{Orb}$, and $2\Omega_{Orb}+\Omega_e$. For these pairs of cosine and sine functions, we have a sinusoidal function, for each, expressed as

$$K_c cos[(\Omega_{Orb} + \Omega_e)\tau + \xi_{Orb}] + K_s sin[(\Omega_{Orb} + \Omega_e)\tau + \xi_{Orb}]$$

$$= \sqrt{K_c^2 + K_s^2} cos\left[(\Omega_{Orb} + \Omega_e)\tau + \Phi_{K\xi}\right]. \qquad (34)$$

where $\Phi_{K\xi}$ is given by

$$\Phi_{K\xi} = \xi_{Orb} - tan^{-1}\left(\frac{K_s}{K_C}\right).$$

Then by rewriting eq.(33) with newly defined six coefficients we have the results of Θ as

$$\Theta = \sum_{i=1}^{6} \Theta_i . \qquad (35)$$

where Θ_i (i = 1 to 6) are given by

$$\Theta_1 = \pi \frac{L_{Orb}}{L_{Sg}} \cdot \frac{r_e}{\lambda} \sqrt{K_c^2 + K_s^2} cos\left[(\Omega_{Orb} + \Omega_e)\tau + \Phi_{K\xi}\right] \qquad (35-1)$$

$$\Theta_2 = 2\pi \frac{L_{Orb}}{L_{Sg}} \cdot \frac{r_e}{\lambda} \sqrt{M_c^2 + M_s^2} cos\left[\Omega_{Orb}\tau + \Phi_{M\xi}\right] \qquad (35-2)$$

$$\Theta_3 = \pi \frac{L_{Orb}}{L_{Sg}} \cdot \frac{r_e}{\lambda} \sqrt{L_c^2 + L_s^2} cos\left[(\Omega_{Orb} - \Omega_e)\tau + \Phi_{L\xi}\right] \qquad (35-3)$$

$$\Theta_4 = \pi \frac{L_{Orb}}{L_{Sg}} \cdot \frac{r_e}{\lambda} \kappa_r \sqrt{K_c^2 + K_s^2} cos\left[(2\Omega_{Orb} - \Omega_e)\tau + \Phi_{K\eta}\right] \qquad (35-4)$$

$$\Theta_5 = 2\pi \frac{L_{Orb}}{L_{Sg}} \cdot \frac{r_e}{\lambda} \kappa_r \sqrt{M_c^2 + M_s^2} cos\left[2\Omega_{Orb}\tau + \Phi_{M\eta}\right] \qquad (35-5)$$

$$\Theta_6 = \pi \frac{L_{Orb}}{L_{Sg}} \cdot \frac{r_e}{\lambda} \kappa_r \sqrt{L_c^2 + L_s^2} cos\left[(2\Omega_{Orb} + \Omega_e)\tau + \Phi_{L\eta}\right] \qquad (35-6)$$

with $\Phi_{K\xi}, \Phi_{M\xi}, \Phi_{L\xi}, \Phi_{K\eta}, \Phi_{M\eta}$, and $\Phi_{L\eta}$ which are given below:

$$\Phi_{K\xi} = \xi_{Orb} - tan^{-1}\left(\frac{K_s}{K_C}\right). \qquad (35-7)$$

$$\Phi_{M\xi} = \xi_{Orb} - tan^{-1}\left(\frac{M_s}{M_C}\right). \qquad (35-8)$$

$$\Phi_{L\xi} = \xi_{Orb} - tan^{-1}\left(\frac{L_s}{L_C}\right). \qquad (35-9)$$

$$\Phi_{K\eta} = \eta_{Orb} - tan^{-1}\left(\frac{K_s}{K_C}\right). \qquad (35-10)$$

$$\Phi_{M\eta} = \eta_{Orb} - tan^{-1}\left(\frac{M_s}{M_C}\right). \qquad (35-11)$$

and

$$\Phi_{L\eta} = \eta_{Orb} - tan^{-1}\left(\frac{L_s}{L_C}\right). \qquad (35-12)$$

With these arguments defined from eq.(35-1) to eq.(35-6) then we can find time dependence of the phase part of the visibility from eq.(35), as

$cos\Theta=cos(\Theta_1+\Theta_2+\Theta_3+\Theta_4+\Theta_5+\Theta_6)$

$$
\begin{aligned}
&=cos\Theta_1\,cos\Theta_2\,cos\Theta_3\,cos\Theta_4\,cos\Theta_5\,cos\Theta_6 - sin\Theta_1\,sin\Theta_2\,cos\Theta_3\,cos\Theta_4\,cos\Theta_5\,cos\Theta_6 \\
&\quad - sin\Theta_1\,cos\Theta_2\,sin\Theta_3\,cos\Theta_4\,cos\Theta_5\,cos\Theta_6 - cos\Theta_1\,sin\Theta_2\,sin\Theta_3\,cos\Theta_4\,cos\Theta_5\,cos\Theta_6 \\
&\quad - sin\Theta_1\,cos\Theta_2\,cos\Theta_3\,sin\Theta_4\,cos\Theta_5\,cos\Theta_6 - cos\Theta_1\,sin\Theta_2\,cos\Theta_3\,sin\Theta_4\,cos\Theta_5\,cos\Theta_6 \\
&\quad - cos\Theta_1\,cos\Theta_2\,sin\Theta_3\,sin\Theta_4\,cos\Theta_5\,cos\Theta_6 + sin\Theta_1\,sin\Theta_2\,sin\Theta_3\,sin\Theta_4\,cos\Theta_5\,cos\Theta_6
\end{aligned}
$$

$$-sin\Theta_1 cos\Theta_2 cos\Theta_3 cos\Theta_4 sin\Theta_5 cos\Theta_6 - cos\Theta_1 sin\Theta_2 cos\Theta_3 cos\Theta_4 sin\Theta_5 cos\Theta_6$$

$$- cos\Theta_1 cos\Theta_2 sin\Theta_3 cos\Theta_4 sin\Theta_5 cos\Theta_6 + sin\Theta_1 sin\Theta_2 sin\Theta_3 cos\Theta_4 sin\Theta_5 cos\Theta_6$$

$$- cos\Theta_1 cos\Theta_2 cos\Theta_3 sin\Theta_4 sin\Theta_5 cos\Theta_6 + sin\Theta_1 sin\Theta_2 cos\Theta_3 sin\Theta_4 sin\Theta_5 cos\Theta_6$$

$$+ sin\Theta_1 cos\Theta_2 sin\Theta_3 sin\Theta_4 sin\Theta_5 cos\Theta_6 + cos\Theta_1 sin\Theta_2\,sin\Theta_3 sin\Theta_4 sin\Theta_5 cos\Theta_6$$

$$-sin\Theta_1 cos\Theta_2 cos\Theta_3 cos\Theta_4 cos\Theta_5 sin\Theta_6 - cos\Theta_1 sin\Theta_2 cos\Theta_3 cos\Theta_4 cos\Theta_5 sin\Theta_6$$

$$- cos\Theta_1 cos\Theta_2 sin\Theta_3 cos\Theta_4 cos\Theta_5 sin\Theta_6 + sin\Theta_1 sin\Theta_2 sin\Theta_3 cos\Theta_4 cos\Theta_5 sin\Theta_6$$

$$- cos\Theta_1 cos\Theta_2 cos\Theta_3 sin\Theta_4 cos\Theta_5 sin\Theta_6 + sin\Theta_1 sin\Theta_2 cos\Theta_3 sin\Theta_4 cos\Theta_5 sin\Theta_6$$

$$- sin\Theta_1 cos\Theta_2 sin\Theta_3 sin\Theta_4 cos\Theta_5 sin\Theta_6 + cos\Theta_1 sin\Theta_2\,sin\Theta_3 sin\Theta_4 cos\Theta_5 sin\Theta_6$$

$$- cos\Theta_1 cos\Theta_2 cos\Theta_3 cos\Theta_4 sin\Theta_5 sin\Theta_6 + sin\Theta_1 sin\Theta_2 cos\Theta_3 cos\Theta_4 sin\Theta_5 sin\Theta_6$$

$$+ sin\Theta_1 cos\Theta_2 sin\Theta_3 cos\Theta_4 sin\Theta_5 sin\Theta_6 + cos\Theta_1 sin\Theta_2\,sin\Theta_3 cos\Theta_4 sin\Theta_5 sin\Theta_6$$

$$+ sin\Theta_1 cos\Theta_2 cos\Theta_3 sin\Theta_4 sin\Theta_5 sin\Theta_6 + cos\Theta_1 sin\Theta_2 cos\Theta_3 sin\Theta_4 sin\Theta_5 sin\Theta_6$$

$$+ cos\Theta_1 cos\Theta_2 sin\Theta_3 sin\Theta_4 sin\Theta_5 sin\Theta_6 - sin\Theta_1 sin\Theta_2 sin\Theta_3 sin\Theta_4 sin\Theta_5 sin\Theta_6 \tag{36}$$

Using eq. (36), (see Appendix B for details) we can investigate the time dependence of the phase component of visibility by calculating $cos\Theta_i$ and $sin\Theta_i$ (i=1 6). When we attempt to rewrite $cos\Theta_1$ (selecting i = 1 as an example), it follows from eq. (35-1) that

$$cos\Theta_1 = cos\left\{\pi\frac{L_{Orb}}{L_{Sg}}\cdot\frac{r_e}{\lambda}\sqrt{K_c^2 + K_s^2}\,cos\left[(\Omega_{Orb} + \Omega_e)\tau + \Phi_{K\xi}\right]\right\}. \tag{37}$$

By setting

$$\zeta_1 = \pi\frac{L_{Orb}}{L_{Sg}}\cdot\frac{r_e}{\lambda}\sqrt{K_c^2 + K_s^2}\,, \tag{37-1}$$

and

$$\mu_1 = (\Omega_{Orb} + \Omega_e)\tau + \Phi_{K\xi}\,, \tag{37-2}$$

, then $cos\Theta_1$ given by eq.(37) is expanded using the Bessel functions as

$$cos\Theta_1 = cos(\zeta_1 cos\mu_1) = J_0(\zeta_1) - 2J_2(\zeta_1)cos2\mu_1 + 2J_4(\zeta_1)cos4\mu_1 - \cdots\cdots \tag{38}$$

When we apply the procedure to have eq.(38) starting from eq.eq.(37) for Θ_1 to the general expression of Θ_i considering the similarity of eqs. (35-1) to (36-6) it follows that

$$\Theta_i = \zeta_i cos\mu_i\,. \tag{39}$$

Then, all member terms in eq.(36) that consist of six components as combination of $cos\theta_i$ and $sin\theta_i$ are expressed as sequence of $cos(m\mu_i)$ (m=0 ,1,2,3 $\cdots\cdots$) formed by relations,

$$cos\Theta_i = \cos(\zeta_i cos\mu_i) = J_0(\zeta_i) - 2J_2(\zeta_i)cos2\mu_i + 2J_4(\zeta_i)cos4\mu_i - \cdots\cdots, (40-1)$$

and

$$sin\Theta_i = \sin(\zeta_i cos\mu_i) = 2J_1(\zeta_i)cos\mu_i - 2J_3(\zeta_i)cos3\mu_i + \cdots\cdots . \qquad (40-2)$$

Taking eq. (36) and inserting eqs. (40-1–40-2) together with eq. (39), we find that the time variation of the phase component for the visibilities of the DRWP-Model for the comparison with EHT Data is extremely complicated, where the six basic time varying components (with angular frequencies of $\Omega_{Orb} - \Omega_e$, Ω_{Orb}, $\Omega_{Orb} + \Omega_e$, $2\Omega_{Orb} - \Omega_e$, $2\Omega_{Orb}$, and $2\Omega_{Orb} + \Omega_e$) together with the generated higher harmonics (shorter-period phenomena) and mutually coupled frequencies form a sophisticated ensemble.

3.4 Constructed DRWP-Model to Identify Correspondence with VLBI Visibilities from EHT

Based on a detailed investigation of the relationship how the orbital motions of SMBHB concluded from the DRWP observations reflect to the observation of visibilities by EHT VLBI system is described in this sub-section; and we obtain the form of the DRWP-Model as follows.

3.4.1 Amplitude and Bias
Using this model function as the DRWP-Model based on data from the DRWP observations, we conduct a comparison with the EHT-Data. For this purpose, we are required an additional adjustment by introducing an amplitude A(mn) to match the observation level given by the EHT-Data, because the function of the DRWP-Model, given by eq. (11), is expressed only as relative quantity normalized by the 1.3 mm-wavelength emission power of the SMBH Gaa. The amplitude A(mn) is given according to the observation day for each baseline pair of observatories m and n. Sometimes it is necessary to shift the data (adding or subtracting) using a bias function Bias (mn).

In this way, we prepared the final form of the model function Mod(t,m) as the amplitude of the DRWP-Model visibility, starting from eq. (11); thus, we have

$$Mod(t,mn) = A(mn)\{[1 + 0.0537 \cdot cos\Omega(t - t_0)]S_{Gaa}(t) +$$
$$[1 - 0.0626 \cdot cos\Omega(t - t_0)]S_{Gab}(t)\}E_c(t) + Bias(mn) \qquad (41)$$

To determine the parameters A(mn) and Bias(mn), we sought the best-fitting values by sweeping the possible ranges for each parameter.

3.4.2 Period and initial phase angle of SMBHs along the orbit
The most important parameter for "finding coincidence between the EHT-Data and DRWP-Model" (FCED here after) is the search period of the VSCAT in the EHT-Data. Because of the principal philosophy of the present study, we set the period range according to the results of the DRWP observations, which indicated the period of T=2200±50 s. Considering the study result that compared with previous VLBI data that indicated around 2150 sec[17], however, we set the center period at 2175 sec (as the middle value between 2150 and 2200 sec) with deviation range around ±75 sec. Then, we selected a searching range for T for the FCED from 2100 to 2250 sec (most of the cases, 2245sec).

The second significant parameter for FCED is the initial phase of the SMBHB's orbital motions, which are controlled by the time t_0 in eq. (11). In the direct comparison for FCDE, we have swept the whole range (0–2π rad) as the initial phase angle, Ωt_0 with a step of (π/9) rad. In the case of the Fourier-transformed space comparison for FCED, we can avoid the initial phase parameter by sacrificing the phase information of the Fourier transformation, though we are required additional approximation (as given in Sub. Sec. 6.2.1).

3.4.3 Final form of DRWP-Model for FCED work
Then the decided final form $M_{mn}(t)$ of DRWP-Model for the comparison with m-n baseline observation of EHT-Data for FCED work is

$$M_{mn}(t) \equiv Mod_p(t) = Mod(t,m\,n) \cdot cos\left[2\pi\frac{L_{Orb}}{L_{Sg}}(\hat{k}_1 + \kappa_r\hat{k}_2)\cdot\frac{(r_m - r_n)}{\lambda}\right]. \qquad (42)$$

We should refer eq.(41) and related equation for Mod(t,mn),and eqs.(26) and (29) for $\hat{k}_1 + \kappa_r\hat{k}_2$; we should also refer eq. (30) for $r_m - r_n$ .The descriptions relating from eq.(31) to eq.(40-2) are necessary for understanding the physical origin of time dependent varying characteristic of the visibilities. But we basically depend on the expression eq. (42) for DRWP-Model as practical numerical approaches in the present FCED.

4. Morphological Studies on Visibility of EHT- Data
4.1 Three Categories of Baseline Length
In Figure 4, we have plotted examples of the visibilities of EHT-Data released to the public [35]; these correspond to eq.

(4), taking j = EHT ; for plotting examples we have selected data from CASA data handling pipeline for 96 day (April 6, 2017) as examples. We divide the visibilities of EHT-Data into three categories depending on the observed baseline lengths: short baseline length, where the baseline length is less than 2 Gλ (λ: wavelength); medium baseline, where the baseline length varies as 2–6 Gλ; and long baseline, where the baseline length varies from 6 Gλ to ~8 Gλ. In Figure 4 in panel (A), two cases of short baseline length are indicated. From estimations relating to the deduction of Eq. (29), this category of baseline length corresponds to a source region wider than 25 AU at the Galaxy center. The time-varying features represented by these two plots give the

time variation of emissions at 1.3 mm-wavelengths via discrete forms, indicating the long-time characteristics of the variation of the back ground luminosity that reflects accreting condition of plasma around the Sgr A* at the center of the Galaxy.

Figure 4(B) presents examples of the time variation of visibilities in the category of medium baseline length. A remarkable gap is identified in the time-dependent variation between cases in the short baseline length category, indicating the spreading feature

time variability of visibilities. In the present study, to identify the morphological differences of the visibilities, we define the visibility for the short baseline category given in Panel (A) as "discrete visibility" and the visibility given in the Panel (B) as the "spreading visibility."

Considering eq.(29) with eq.(27), we conclude that the effective visibility is obtained for condition

$$\frac{-\pi}{2} < \Delta k_j \cdot (r_m - r_n) < \frac{\pi}{2}. \qquad (43)$$

The SMBHB orbit range of present interest is given by eq. (27) and yields the corresponding baseline length as

$$|r_m - r_n| \approx 3.13 \times 10^9 \lambda. \qquad (44)$$

Discontinuous changes of the morphological features from discrete to spreading visibilities can be understood as a result of focusing of the observation regions upon the SMBHB-associated range apart from a wide background which is one order of magnitude wider than the region occupied by the SMBHB's orbiting range.

4.2 The First Pilot Work for FCED
To investigate the dependence of the visibility amplitude upon the baseline length has a pilot role of the FCED (i.e., to find the

coincidence between the EHT data and DRWP-Model). That is, the variation of the visibility amplitude suggests that the level range of ~0.74 Jy (P-P), with a representative baseline length of $3.41 \times 10^9 \lambda$.

In Figure 4 in Panel(C), examples of the long baseline length category are presented. We see two cases of the spreading visibility for the LM-SP and AZ-SP baseline observations. The level ranges of spreading visibility for the AZ-SP baseline
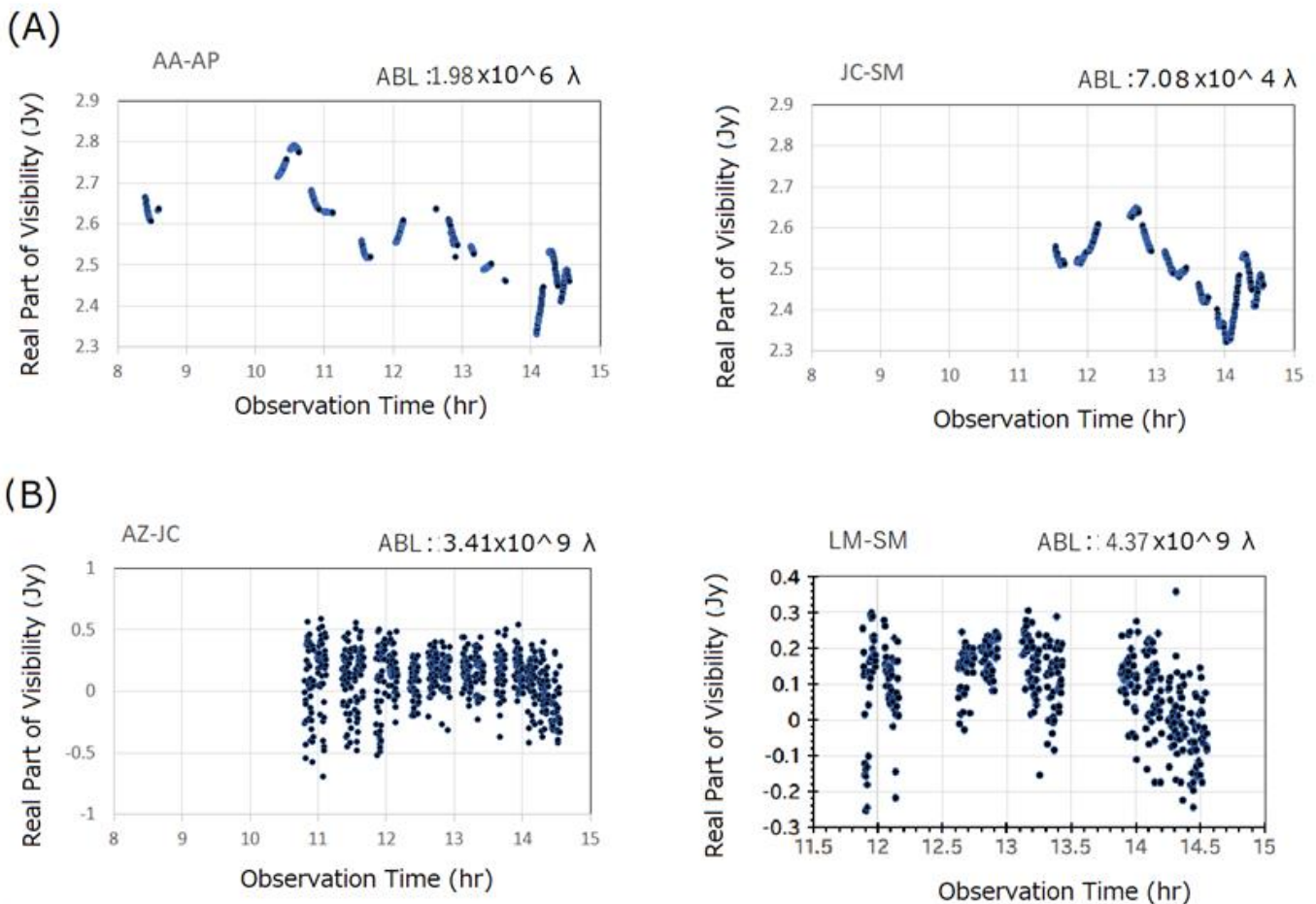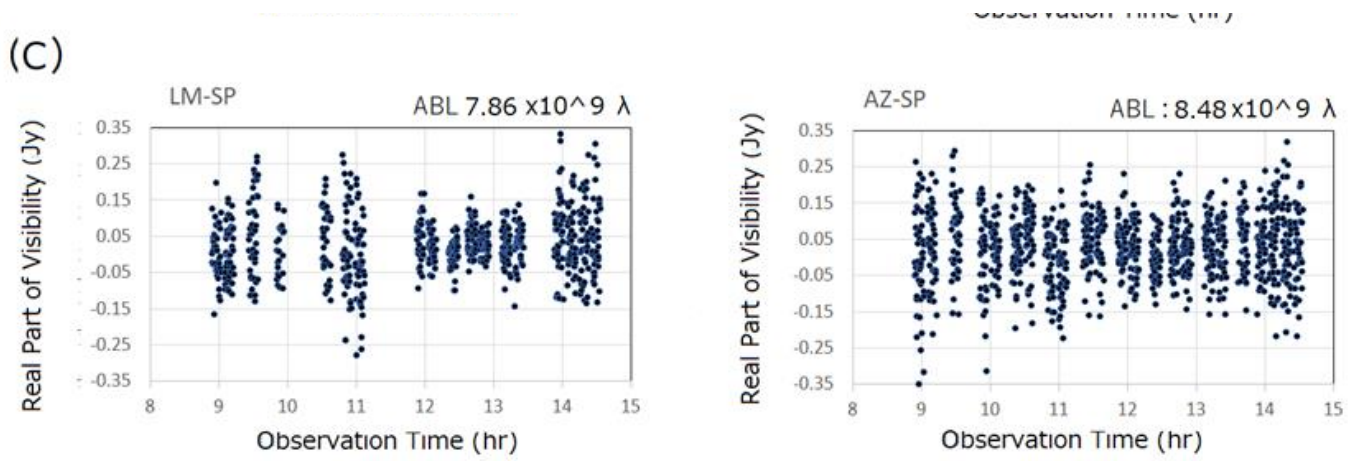
Figure 4: Time varying plots of VLBI visibilities obtained from the CASA pipeline data handling channel of EHT for observations on Day 96 (April 6, 2017). The data are plotted for two examples per each for the three categories of the baseline length from the VLBI baselines of EHT given in each corresponding diagram.

are reduced to about 0.35 Jy (on average) from the negative to positive peak (P-P) when compared with the case of the AZ-JC baseline observation; this case provides the spreading visibility which consists of a component of steady white noises and a component of periodic variation synchronized with the orbiting motion of the SMBHB. By focusing on the observation area at ~1/7, with respect to the baseline length from ~3×10^9 λ (the case of AZ-JC) to ~8×10^9 λ (the case of AZ-SP), the background white noise component is notably reduced (details are presented in Appendix C).

That is, for the case of the AZ-SP baseline, we obtain the source areas for the coherent visibility of the VLBI by dividing them into the noise source area S_N and the signal source area S_S for emissions modulated by SMBHB motions (hereafter referred to as the "SMBHB signal"). Radio-wave emissions are observed from the areas of white noise and area of SMBHB signals, with emission coefficients α_N and β_S, respectively. Then, the observed visibility can be expressed for the AZ-SP baseline by

$$\alpha_N S_N + \beta_S S_S = 0.35 \text{ (Jy).} \qquad (45)$$

In the case of the EHT-Data for the AZ-JC baseline, the coherent signal and noises are originated from an area seven times wider than that of the AZ- SP baseline observation. Then, the source area relation is expressed as

$$x S_N + S_S = 7(S_N + S_S), \qquad (46)$$

where x is the expansion factor of the background noise area under the expansion of the VLBI coherent observation area. Then, the observed amplitude of the visibility is given by

$$\alpha_N x S_N + \beta_S S_S = 0.74 \text{ (Jy).} \qquad (47)$$

To estimate the S/N ratio, we introduce a factor κ_e as the ratio of the radio emission coefficient in the SMBHB area to the emission coefficient in the background area, as

$$\beta_S = \kappa_e \alpha_N. \qquad (48)$$

As details are given in Appendix C. we obtain results for background noise $\alpha_N S_N$ and SMBHB signal $\beta_S S_S$ by solving eqs. (45) – (48) as a function of the ratio κ_e for the AZ-SP baseline observation, as

$$\alpha_N S_N = \frac{0.065 \cdot \kappa_e - 0.35}{(\kappa_e - 1)}, \qquad (49)$$

and

$$\beta_S S_S = \frac{0.285 \cdot \kappa_e}{(\kappa_e - 1)}. \qquad (50)$$

The source area of the background noise in the case of the AZ-JC baseline observation is larger, by factor x($=(7\alpha_N S_N+6 (\beta_S S_S)/\kappa_e)/(\alpha_N S_N)$:see eq.(47)), than that of the AZ-SP baseline observations.

Subsequently, we clarify that the S/N ratio R_{JC} revealed for observation of the AZ JC baseline, as expressed by $\beta_S S_S /\alpha_N x S_N$, is

increased to $R_{SP}=\beta_S S_S / \alpha_N S_N$, for the case of AZ SP baseline observations, owing to the increased baseline length from 3.4 G λ with respect to AZ JC to 8.5 G λ

Table 2   Signal (SMBHB) to Noise for AZ-JC and   AP-SM Baseline Observations

κ_e	R_{SP}	R_{JC}	$\beta_S S_S$	x $\alpha_N S_N$,	x
10	9.499	0.748	0.316	0.423	12.699
15	6.839	0.702	0.305	0.434	9.736
20	5.999	0.681	0.299	0.439	8.799
25	5.588	0.669	0.296	0.443	8.341
30	5.343	0.662	0.294	0.445	8.068
35	5.181	0.656	0.293	0.446	7.888
40	5.066	0.652	0.292	0.447	7.759
45	4.98	0.649	0.291	0.448	7.664
50	4.913	0.647	0.29	0.449	7.589
55	4.86	0.645	0.29	0.449	7.53

with respect to AZ SP. In Table 2, R_{SP} , R_{JC} , $\beta_S S_S$, x$\alpha_N S_N$, , and x are indicated as functions of κ_e. As details will be described in Sec.7 for the modified Fourier transformation (MDFT) method, for FCED, the signal to noise ratio R_{SP} of AZ-SP baseline observation on April 6 day observation is disclosed to be in a range around 5.6 ; that is, white noise emissions of about 15 % are mixed with emissions of about 85 % of the signal intensity which is modulated by the orbital motions of SMBHB. For this context, we understand from the results given in Table 2, that the S/N ratio R_{JC} for AZ-JC baseline observations is in a range centered around 0.67, where κ_e=25; we see that the emission mechanism in the SMBHB area has activity to emit 25 times more power than the background emissions per unit area. Because the observed background noise area is expanded by ~8.3 times compared to the AZ-SP baseline observations, the background noises in AZ-JC baseline observations occupy 60% of the detected total power, whilst the power of the SMBHB signal is 40%; i.e., the S/N ratio becomes 0.67.
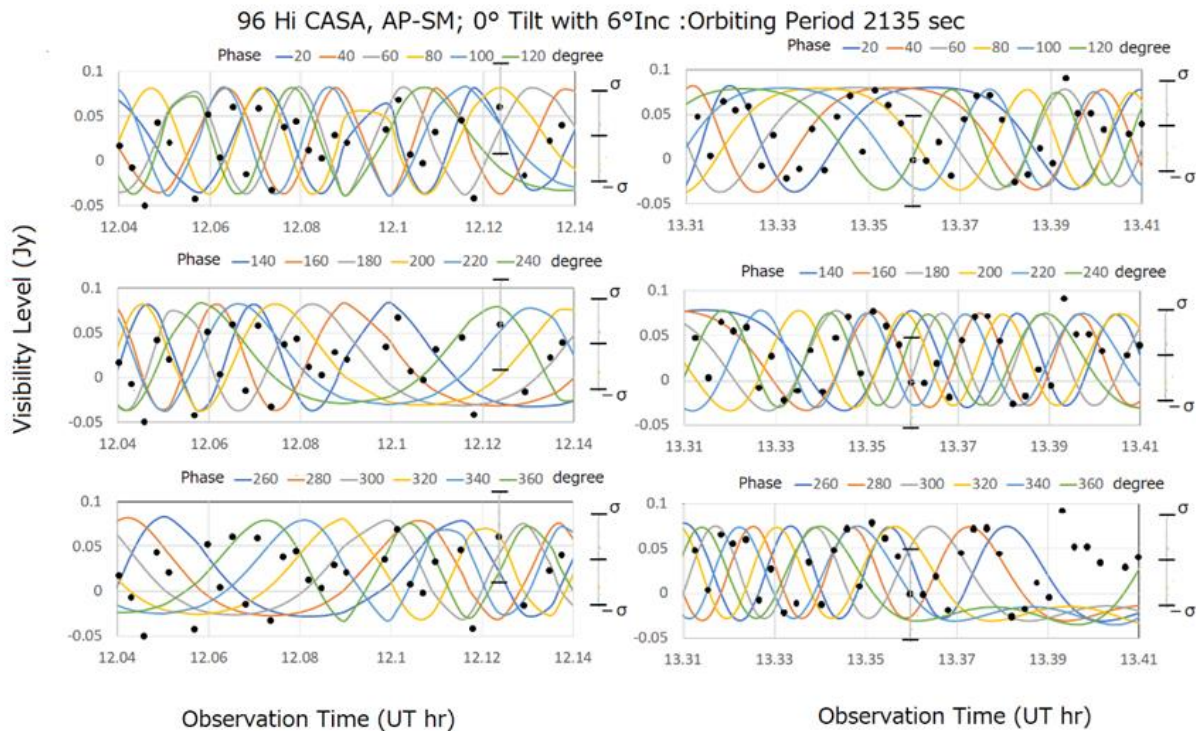
Figure 5. Examples of the EHT-Data and DRWP-Model plots for direct comparison. The EHT-Data for the Day 96 CASA AP-SM baseline are selected for two 6-min intervals from 12.04 to 12.14 UT hr and from 13.31 to 13.41 UT hr. The DRWP-Models calculated at the corresponding times in the EHT-Data are plotted together with the AP-SM baseline visibility data plots (EHT-Data). The plots of DRWP-Model are made by dividing the assumed initial phases of the orbiting SMBHB into three groups (20–120°, 140–240°, and 260–360°). In the EHT-Data plots, the individual error bars of the data are not indicated; however, the averaging error limit for all over the data group is indicated by positive and negative σ.

Even though the accuracy of present estimations is coarse, we can verify the presence of SMBHB effects as an initial step of FCED. In following Sections we confirm the existence of the SMBHB via two ways that reveal the existence of orbiting SMBHB through effective methods of FCED, i.e., by the direct comparison and MDFT methods.

5. Confirmation of SMBHB in EHT Data via Direct Comparison with DRWP-Model
5.1 Definition of Coincidence Index

To verify the existence of SMBHB orbits in the EHT-Data by finding the VSCATs in the observed visibilities, we continue the FCED via a direct comparison with the DRWP-Model described in Sec. 3. To this end, we have selected three example cases of spreading-type visibilities from the AP-SM, AZ-SP, and SM-SP baseline data for Day 96.

In Figure 5 plots of the observed visibilities are displayed together with plots of the DRWP-Model based on eq.(42), as an example case of the AP-SM baseline with assumed orbiting periods of 2135 sec and initial phase angles of 20–360°, in 20°
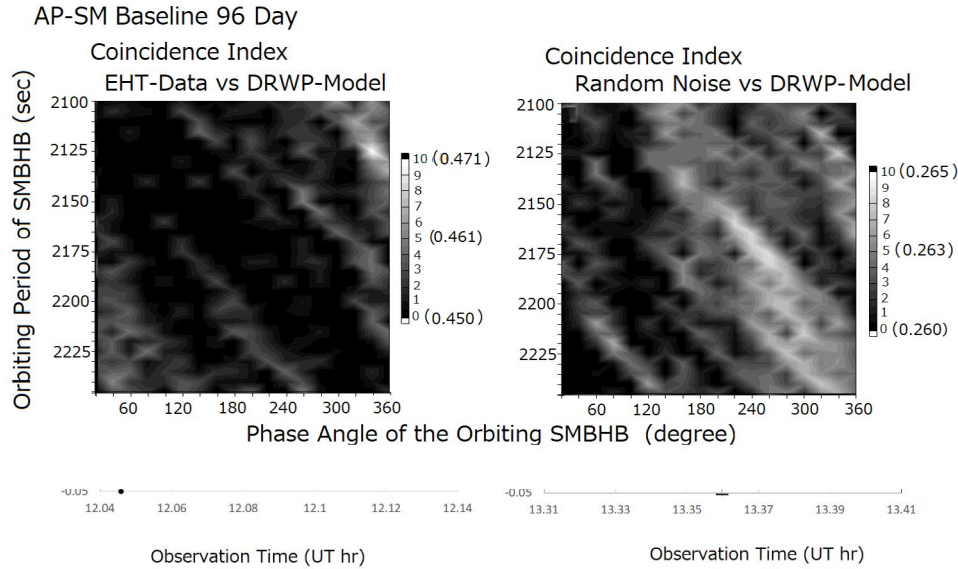
Figure 6. Two-dimensional displays of Ind_D and Ind_N for the comparison of the Day 96 AP-SM observation averaged 4-DATA from the EHT against the DRWP-Model, by setting a zero tilt angle ($\alpha = 0$) for the SMBHB orbital plane. In the left-hand panel, Ind_D is plotted as a function of the orbiting period (given in the ordinate) and the initial phase (given in the abscissa) of the two aligned SM-BHs in the DRWP-Model, to facilitate comparison with the EHT-Data. The index Ind_N that is calculated between the "quasi-random signal modulated by the EHT-Data sample timing" (QRN-EHT) and DRWP-Model is displayed in the right-hand panel, taking the same ordinate and abcissa as the left.

increments; the plots for the AP-SM baseline visibility data (EHT-Data) and DRWP- Model are made for two 6-min intervals from 12.04 to 12.14 UT hr and from 13.31 to 13.41 UT hr, on April 6, 2017. The plots of the DRWP-Model are constructed by dividing the initial phases of the orbiting SMBHB into three groups (20–120°, 140–240°, and 260–360°). To quantitatively evaluate the coincidence between the EHT Data and DRWP-Model, we define the coincidence index Ind_D as

$$Ind_D = \frac{1}{M} \sum_{m=1}^{M} exp\left[-\frac{1}{2}\left(\frac{x_{Dm} - x_{Mm}}{\sigma_m}\right)^2\right], \qquad (51)$$

where M is the total number of data for each subject under consideration, and x_{Dm} and x_{Mm} are the EHT-Data (under observation error rate σ_m) and DRWP-Model values which are given by eq. (42), respectively, at $t = t_m$. As a reference, we define another coincidence index Ind_N for the cases of coincidence between random noise and the DRWP-Model as

$$Ind_N = \frac{1}{M} \sum_{m=1}^{M} exp\left[-\frac{1}{2}\left(\frac{x_{Nm} - x_{Mm}}{\sigma_m}\right)^2\right], \qquad (52)$$

where x_{Nm} is the random noise level at t_m, formed by adjusting to overlap with the level ranges of the EHT-Data by using multiplication coefficients. The use of random noise as a reference is important to discriminate the difference between any meaningful sequences (e.g., sinusoidal wave variation) in the time series data; the significance is rather complicated in the EHT-Data case because the observation timing t_m is not a homogeneous period; however, the timing is synchronized with the observation DSTW (data sample time window). The DSTW of the EHT-Data is characterized by a quasi-periodic pause of ~1000 -1100 sec, which is accidentally close to the eclipse cycle of the two MS-BHs in the SMBHB. Because the time distribution of the random noise is set to be completely synchronized with the EHT-Data observation timings, it is neither completely random nor pure periodic; instead, it is modulated by the DSTW of the EHT-Data, which exhibits randomness only in the intensity level; we refer to this random signal as a "quasi-random signal modulated by the EHT-Data sample timing" (QRN-EHT).
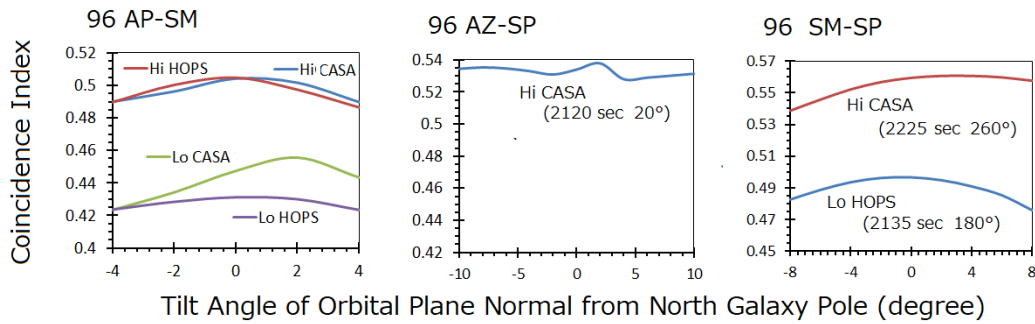
Figure 7. Coincidence index Ind$_D$ as a function of tilt angle α for the DRWP-Model, to facilitate comparison between the EHT-Data and DRWP-Model. The left-hand side panel shows the results of Ind$_D$ with respect to α for 4-DATA of Day 96 AP-SM baseline observations; most results, except for the case of the Lo CASA data, show the tilt angle α to be zero. The middle panel shows Ind$_D$ for the case of AZ-SP for the 96 Hi-CASA EHT-Data, compared against the DRWP-Model for a period of 2120 sec and a phase angle of 20° for the initial alignment of the two BHs. Though the dependence of coincidence index Ind$_D$ on the tilt angle of the orbital plane is weak, the result does not negate the conclusion of α=0±3°. In the right-hand panel, two cases of Ind$_D$ are displayed with respect to tilt angle α for the 96 SM-SP baseline data of the Hi CASA and Lo HOPS, compared with the DRWP-Model for the periods of 2225 sec ,with the initial phase angle 260,°and 2135 sec, with the initial phase angle of 180°; these results are also within a limit of α=0±3°.

5.2 Determining the Tilt Angle α of the Orbital Plane of the SMBHB

We have deferred to determine the tilt angle α of the orbital plane of SMBHB as unknown value. As a strategy, we first assume that the orbital plane is parallel to the equatorial plane of the milky way Galaxy; after we have achieved to find well fitting case in the processes of the FCED then we attempt to seek for the tilt angle α to determine the best fit cases of FCED.

As has been described in Sec 4, relating the Table 2, the signal to noise ratio is possibly in a range from 0.5 to 6. We may take, here, middle values from 1 to 2 which means almost same level of random noise emissions are existing together with coherent systematic variation level due to modulation by the orbital motion of SMBHB. Then we are required to have averages of the data which include independent noise to see resulting signals of SMBHB clearer. Using the DRWP-Model of α=0 orbital plane, then we have calculated fitting indices for four data of AP-SM observations of 96 day such as Hi-CASA, Hi-HOPS, Lo-CASA and Lo-HOPS (4 -DATA , hereafter).Then we average results of Ind$_D$ for the 4- DATA.

In Figure 6, two dimensional displays of Ind$_D$ and Ind$_N$ for the comparison of 4-DATA of AP-SM on 96 day observations of the EHT versus the DRWP-Model with 0 tilt angle (α=0) are given. In the left hand side panel, Ind$_D$ is plotted as function of the orbiting period (given in the ordinate) and initial phase (given in the abscissa) of the BHs alignment of SMBHB for DRWP-Model for comparison with EHT -Data, while Ind$_N$ that is calculated between QRN-EHT and DRWP-Model is displayed in the right-hand panel with the same ordinate and abscissa as the left-hand cases (show in two dimensions to facilitate comparison with DRWP-Model). Remarkably, a unique point is observed showing the maximum coincidence index Ind$_D$ when comparing the EHT-Data against the DRWP-Model for an orbiting period of 2135 sec and initial phase angle of 340°(in left panel); meanwhile, no such selected case can be found for the comparison between QRN-EHT and the DRWP-Model (right panel). This suggests that we can seek meaningful signatures in the observed visibilities of EHT-Data, to verify the existence of the SMBHB's motion.
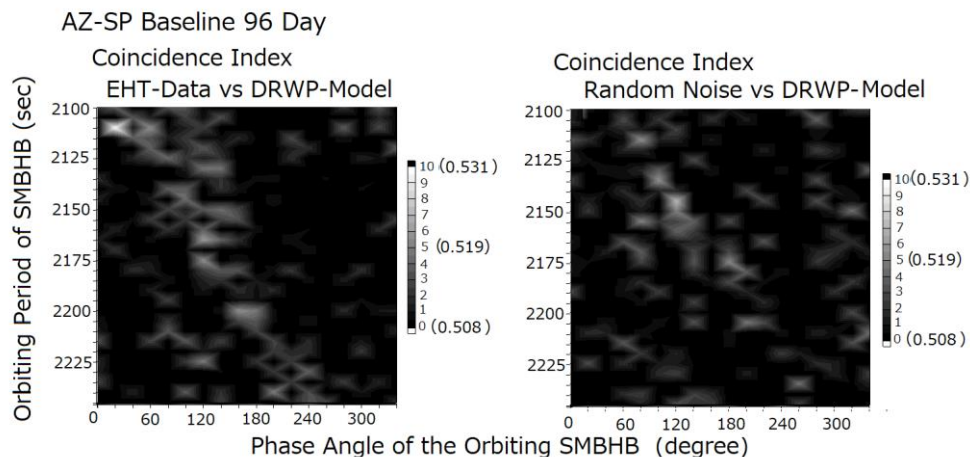
Figure 8. Same with Figure 6 for the averaged 4-Data of the AZ-SP base line observation. We can see a single maximum spot of the coincidence at 2110sec with phase 20.°

After this confirmation of the signature of the SMBHB motion, we have decided the tilt angle α of the SMBHB's orbital plane by finding the maximum Ind_D value, by sweeping α in the DRWP-Model, given by eq. (42), where the $\hat{k}_1 + \kappa_r\,\hat{k}_2$ vector is controlled by the angle α via eq. (26). In Figure 7, the coincidence indices Ind_D are displayed as a function of the tilt angle α of the DRWP-Model, to facilitate comparison with the EHT-Data. The left-hand side shows the results of Ind_D with respect to α for the 4-DATA for Day 96 AP-SM baseline observations; for most results except for the case of the Lo CASA data, which indicate a maximum Ind_D at α=-2°, the maximum Ind_D occurs at α = 0. Furthermore, two data, Hi CASA and Lo HOPS of SM-SP baseline observations, indicate a clear dependence of the coincidence index on the tilt angle α, showing that the correct tilt angle of the orbital plane can be expressed as α =0°±3°. As shown in the middle panel of Figure 7, the dependence of AZ-SP on the tilt angle α is slight and unclear; it is considered to be attributable to the low S/N ratio and does not negate the result of α =0°±3°.
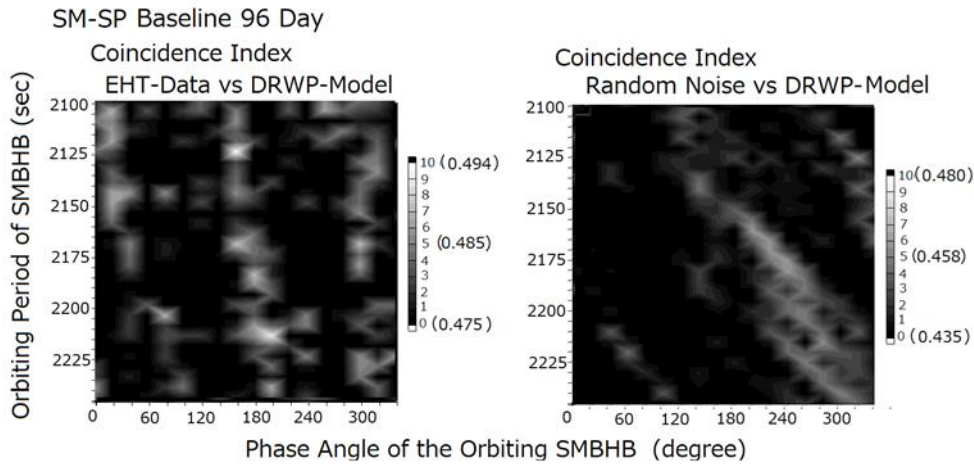
Figure 9. Same with Figure 6 for the average of 4-Data of the SM-SP base line observation. The maximum spot of Ind_D is at 2125sec of the orbital period with initial phase angle of 180°; there is the second peak at 2210 sec (phase angle 200°) with the coincidence index 0.492 close to the coincidence index 0.494 of the first peak.

5.3 Direct Comparison of the EHT-Data and DRWP-Model
We further have applied the method of the direct comparison of the EHT-Data and DRWP-Model to the case of Day 96 AZ-SP and SM-SP baselines taking the tilt angle α = 0 as the real case. As shown in Figure 8, we can see a single maximum spot of coincidence at 2110 sec with phase 20°. In the case of Figure 9, the maximum spot for Ind_D is at 2125 sec of the orbital period and an initial phase angle of 180°; the second peak appears at 2210 sec with a coincidence index 0.492, close to the coincidence index 0.494 of the first peak.

During the processes of these calculations of the coincidence index Ind_D for the direct comparison of the DRWP-Model and EHT-Data for Day 96 AP-SM, AZ-SP, and SM-SP baselines, we can verify the tilt angle α of the SMBHB's orbital plane as the results are given in Figure 7. Thus, we see that the direct comparison method between the EHT-Data and DRWP-Model can express the geometric features of the orbital plane of the SMBHB, along with the orbiting period; however, calculation of the coincidences is subjected to the low S/N ratio (~0.5–6); reflecting low signal to noise ratio, as a result, the coincidence indices Ind_D and Ind_N show close values.

$$d(t) = p(t) \cdot s(t). \qquad (53)$$

We have obtained the orbital period of the SMBHB by the direct comparison for the EHT-Data of Day 96 for AZ-SP, SM-SP, and AP-SM baselines. These are worthwhile as providing the pilot role to search for the existing SMBHB effects. Because no quantitative approach to avoid the disturbance of large co-existing quantities of noise in the direct comparison method, however, we concentrate upon the analyses using the MDFT (modified Fourier transformation) for determining the orbital period of the SMBHB, as described in Secs. 6 and 7.

6. Confirmation Method of The Orbital Period of SMBHB by Fourier Transformation
6.1 Fourier Transformation under the Effects of the DSTW
The VLBI observations for the EHT-Data are characterized by quasi-periodic sampling time windows. We would therefore obtain misleading results regarding the periodicity of the phenomena if we apply a simple Fourier transformation to the published data (without attending to the effects of DSTW modulation). That is, observed visibility data *d(t)* are expressed via a physical component *p(t)* and data sampling window *s(t)* as

Then, the Fourier transformation is expressed via the convolution form of two intrinsic Fourier-transformed functions $P(\omega)$ and $S(\omega)$ that correspond to *p(t)* and *s(t)*, respectively; thus,

$$D(\omega) \equiv P(\omega) * S(\omega) = \frac{1}{2\pi}\int_{-\infty}^{\infty} P(\xi) \cdot S(\omega - \xi)d\xi. \qquad (54)$$

In addition to the artificially modulated sampling window there are remarkably large white noise component associated with the coherent orbital modulation of SMBHB.

To eliminate the effects of white noise spectra of emissions from SgrA* then, we utilize the spectra of white noise modulated by data sampling window (QRN-EHT, see Sec.5).

When we apply the group of random noise $n_G(t)$, averaged for M set, that is expressed by ,

$$n_G(t) = \frac{1}{M} \sum_{j=1}^{M} \sum_{i=1}^{K} n_{ij} \delta(t - t_{ij}) , \qquad (55)$$

with random levels n_{ij} and random times t_{ij}, as $p(t)$ in eq.(53), the Fourier transformed spectra function $D_n(\omega)$ corresponding to the random noise group $n_G(t)$ is expressed by

$$D_n(\omega) = \frac{1}{M} \int_{-\infty}^{\infty} \sum_{j=1}^{M} \sum_{k=1}^{K} n_{jk} \delta(t - t_{jk}) s(t) e^{-i\omega t} dt . \qquad (56)$$

This relation eq.(56) can be rewritten in the form of average of discrete Fourier transformed formulae in M random noise groups (see Appendix D), as

$$D_n(\omega) = \frac{1}{M} \sum_{j=1}^{M} \sum_{k=1}^{K} \bar{n}_j \, s(t_k) e^{-i\omega t_k} \Delta t . \qquad (57)$$

where $\bar{n}_j$ is average level of the noise group j; $t_k = k \, \Delta t$ for $\Delta t = T/K$ for sufficiently large time interval T and sufficiently large sampling number K. When we select the random noise group where the average of the noise levels are equal to N_L, $D_n(\omega)$ is expressed by

$$D_n(\omega) = N_L S(\omega) . \qquad (58)$$

In the case of the observed EHT visibilities, we can consider that $p(t)$ in eq.(53) consists of random noise $n(t)$ and non thermal component $p_s(t)$ where a systematic VSCAT is included; that is, data $d(t)$ are expressed by

$$d(t) = [p_s(t) + n(t)] \cdot s(t) . \qquad (59)$$

By the Fourier transformation of the visibilities then we have the results as

$$D(\omega) = P_s(\omega) * S(\omega) + N_L S(\omega) . \qquad (60)$$

By using relation given in eq.(58) we can obtain the Fourier transformed DSTW corresponding to the visibility of each pair baseline of EHT; that is, by applying the Fourier transformation to the group of random noise under the constraint of the DSTW which is exactly same with the case of EHT observations, we have the Fourier transformation of QRN-EHT. Then for $S(\omega)$, we take results of the Fourier transformation $Dn(\omega)$ obtained from 10 sets (selecting M=10 in eq.(57)) of QRN-EHT ; that is

$$S(\omega) = D_n(\omega)/N_L . \qquad (61)$$

In the present work, we calculate only the absolute values of the Fourier transformed function; when we divide both sides of eq.(60) taking the absolute value , then, it follows that

$$\frac{|D(\omega)|}{|S(\omega)|} = \frac{|P_s(\omega) * S(\omega)|}{|D_n(\omega)|/N_L} + A(\omega) + N_L . \qquad (62)$$

where $A(\omega) = \{|P_s(\omega) * S(\omega) + N_L S(\omega)| - (|P_s(\omega) * S(\omega)| + N_L |S(\omega)|)\}/|S(\omega)|$.

In parallel to this data handling processes to the visibilities observed by EHT (EHT-Data), we prepare Fourier transformation of the constructed DRWP-Model, $Mod(\omega)$ corresponding to eq.(42) with the DSTW that is completely same with the case of the visibilities observation by EHT; that is,

$$Mod(\omega) \equiv Mod_p(\omega) * S(\omega) = \frac{1}{2\pi} \int_{-\infty}^{\infty} Mod_p(\xi) \cdot S(\omega - \xi) d\xi. \qquad (63)$$

where $Mod_p(\omega)$ is the proper spectrum of DRWP-Model.
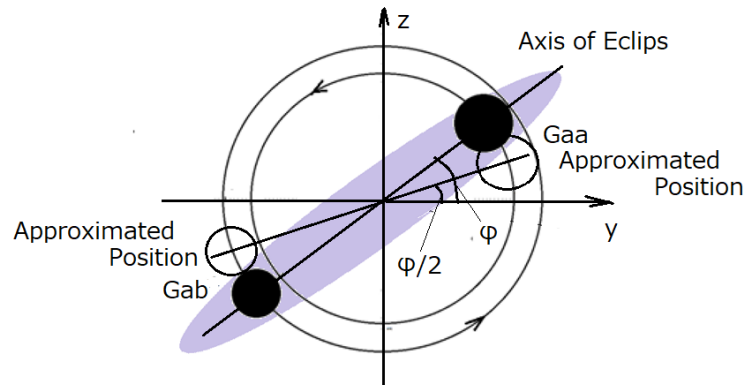
Figure 10. Geometry of eclipse approximation for DRWP-Model. The positions of individual SMBHs are assumed to be shifted from the real eclipse alignment by an angle $\varphi/2$.

When we divide the results $Mod(\omega)$ by spectra of DSTW, then, it follows that

$$\frac{|Mod(\omega)|}{|S(\omega)|} = \frac{|Mod_p(\omega) * S(\omega)|}{|D_n(\omega)|/N_L}. \tag{64}$$

Finally by comparing the two deduced functions, in eqs.(62) and (64), which consist of three Fourier transformed functions $P_s(\omega)$, $D_n(\omega)$ and $Mod_p(\omega)$ we can confirm the coincidence of the phenomena given by $P_s(\omega)$ for the EHT-Data with the prepared DRWP-Model ; that is , we can find coincidence of $P_s(\omega)$ and $Mod_p(\omega)$ in the form,

$$\frac{|D(\omega)|}{|S(\omega)|} - (A(\omega) + N_L) = \frac{|Mod(\omega)|}{|S(\omega)|} . \tag{65}$$

In real procedure , we are required to separate VSCAT spectrum from other non thermal spectra $D_B(\omega)$. Further, because the level of EHT Data , amplitude of DRWP Model and amplitude of QRN-EHT are independently generated quantities, we should adjust multiplying coefficients as close to each other as possible. Then, we set two parameters α_D and α_M to accomplishment of eq.(65) as

$$\frac{|D(\omega)|}{|D_n(\omega)|} - \alpha_D = \alpha_M \frac{|Mod(\omega)|}{|D_n(\omega)|} . \tag{66}$$

where

$$\alpha_D = 1 + \overline{A(\omega)}/N_L . \tag{67}$$

That is, we define a constant α_D that consists of a noise level factor N_L and noise affected unknown excess values $\overline{A(\omega)}$ which are approximated by taking average in the concerned analyzing period range. Further in eq.(66), α_M is the coefficient resulted from adjustment of the amplitude of Mod(ω) spectrum. We denote the terms, $|D(\omega)|/|D_n(\omega)|$ and $|Mod(\omega)|/|D_n(\omega)|$ in eq. (66) as the MDFTs (modified Fourier transformation) for EHT-Data and MDFT for DRWP-Model, respectively.

6.2 Fourier Transformation of DRWP-Model
6.2.1 Eclipse approximation model
As we have recognized in Sec. 5 for the study of the direct comparison of the EHT-Data with DRWP-Model which shows orbital motion and eclipse effects of two SMBHs, the parameter of the initial phase of the orbit to identify positions of the SMBHs is crucial to discuss the coincidence of the Data and Model;

and results of comparison is fairly obscured by existing random varying noise components associated with the observed visibilities. In this Fourier transformation approach, we concentrate on the identification of the orbiting periods of SMBHB using absolute function of Fourier transformation by sacrificing the phase components; by this selection, confirmation of the coincidence of the EHT-Data and DRWP-Model becomes clear by avoiding the disturbances of the noise components. In this selection we are not required to set initial phase of the orbital motion in DRWP-Model.

For this approach, however, we are required to employ an approximation that we call here "eclipse approximation". We here consider a case of time t dependent sinusoidal functions $f(t)$ which appear in DRWP-Model as combination of terms, as

$$f(t) = A[\cos(\Omega_{Orb}t + \varphi_{Orb}) + \kappa\cos(2\Omega_{Orb}t + \varphi_{Orb})]$$
$$- B[\cos(\Omega_{Orb}t + \varphi_{Orb}) + \kappa\cos(2\Omega_{Orb}t + \varphi_{Orb})]. \tag{68}$$

where the term with $\Omega_{Orb}\,t+\varphi_{Orb}$ in the argument of the function is for orbital motion of the SMBHs and the term with $\cos(2\Omega_{Orb}\,t+\varphi_{Orb})$ in the argument of the function is for ecliptic effects, of SMBHB, that occur twice during one orbital rotation. A and B in eq. (68) are time independent coefficients that appear in equations from eq.(9) to eq.(11) and eqs.(41) and (42). In this model of the eclipse approximation, we change eq. (68) to following form, $f_a(t)$, as

$$f_a(t+\tau) = A[\cos(\Omega_{Orb}t + \varphi_{Orb}/2) + \kappa\cos(2\Omega_{Orb}t + \varphi_{Orb})]$$
$$- B[\sin(\Omega_{Orb}t + \varphi_{Orb}/2) + \kappa\sin(2\Omega_{Orb}t + \varphi_{Orb})]. \qquad (69)$$

where $\tau = \varphi_{Orb}/2\Omega_{Orb}$.

By this approximation, then, we are not required to select φ_{Orb} value in the resulted absolute value of the Fourier transformation as reasoning is given below.
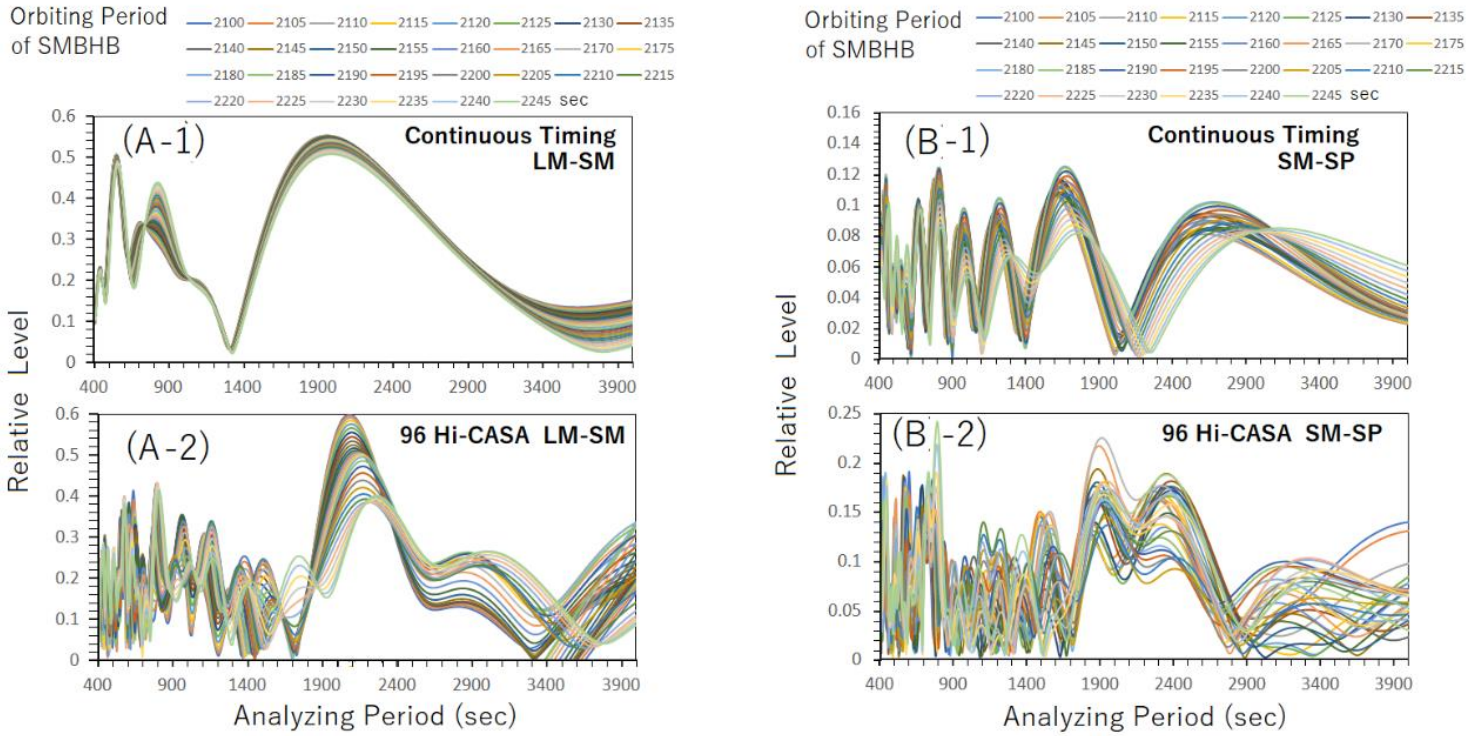
Figure 11. Absolute values of results of Fourier transformation with respect to the DRWP-Model expressed by eq.(42), employing the eclipse approximation to reduce the phase parameter , (see Sub Sec. 6.2.1)), corresponding to two examples of the EHT-Data obtained by baselines LM-SM (panel (A-1) and (A-2)), and SM-SP (panel(B-1) and (B-2)). Results of DRWP-Model corresponding to the medium length baseline LM-SM are given for the model function sampled with homogeneous sampling timing of 10 sec interval (Proper Spectra) in panel (A-1), and for the model function sampled with the specific timing synchronized with DSTW of EHT-Data (DSTW Spectra) in panel (A-2). In panels (B-1) and (B-2) results for the long length baseline SM-SP are given for the Proper Spectra and DSTW Spectra of DRWP-Model respectively. The Fourier transformed results given with relative level resulted from the amplitude between -1 to 1 of the model function are given versus the analyzing periods, with unit sec, given in the abscissa of all panels from 400 sec to 4000 sec; in each panel, all 30 cases of the orbiting period of SMBHB of the DRWP-Model are plotted with corresponding colors given in the top part of the diagram.

That is, the Fourier transformation $F(\omega)$ is expressed by

$$F(\omega) = \int_{-\infty}^{\infty} f_a(t+\tau)e^{-i\omega t}\,dt = \int_{-\infty}^{\infty} f_a(\xi)e^{-i\omega(\xi-\tau)}\,d\xi = F_a(\omega)e^{i\omega\tau}. \qquad (70)$$
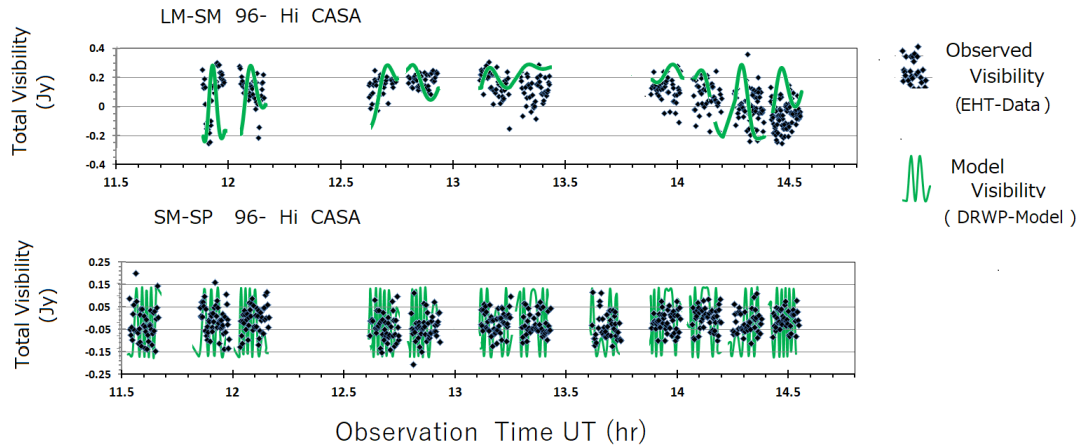
Figure 12. Real time plots of EHT Data from Day 96 Hi CASA pipeline for two example observations by LM SM baseline and SM SP baseline where all EHT Data and DRWP Model are plotted corresponding to the EHT observation times given by UT with hour unit. The observations are made intermittently with characteristic time window (DSTW) . The calculated points of DRWP Model (green curves) for example cases with SMBHB orbiting period, T_{orb}=2195 sec, and with the initial phase angle φ_{Orb}=20 deg are plotted as example case ; the generation timing of the DRWP Model is synchronized with DSTW of the EHT observation though the plots are made with continuous curves.

When we rewrite $F_a(\omega)$ with absolute value $|F_a(\omega)|$ and phase function $\theta(\omega)$, it follows that

$$F(\omega) = |F_a(\omega)| \cdot exp[i(\theta(\omega) + \omega\tau)]. \qquad (71)$$

From this expression, we can easily conclude that $|F(\omega)|$ is completely free from τ.

In this case of eclipse approximation the geometrical relation of the SMBHs relative to the real alignment of SMBHB is depicted in Figure 10. Because no harmful change is made to the orbital motions and also for orbiting period at all, we are allowed to apply this model for simplicity by avoiding to introduction of additional parameters such as the initial phase for orbits of the SMBHB.

6.2.2 Features of Fourier transformation of DRWP-Model
Before progressing to the FCED (comparison of the EHT-Data with the DRWP-Model), we here display the result of analyses of Fourier transformation and MDFT for DRWP-Model corresponding to two selected EHT-Data observed by the baselines LM-SM and SM-SP. In Figure 11, the absolute values of results of Fourier transformation with respect to the DRWP-Model expressed by eq.(42), employing the eclipse approximation to reduce the number of parameter, as describing in Sub Sec. 6.2.1, are displayed corresponding to two examples of the EHT-Data obtained by baselines LM-SM (panel (A-1) and (A-2)), and SM-SP (panel(B-1) and (B-2). The Fourier transformed results given with relative level resulted from the amplitude between -1 to 1 of the model function are given with respect to the analyzing periods, with unit sec, given in the abscissa of all panels from 400 sec to 4000 sec; in each panel, all 30 cases of the orbiting period of SMBHB of the DRWP-Model are plotted with the corresponding colors given in the top part of the diagram. In panels (A-1) and (A-2) results for the medium length baseline LM-SM are given respectively for the model function sampled continuously at 10 sec interval (Proper Spectra), and that for the model function sampled with the specific timings synchronized with the DSTW of EHT-Data (DSTW Spectra).

The Proper Spectra given in panel (A-1) is a manifestation of the complicated time dependent variation of the DRWP-Model expressed by from eqs. (33) to (40); the principal feature of this Proper Spectra is represented by a large peak centered around 2000 sec suggesting the correspondence to the orbiting period of the DRWP-Model but the peak periods are not exactly showing orbiting periods. The frequencies corresponding peaks of the Proper Spectra are modified through interaction of complicated coupling processes given in eqs. (33) ~ (40). In shorter period range than the orbiting period, we can see three peaks with periods given as higher harmonics of modified orbiting periods caused by nonlinear characteristic, of the visibility function, which is also expressed by eqs. (33) ~ (40). In panels (B-1) in Figure 11, results for the long length baseline SM-SP are given for the Proper Spectra . Different from the case of medium range of baseline length, the spectra become complicated with 8 peaks as results of expanded baseline length. Even the principal peak which would reflect the orbiting periods of SMBHB model shifts largely towards the side of the longer analyzing period which suggest modification of angular velocity Ω_{orb} of the orbiting SMBHB to $\Omega_{orb}-m\Omega_e$ under the effect of the earth rotation with angular velocity Ω_e (m is arbitrary integer below 6) in the model function corresponding to equations from eqs.(33) ~ (40). To show real time features of the DSTW (see SubSec 6-1) before the Fourier transformation, we have plotted EHT-Data in Figure 12, together with DRWP-Model as the function of real time. Though DRWP-Model is connected by continuous curves the sampled values for the Fourier calculation are completely synchronized with the DSTW of EHT-Data. It is remarkable that the EHT-Data and the DRWP-Model are sampled with the timings same with the DSTW of the EHT observation with pauses of some characteristic periods around 1000 sec to 1100sec . By this quasi periodic sampling interval the Fourier transformation

of EHT-Data and also synchronized sampling DRWP-Model are largely altered from the Proper Spectra in panel (A-1) to the DSTW affected Spectra in panel (A-2) for LM-SM baseline data, and from the Proper Spectra in panel (B-1) to DSTW affected Spectra in panel (B-2) for SM-SP baseline data. In the process of the comparison of the Fourier transformation of EHT-Data and DRWP-Model then we use spectra largely affected by DSTW rather than the usage of direct Fourier transformation, as has been explained in Sub Sec. 6.1.
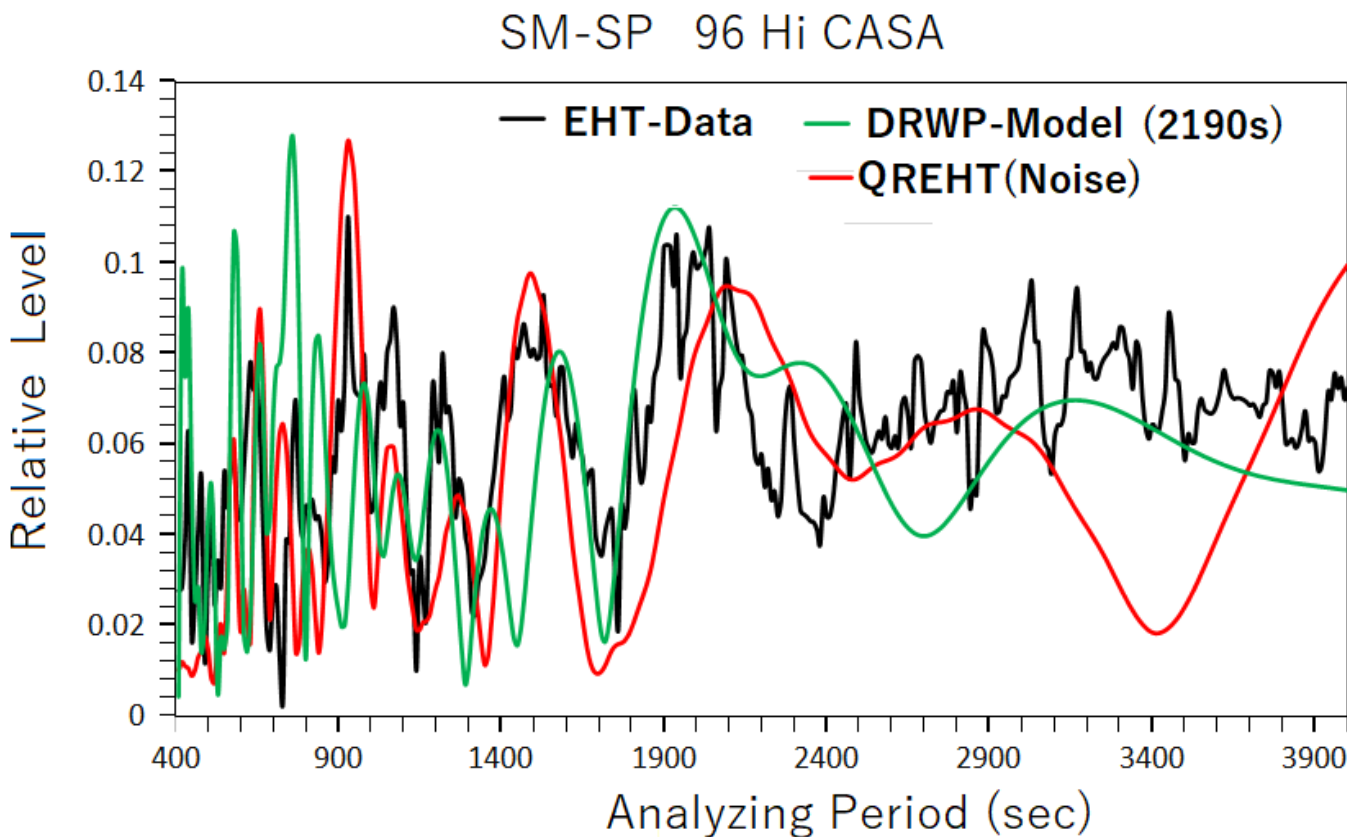
Figure 13. Absolute values of Fourier transformation results under the constraint of the common DSTW of the EHT-Data, Day96 Hi-CASA, SM-SP baseline with respect to the analyzing period, $2\pi/\omega$ ranging from 400sec to 4000sec. Results are indicated for EHT-Data(black curves; as D(ω) corresponding to eq.(60)), for DRWP-Model (green curve; as Mod(ω) corresponding to eqs. (42) and (63)) and QRN-EHT (DSTW controlled random noises) S(ω) (red curve; corresponding to eqs.(56) to (58)). DRWP-Model, Mod(ω) is selected as a representative orbiting period of 2190 sec from 30 periods in a range from 2100 to 2245 sec prepared in DRWP-Model as parameters.

6.2.3 Significance of the sensitive dependence on the orbiting period of SMBHB

Seeing Figure 11 where the results of the Fourier transformation of DRWP-Model, under the constraint of DSTW are displayed, we emphasize that though proper Fourier transformed results are altered due to convolution effects with DSTW spectra, the Fourier transformed DRWP-Model shows extremely clear dependence on the parameters of the orbitals period of SMBHB through entire period range of the spectra. It is promised that we can select correct orbiting period of SMBHB from the EHT-Data by identifying coincidences with DRWP-Model. As given in eq. (66) we use the MDFT for FCED processes where the DSTW modulated proper spectra for EHT-Data and DRWP-Model are compared in the form of MDFT with adjustment by relatively set coefficients α_D and α_M. Under such modification and adjustment, however, it is significant that there remain sensitive dependence on the SMBHB orbiting period in the MDFTs for DRWP-Model. Thus we can complete FCED by selecting the best fitting pa-

rameter in DRWP-Model with the EHT-Data that is also modified as MDFT with the same algorism to have MDFT for the DRWP-Model.

7 Comparison of EHT-Data and DRWP-Model via Fourier Transformed Function
7.1 General

To apply the Fourier transformation method to the FCED (find coincidence of the EHT-Data with DRWP-Model), we selected five cases of the baselines of EHT observations; two of these are AZ-SP and SM-SP which have long baseline length around 8 Gλ range and another two cases are AZ-SM and LM-SM which have medium baseline length around 3 to 4 Gλrange. As a short baseline case we have selected the data of AZ-LM with the baseline length around 1 Gλwhich is scarcely out of the limiting zone to detect the orbit of SMBHB. Hereafter we will follow the processes given in Sub Sec.6.1 for comparison of EHT-Data and DRWP-Model with selected observation data (EHT-Data).
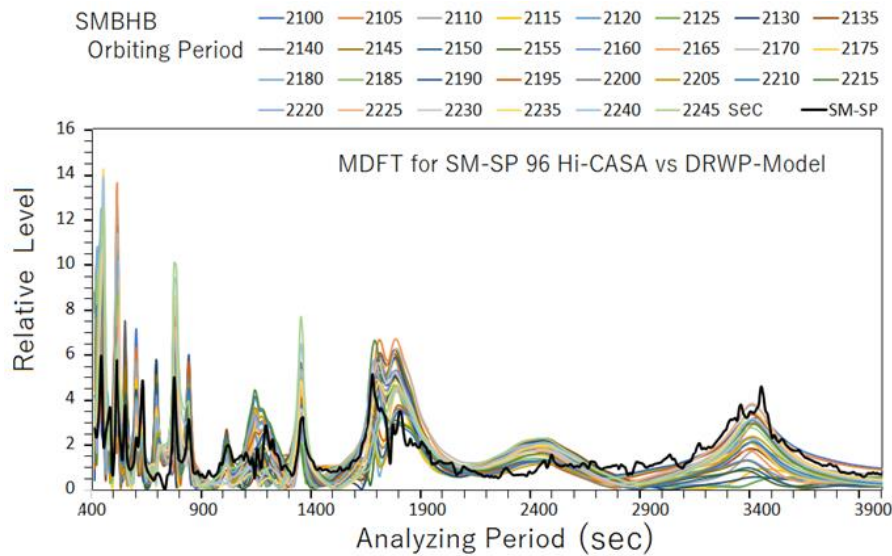
Figure 14. Comparison of the modified Fourier transformed functions (MDFT) $|D(\omega)|/|S(\omega)|$ for EHT-Data (black curve) and MDFT, $|Mod(\omega)|/|S(\omega)|$ for DRWP-Model with 30 orbiting periods of SMBHB (given by corresponding colors). Results are displayed for the FCED as function of the analyzing period, $2\pi/\omega$ ranging from 400sec to 4000sec.

7.2 The Case of Day 96 Hi-CASA SM-SP baseline data

In Figure 13, comparisons of the direct Fourier transformation results under the constraint of the common DSTW are displayed with respect to analyzing periods from 400sec to 4000sec, for EHT-Data(black curves) as $D(\omega)$ corresponding to eq.(60), for DRWP-Model (green curve) as $Mod(\omega)$ corresponding to eqs. (42) and (63) and QRN-EHT (DSTW controlled random noises) $S(\omega)$ (red curve: averaged for 10 cases after Fourier transformation) corresponding to eqs.(56) ~ (58). The direct Fourier transformation of DRWP-Model, Mod(ω) is selected for period 2190 sec as a representative orbiting period from prepared 30 orbiting periods in a range from 2100 to 2245 sec. The features of three Fourier transformation results show similar trend with respect to the analyzing periods arising from common DSTW effects and from random noises associated with EHT-Data because of low signal to noise ratio in a range from 0.5 ~ 6 (See Secs,3 and 5); similarity between black and red curves becomes clear in the analyzing period 900 to 1500 sec. Though we may state rough similarity between the three results, however, no clear conclusion is able to be drawn because the displayed spectra of EHT-Data and DRWP-Model are resulted from the convolution between each proper spectrum and the Fourier transformation of DSTW, $S(\omega)$ that is proportional to the spectra of QRN-EHT whose occurrence are synchronized with DSTW (see eq.(61)). For the complete confirmation of the results towards the FCED, we are required to have a sophisticated handling of Fourier transformed function as given by eq.(66). To pursue this processes we calculated MDFT (see Sub Sec.6-1) both for direct Fourier transformation $D(\omega)$ for EHT-Data (see eq.(62)) and direct Fourier transformation Mod(ω) for DRWP-Model (see eq.(64)).
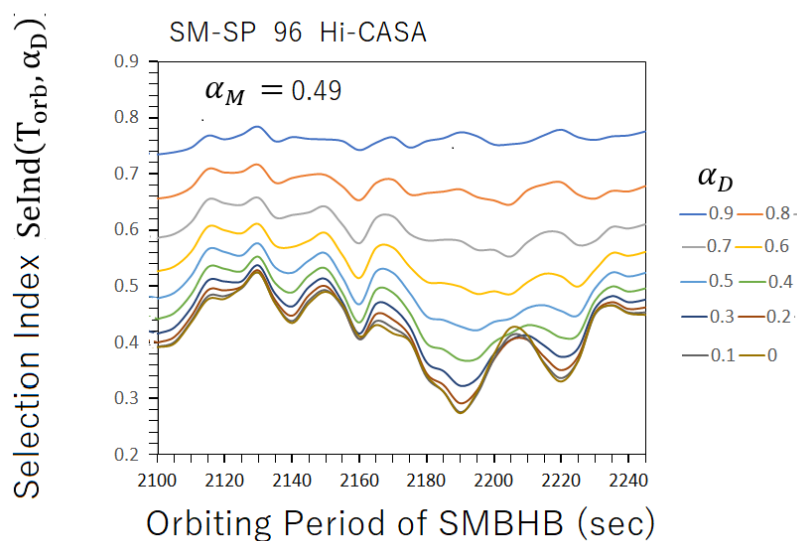
Figure 15. Selection index SeInd to evaluate the coincidence of MDFT for EHT-Data and MDFT for DRWP-Model. Calculated SeInds are displayed versus the orbiting period of SMBHB taking noise reduction coefficient α_D as parameter by adjusting coefficient α_M to be 0.49 to make the level of EHT-Data equal to the amplitude of DRWP-Model. The results show that the best fit condition between EHT-Data and DRWP-Model occurs at the orbiting period of 2190 sec for α_D=0 ~0.1.

In Figure 14, we plot the MDFT for EHT-Data together with the MDFT for DRWP-Model with 30 cases of the orbiting periods of SMBHB of the DRWP-Model. We can see clear similarity here, between the MDFTs for EHT-Data and DRWP-Model. And these results show possibility that we are able to select a parameter of the orbiting periods from given 30 cases to find the best fitting orbiting period. Thus, to evaluate the coincidence of the MDFT for EHT-Data versus the MDFT for DRWP-Model associated with 30 cases of the orbiting periods from 2100 sec to 2245 sec, we define the selection
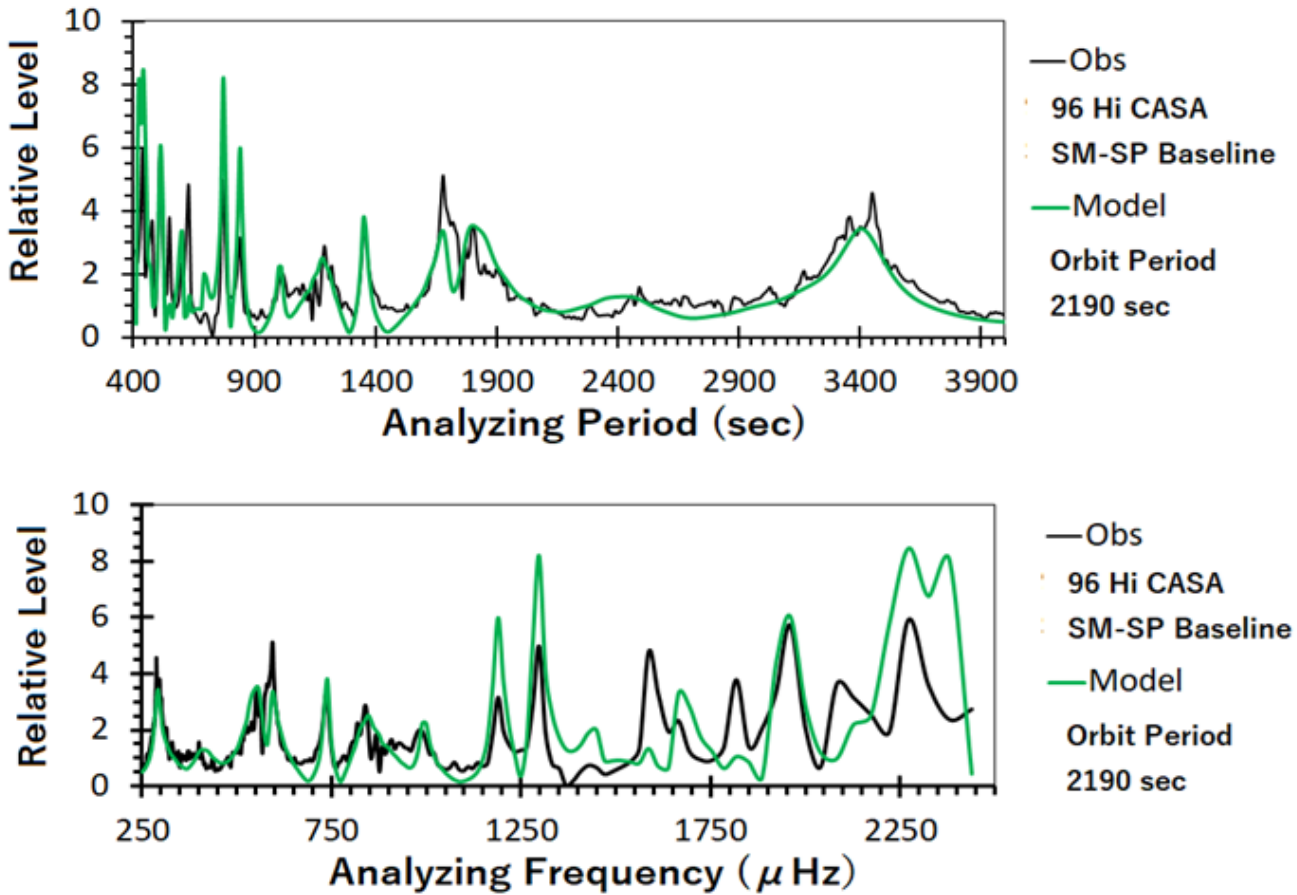
Figure 16. Final results showing coincidence of the MDFT for EHT-Data (black curve) and the MDFT for DRWP-Model (green curve). Via the identity of the results, it can be concluded that the EHT-Data have definitely the component of the steady time variation coinciding with the SMBHB orbiting period of 2190 sec prepared in DRWP-Model.

index SeInd ,as

$$[\text{SeInd}(T_{orb}, B_r)]^2 = \frac{1}{M} \sum_{m=1}^{M} \frac{\left\{\left[G_{EHT}\left(T_0 + T_m\right) - \alpha_D\right] - \alpha_M G_{Mod}\left(T_0 + T_m, T_{orb}\right)\right\}^2}{\left[G_{EHT}\left(T_0 + T_m\right) - \alpha_D\right]^2 + \left[\alpha_M G_{Mod}\left(T_0 + T_m, T_{orb}\right)\right]^2}. \qquad (72)$$

where $G_{EHT}.(T_0 + T_m)$ and $G_{Mod}.(T_0 + T_m, T_{orb})$ are MDFT s for EHT Data and for DRWP Model as the function of analyzing period of $T_0 + T_m$ sec respectively; for DRWP Model 30 functions are expresses with corresponding orbiting period T_{orb}. The both functions $G_{EHT}.(T_0 + T_m)$ and $G_{Mod}.(T_0 + T_m, T_{orb})$ are defined by rewriting the left hand side of eq.(66) and also right hand side of eq.(66) by expressing T_{orb} explicitly, as

$$G_{EHT}(T_m) = \frac{|D(2\pi/T_m)|}{|D_n(2\pi/T_m)|}. \qquad (73)$$

and
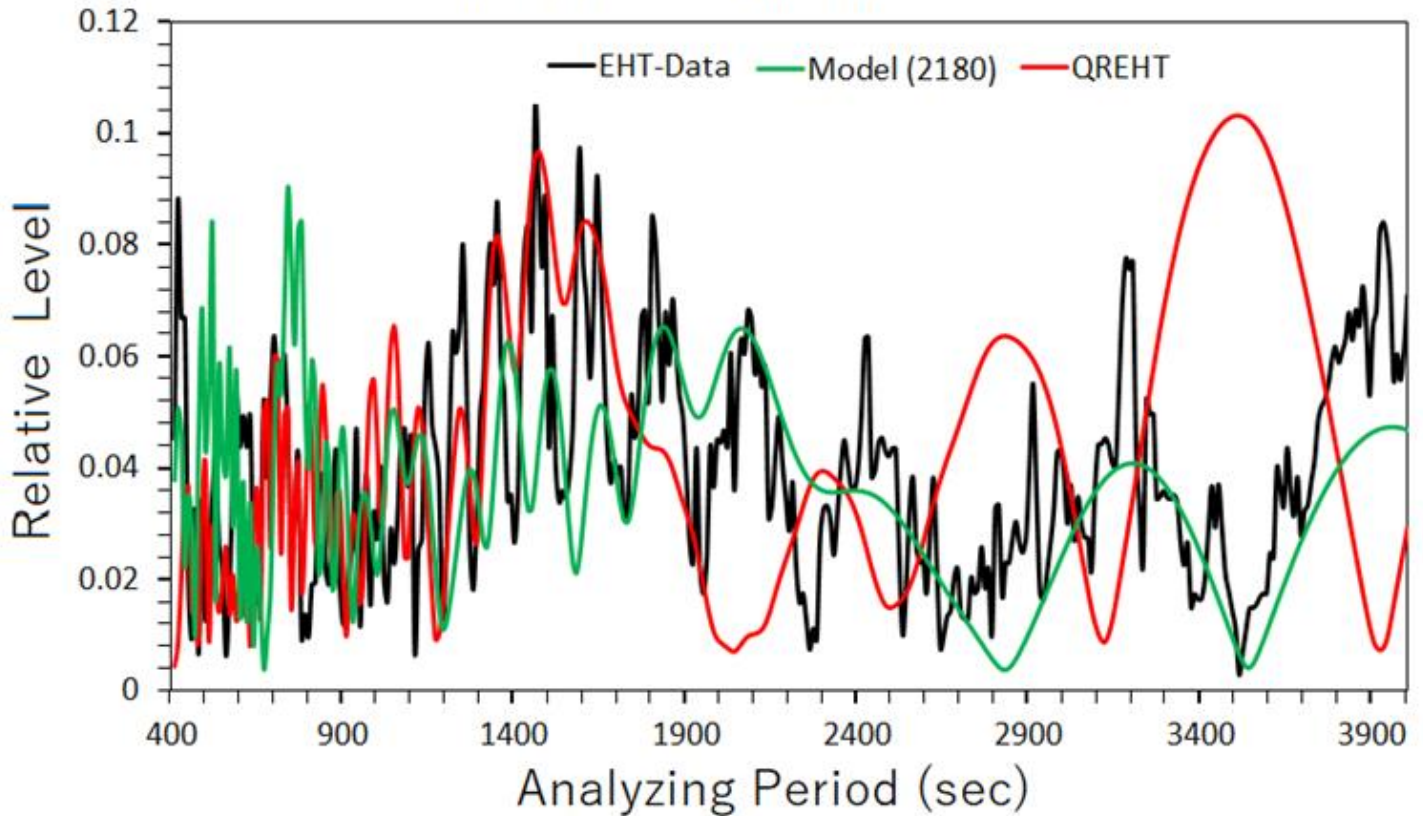
Figure 17. Same with Figure 13, for Day 97 Hi-HOPS AZ-SP baseline data. Reflecting the evidence of the longest baseline length of 8.48 Gλ (in average), the spectra structure of observed EHT-Data show several identical components, corresponding to spectra structure of the DRWP-Model, selected for the case of the orbiting period of 2180sec, even spectra are results of convolution with spectrum of the DSTW.

$$G_{Mod}(T_m, T_{orb}) = \frac{|Mod(2\pi/T_m, T_{orb})|}{|D_n(2\pi/T_m)|} \qquad (74)$$

For calculation of the SeInd index to estimate the coincidence of MDFT for EHT-Data and MDFT for DRWP-Model, we are allowed to select the range of T_m in a range where the modulation effect of the orbital motion of the SMBHB is clearly, dominant and sensitive under the condition of existing background noises which are generated with spectra of various time variations in the turbulent plasma co-existing with the spectra of the modulation with period of SMBHB orbital motion in SgrA*. In eq.(72), then, T_0 indicates the starting point of the calculation of the coincidence index, SeInd in term of the analyzing period .

In Figure 15, the selection index SeInd to evaluate the coincidence of MDFTs for EHT-Data and for DRWP-Model is indicated with respect to the orbiting period of SMBHB taking noise reduction coefficient α_D (see eq.(66)) as parameter by adjusting coefficient α_M=0.49 (see eq.(66)) to equalize the amplitude of DRWP-Model to the
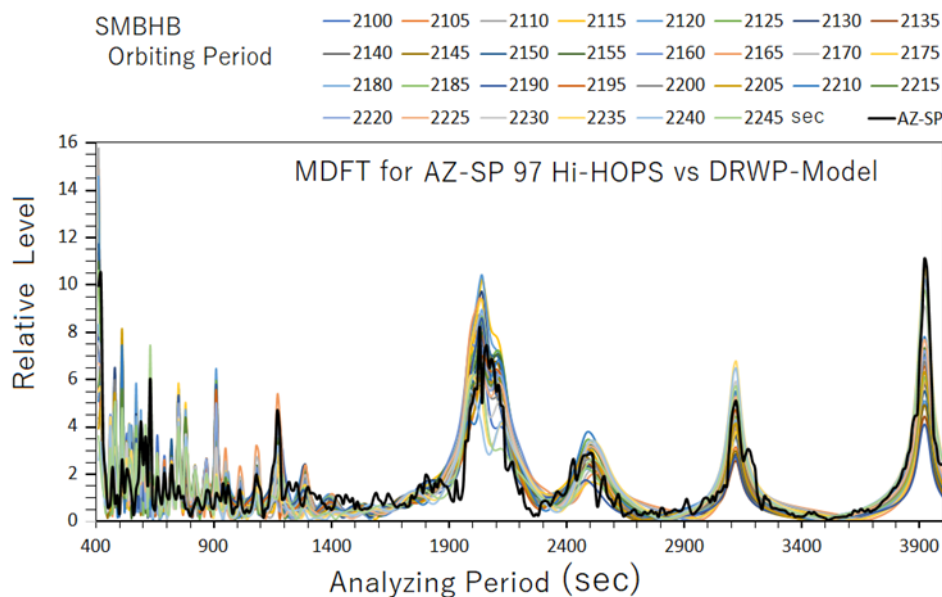
Figure 18. Same with Figure 14, for comparison of MDFTs for EHT-Data, Day 97 Hi-HOPS AZ-SP baseline (black thick curb) and for the DRWP-Model with 30 orbiting periods of SMBHB (given by corresponding colors).

level of EHT-Data after reduction of included noises. The results show that the best fit point between MDFTs for EHT-Data and for DRWP-Model occurs at the orbiting period of 2190 sec, in this case. Based on this evaluations we confirm FCED by confirming the coincidence of two MDFTs in Figure 16, where final results show the coincidence of the MDFT for EHT- Data (black curve) and the MDFT for DRWP-Model (green curve). Thus, it can be concluded that the EHT-Data have definitely the component of the VSCAT (Variation with short characteristic time) of steady time variation coinciding with an SMBHB orbiting period of 2190 sec prepared in DRWP-Model; it should be remarked

that the eclipse effect is associated SMBHB orbital motions adding VSCAT with the half of the orbital period of 1095sec.

7.3 The case of Day 97 Hi-HOPS AZ-SP baseline data

In Figure 17, results of three direct Fourier transformations for EHT data in the case of Day 97 Hi-HOPS AZ-SP baseline observation ,for corresponding QRN-EHT, and corresponding DRWP-Model selected for the orbiting period 2180 sec are indicated. Reflecting the evidence of one of the longest baseline length of 8.48 Gλ(average), the
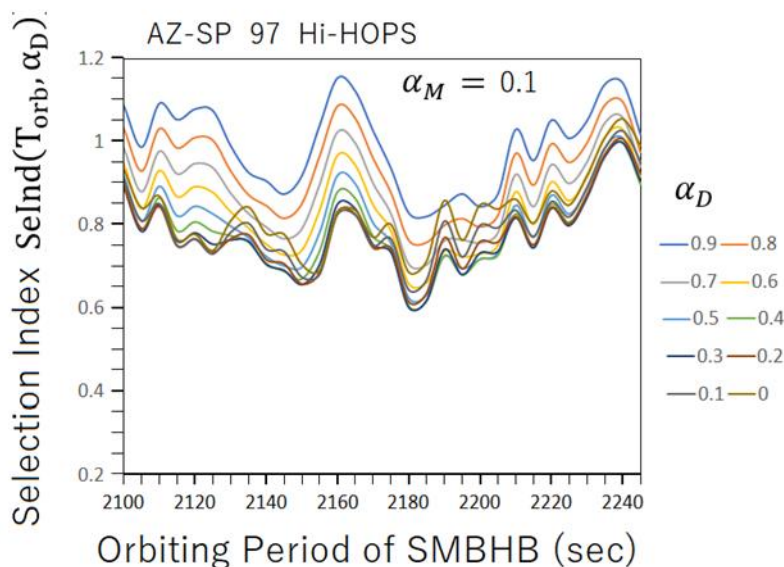

Figure 19. Same with Figure 15 for the selection index SeInd to evaluate the coincidence of MDFT for EHT-Data and MDFT for DRWP-Model with respect to the case of EHT-Data, Day 97 Hi-HOPS AZ-SP baseline. The results indicate that the best fit condition (the minimum of SeInd) between EHT-Data and DRWP-Model occurs at SMBHB orbiting period of 2180 sec.

structure of spectra of observed EHT-Data becomes complicated showing several peaks even under the control of the DSTW. Though the spectrum is convolution with the spectrum of DSTW that is close to QRN-EHT spectra given by the red curve, there are more than 8 peaks in the spectrum of EHT-Data which are almost identical with the DSTW affected spectrum of the DRWP-Model that is selected for the case of the orbiting period of 2180sec.

As the case of Day 96 Hi-CASA SM-SP baseline data, we apply the method to calculate MDFT using DSTW spectrum S(ω) to confirm FCED. In Figure 18, the calculated MDFTs for EHT Data $|D(\omega)|/|S(\omega)|$ and for the DRWP Model $|Mod(\omega)|$ / $|S(\omega)|$ with corresponding 30 cases of the orbiting periods of SMBHB, are indicated with respect to the analyzing period from 400 sec to 4000 sec for the case of Day 97 Hi HOPS AZ SP; we can see that plots of MDFT for the DRWP Model with parameters of corresponding SMBHB orbiting periods are distributed around the MDFT of EHT Data with systematic features from which we are able to find the best fitting case. For the selection of the best fit case, then, we have calculated the selection index SeInd given by eq.(72); the results are given in Figure 19 where the selection index SeInd is indicated as the function of the orbiting period of SMBHB taking noise
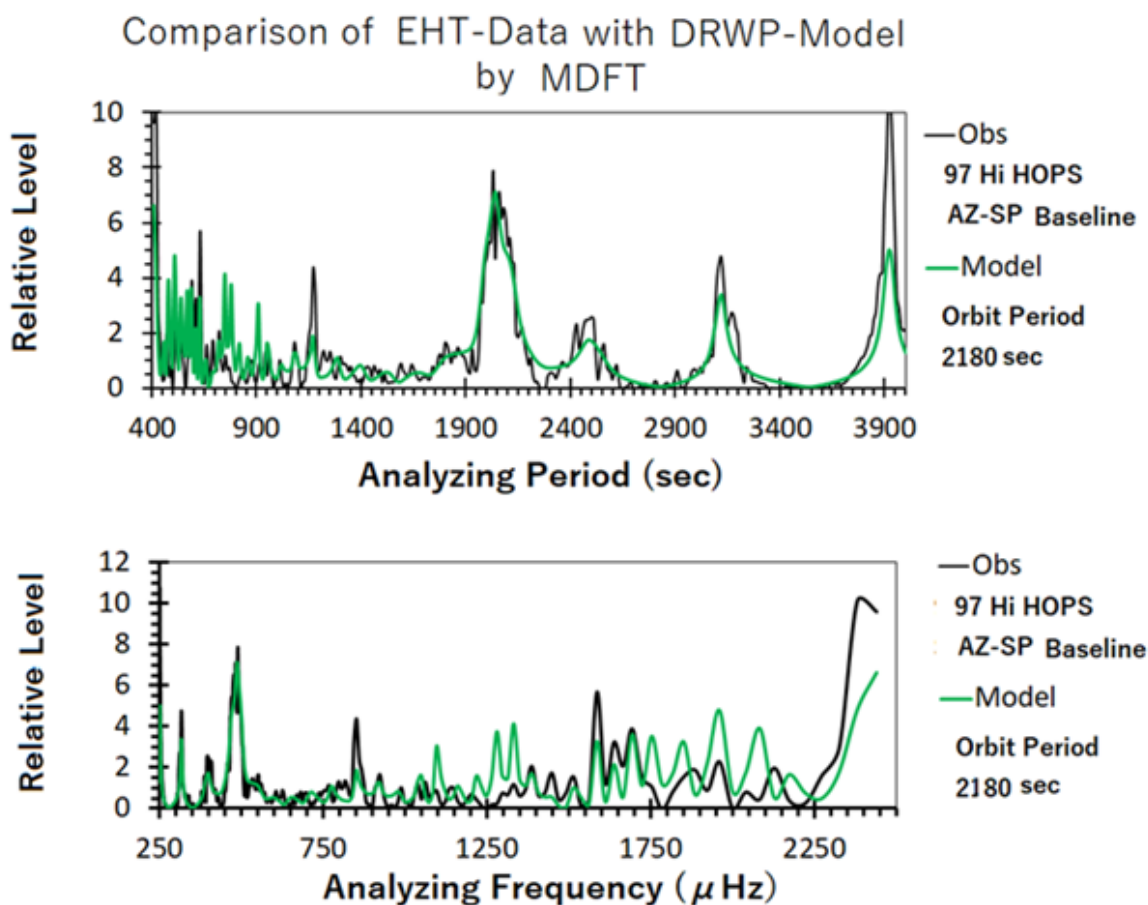
Figure 20. Same with Figure 16 to show concluding results for the coincidence of the MDFT for EHT Data (black curve) Day 97 Hi HOPS AZ SP baseline with MDFT for DRWP Model (green curve) at the SMBHB orbiting period of 2180 sec.

reduction coefficient α_D (see eq.(66)) as parameter by adjusting coefficient as α_M=0.1 (see eq.(66)) that is decided to make the level of EHT-Data equal to the amplitude of DRWP-Model. The results show that the best fitting point of MDFTs for EHT-Data and for DRWP-Model occurs at the orbiting period of 2180 sec, in this case, with the noise reduction coefficient α_D=0.3. Based on this evaluation we can confirm the coincidence of two MDFTs in Figure 20 where we can see finally selected results that show the coincidence of the MDFTs for EHT-Data (black curve) and MDFT for DRWP-Model (green curve). We can conclude that the EHT-Data have also the component of steady time vari-

ation coinciding with the SMBHB orbiting motions with period of 2180 sec.

**7.4 The Cases of Medium Baseline Length**
As the cases of medium baseline length of the EHT-Data, we have selected the cases Day 97 Hi-CASA LM-SM baseline data and Day96 Hi-HOPS AZ-SM baseline data; in Figure 21, the results of three direct Fourier transformation in the case of LM-SM baseline (in panel (A)) and those in the case of the AZ-SM baseline (in panel (B)) are
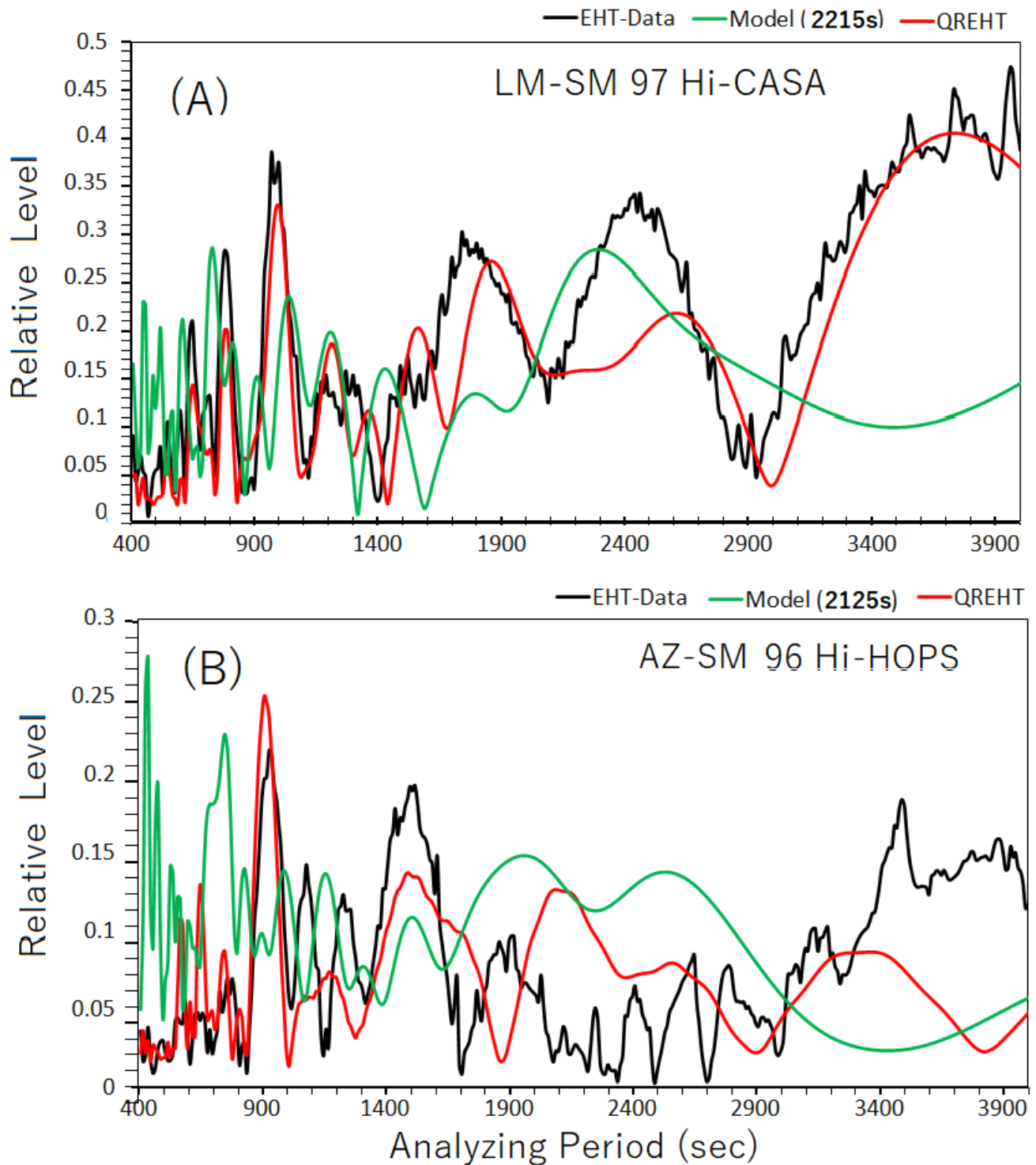
Figure 21. Same with Figure 13, for two cases of EHT-Data Day 97 Hi-CASA LM-SM baseline (Panel A) and Day 96 Hi-HOPS AZ-SM baseline (Panel B). The features of three direct Fourier transformation in the case of LM-SM are reflecting the characteristics of medium baseline length visibilities around 3 to 4 Gλ where the spectrum of EHT-Data shows co-existence with white noise component coinciding with tendency of QRN-EHT spectrum in several analyzing period ranges. The spectrum of EHT-Data of AZ-SM shows same characteristics with the case of LM-SM; however, there is unusual feature where the spectrum shows decreasing level in the period range from 2000 sec to 3000sec departing from DSTW (red curve).
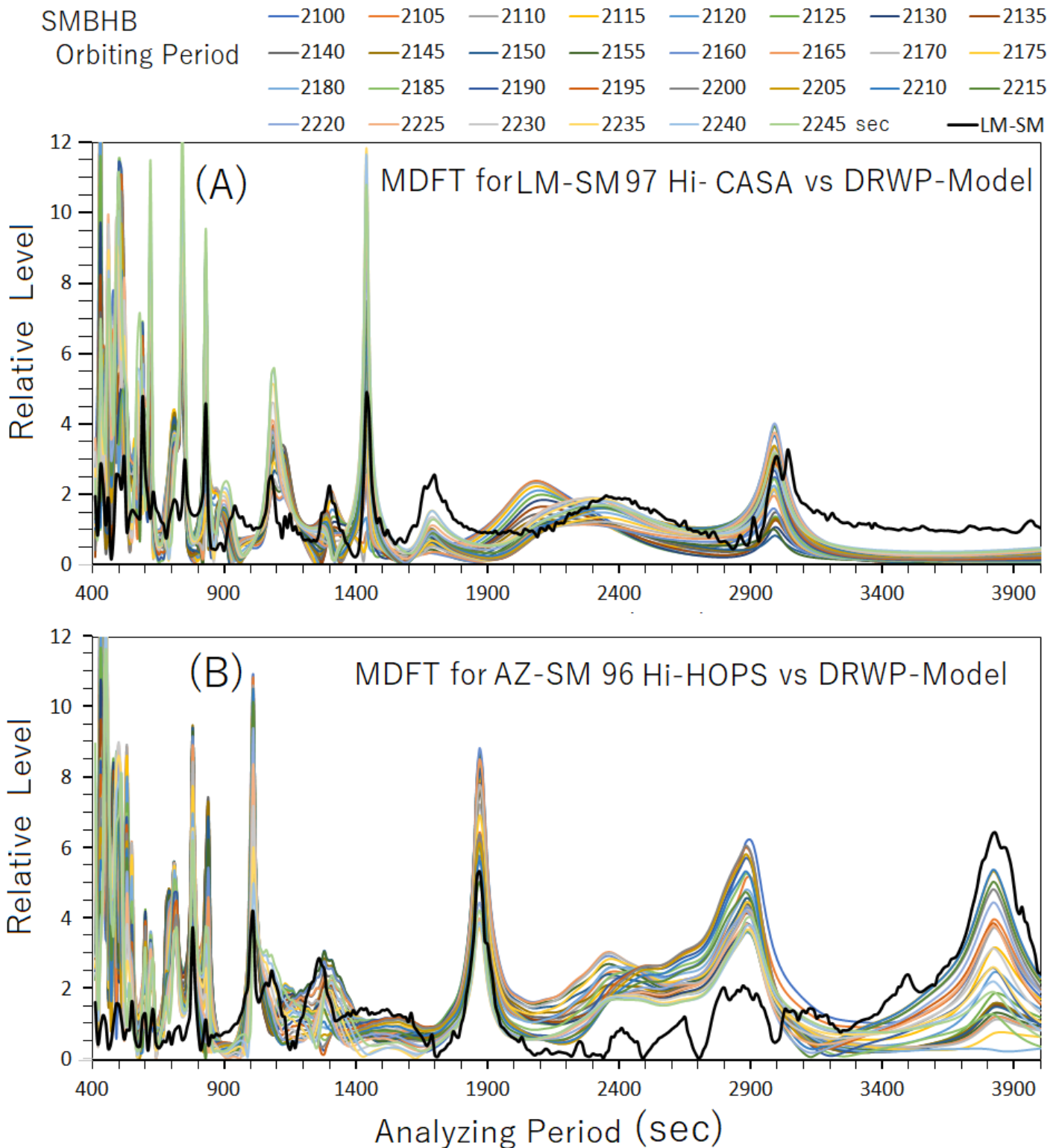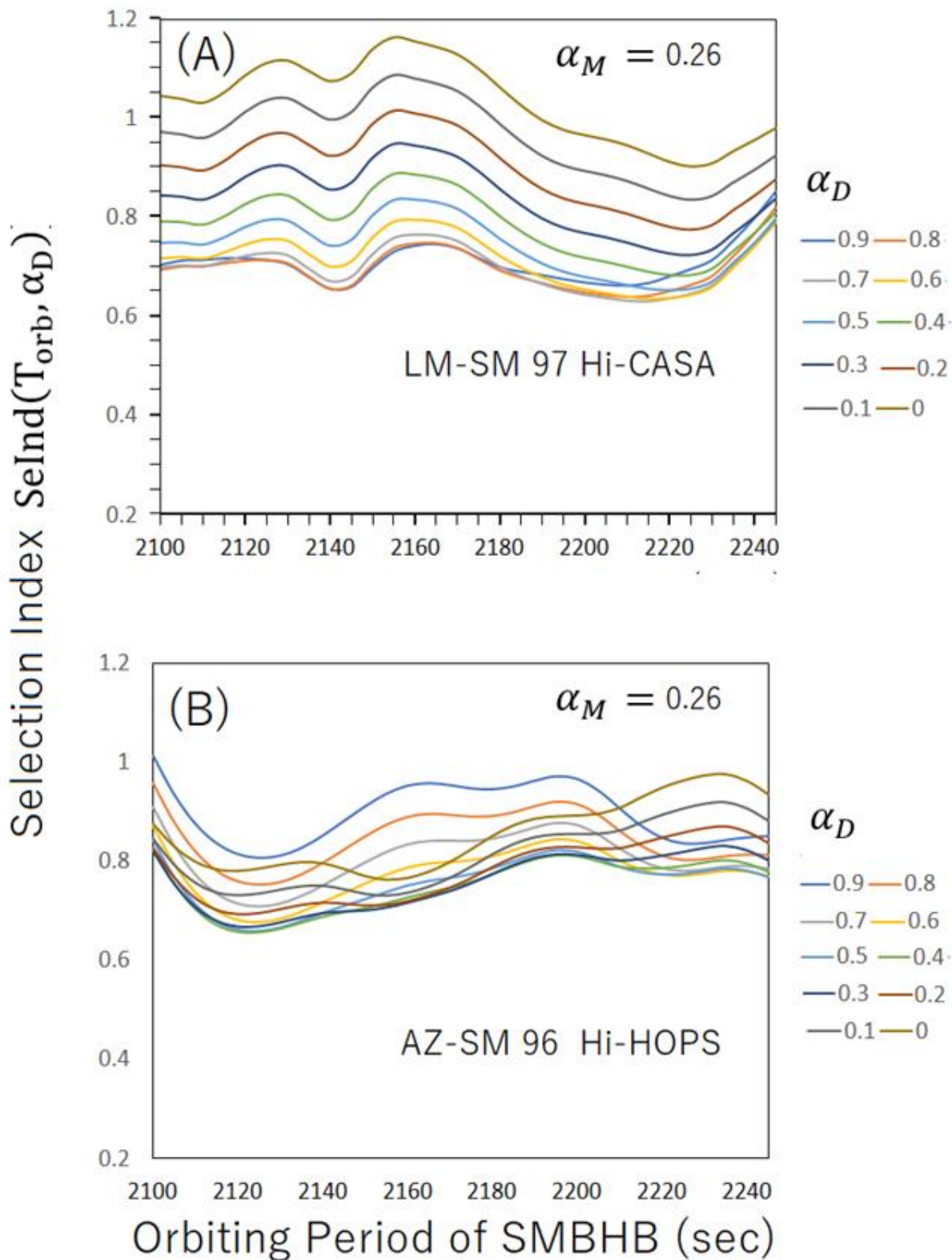
Figure 22 Same with Figure 14, for comparison of MDFT for EHT-Data Day 97 Hi-CASA LM-SM baseline (Panel A) and Day 96 Hi-HOPS AZ-SM baseline (Panel B). In each panel MDFT for EHT-Data (black thick curb) and MDFT for DRWP-Model with 30 orbiting periods of SMBHB (given by corresponding colors) are plotted versus the analyzing period from 400sec to 4000sec.

indicated. The features of combinations of displayed three Fourier transformation results are reflecting the characteristics of medium baseline length visibilities around 3 to 4 Gλ where the spectrum of EHT-Data shows features of co-existence with

Figure 23. Selection index SeInd to evaluate the coincidence of MDFT for EHT-Data and MDFT for DRWP-Model same as Figure 15. SeInds are calculated versus the orbiting period of SMBHB for the EHT-Data Day 97 Hi-CASA LM-SM baseline (Panel A) and Day 96 Hi-HOPS AZ-SM baseline (Panel B) taking noise reduction coefficient α_D as parameter with adjusting coefficient α_M (=0.29) that is set to make the level of EHT-Data equal to the amplitude of DRWP-Model. The results show that the best fit point of MDFTs for EHT-Data and DRWP-Model is revealed for the case of orbiting period of 2210 sec with noise reduction rate α_D=0.6 for LM-SM baseline and the orbiting period of 2125 sec with noise reduction rate α_D=0.4 for AZ-SM baseline.
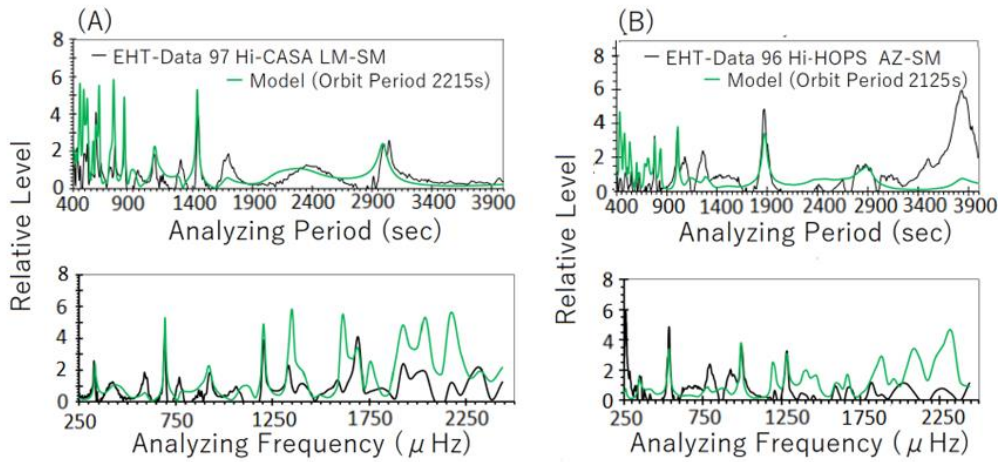
Figure 24. Final results showing coincidence of the MDFT for EHT-Data (black curve) and the MDFT for DRWP-Model (green curve) for two cases of the medium range baseline length observations of EHT-Data Day 97 Hi-CASA LM-SM (Panel A) and Day 96 Hi-HOPS AZ-SM (Panel B) . In the case of LM-SM baseline observation, it can be concluded that the EHT-Data have definitely the component of steady time variation coinciding with the SMBHB orbiting period of 2215 sec. In the case of AZ-SM baseline observation, however, the evaluation of coincidence becomes critical though there are sufficient identical ranges of analyzing periods for MDFTs for EHT-Data and DRWP-Model.

increased rate of white noise components. That is, there appear the tendency of the similarity between trends of MDFTs of EHT-Data and spectrum of QRN-EHT in several analyzing period ranges. Though the spectrum of EHT-Data of AZ-SM given in panel (B) shows same characteristics with the case of LM-SM, there is one unusual feature in the period range from about 2000 sec to 2500 sec of the analyzing period which could be attributable to some unknown unnatural cause which resulted forced depressing of the EHT-Data.

In Figure 22, the MDFT, $|(D(\omega)|\,/\,|(S(\omega)|$ for the EHT-Data of Day 97 Hi-CASA LM-SM baseline and the MDFT for the DRWP-Model $|Mod(\omega)|/|S(\omega)|$ with corresponding 30 cases of the orbiting periods of SMBHB , are indicated in panel (A); and the case of Day 96 Hi-HOPS AZ-SM baseline is given in Panel

(B). In each panel, the MDFT for EHT-Data is indicated as function of the analyzing period from 400sec to 4000sec with black thick curb, meanwhile MDFTs, for DRWP-Model with parameters of 30 orbiting periods of SMBHB given by corresponding colors are plotted as function of the analyzing period from 400sec to 4000sec. In the displayed diagram in the panel (A), we can see that plots of the MDFT for DRWP-Model indicating clear dependence on orbiting periods are distributed around the EHT-Data suggesting the possibility to select best fitting case of the SMBHB orbiting period in the analyzing period range below 3000 sec. In the case of panel (B) with respect to the AZ-SM baseline, apparent depression of the MDFT for EHT-Data is disclosed in the analyzing period between 2000 sec and 3000sec as predicted before calculating MDFT at the stage of DSTW
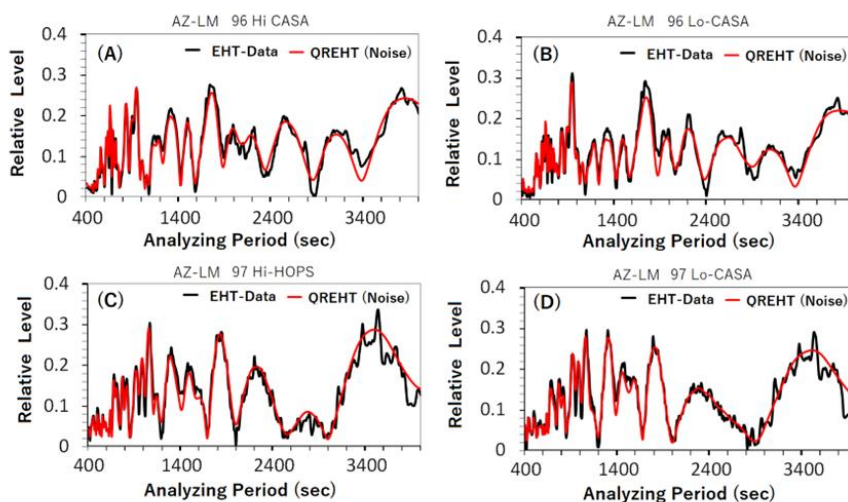
Figure 25. Results of Fourier transformations under the effects of DSTW of EHT-Data for baseline AZ-ML observation compared with averaging Fourier transformations for 10 sets of QRN-EHT. The EHT-Data are selected from 4 cases as Day 96 Hi-CASA (Panel A), Day 96 Lo-CASA, (Panel B) , Day 97 Hi-HOPS (Panel C) and Day 97 Lo-CASA (Panel D). Results are displayed versus the analyzing period $2\pi/\omega$ from 400sec to 4000 sec ; in all cases, there are good coincidences between Fourier transformed EHT-Data, $D(\omega)$ and Fourier transformed QRN-EHT, $S(\omega)$ suggesting that MDFT for EHT-Data constantly becomes the unity in the whole analyzing range except for fractionally small deviations.

controlled Fourier transformation given in Figure 21. Then, we have avoided this analyzing period range between 2000 sec and 3000sec for calculation of SeInd. In Figure 23, the selection index, SeInd to evaluate the coincidence of MDFT for EHT-Data and MDFT for DRWP-Model are indicated with respect to the orbiting period of SMBHB for the cases of EHT-Data ,Day 97 Hi-CASA LM-SM baseline in Panel (A) , and the case of Day 96 Hi-HOPS AZ-SM baseline, in Panel (B), taking noise reduction coefficient α_D as parameter after taking level adjust coefficient as α_M=0.29 both for the LM-SM and AZ-SM baseline data. The results show that the best fit point of MDFTs for EHT-Data and for DRWP-Model occurs at the orbiting period of 2210 sec for the case of noise reduction rate α_D=0.6 for LM-SM baseline and the orbiting period of 2125 sec taking noise reduction rate as α_D=0.4 for AZ-SM baseline. For the results of FCED of the medium range baseline length observations of EHT-Data, it is noted that the noise reduction coefficients are in the range 0.4 ~ 0.6 which are apparently larger than the case of long baseline length observations where the noise reduction coefficients (see Appendix D for details) are in the range 0.1 ~ 0.3.

After determination of the orbiting periods, the final confirmation of comparison of MDFTs for EHT-Data and DRWP-Model are made as given in Figure 24 where final results are displayed for two cases of the medium range baseline length observations of EHT-Data corresponding to Day 97 Hi-CASA LM-SM in Panel (A) and corresponding to Day 96 Hi-HOPS in Panel (B) showing coincidence of the MDFT for EHT-Data (black curve) and the MDFT for DRWP-Model (green curve). In the case of LM-SM baseline observation, it can be concluded that the EHT-Data have definitely the component of steady time vari-

ation coinciding with the SMBHB orbiting period of 2215 sec expressed by the coincidence of two MDFTs for EHT-Data and DRWP-Model.

In the case of AZ-SM baseline observation, the evaluation of coincidence becomes critical though there are sufficient identical analyzing period range of MDFTs for EHT-Data. It is clarified that estimated inclusion of the random noise component is increased by about 1.6 times for the case of AZ-SM data compared with the case of LM-SM.

7.5 The case of Short Baseline Length

In Figure 25, results of Fourier transformations under the effects of the DSTW of the EHT-Data for baseline AZ-ML, are displayed as cases of the short baseline length observation, compared with averaged spectra of QRN-EHT by selecting 4 cases as Day 96 Hi-CASA ,in Panel (A), and Day 96 Lo-CASA, in Panel (B); and Day 97 Hi-HOPS in Panel (C), and Day 97 Lo-CASA ,in Panel (D) . Results are displayed with respect to the analyzing period $2\pi/\omega$,from 400sec to 4000 sec; in all cases, clear coincidences arise between the Fourier transformed EHT-Data D(ω) and Fourier transformed QRN-EHT, S(ω) suggesting that the MDFT for the EHT-Data show constantly the unity ($|D(\omega)|/|S(\omega)| \approx 1$) in the whole analyzing range except for fractionally small deviations.

By complete identification of the EHT-Data and QRN-EHT which result the constant, MDFT value of unity for the EHT-Data, it is indicated that no apparent room is left for coincidence between the MDFTs for DRWP-Model which reveal

Table 3 Total List of Analyzed SMBHB Orbiting Period

Baseline	Day	Frequency	Pipeline	Period (sec)	α_D	α_M	Min SeInd
AZ-SP	"96"	Hi	CASA	2185	0	1.26	0.48
		Hi	HOPS	2220	0	0.72	0.459
		Lo	CASA	2235	0	0.6	0.411
		Lo	HOPS	2240	0.3	0.6	0.506
	"97"	Hi	CASA	2200	0.2	0.48	0.51
		Hi	HOPS	2180	0.4	0.33	0.605
		Lo	CASA	2220	0.3	0.4	0.417
		Lo	HOPS	2225	0	0.48	0.611
	Average				0.14	0.6	
SM-SP	"96"	Hi	CASA	2190	0	0.7	0.274
		Hi	HOPS	2140	0.2	0.56	0.613
		Lo	CASA	2215	0.4	0.48	0.664
		Lo	HOPS	2140	0.4	0.24	0.624
	"97"	Hi	CASA	2190	0	0.5	0.462
		Hi	HOPS	2170	0	0.6	0.382
		Lo	CASA	2195	0.1	0.2	0.67
		Lo	HOPS	2190	0.5	0.36	0.374
	Average				0.2	0.45	
LM-SM	"96"	Hi	CASA	2175	0	0.39	0.465
		Hi	HOPS	2150	0.1	0.2	0.696
		Lo	CASA	2195	0.3	0.24	0.514
		Lo	HOPS	2175	0	0.26	0.63
	"97"	Hi	CASA	2235	0.7	0.48	0.575
		Hi	HOPS	2195	0.5	0.36	0.423
		Lo	CASA	2205	0.2	0.24	0.506
		Lo	HOPS	2175	0.3	0.32	0.429
	Average				0.26	0.31	
Average				2193.3			
STD				27.5			

variations of level corresponding to given orbital period of SMBHB. We can understand this evidence as that the EHT-Data AZ-ML with baseline length of 1.18 Gλ (average) are out of limits for detecting the orbit of the existing SMBHB.

7.6. Final Decision of Orbiting Period of the SMBHB

In Table 3, the total list of SMBHB orbiting periods as analyzed by the MDFT methods which are described in Sec.6 for the principle, and Sub. Secs 7.1~ 7.5 for actual application as example cases are further listed by expanding the number of examples to 24 cases, to determine the proper SMBHB orbiting period. We list also the SeInd, α_D and α_M ,in Table 3, for the cases of the best fit between MDFTs for EHT-Data and for DRWP-Model which are evaluated as minimum of the SeInd; that is, the indices show minimum difference of the MDFTs for EHT-Data and for DRWP-Model. The examples of the analyzed data are selected from the data with baselines AZ-SP, SM-SP and LM-SM where the baseline lengths are longer than 4Gλ considering the sufficient signal (modulation by the existing SMBHB) to noise (emissions independent to SMBHB motion) ratio based on the estimation given by eq.(27) and evidences of example cases given Sub. Secs. 7.1 ~ 7.5. To show reasoning that the variation of the deduced orbiting periods is not attributable to the real variability of the proper orbiting period of SMBHB, but to the numerical fluctuation due to the noise disturbance in analyzing data, we have selected all eight possible data for each of the three selected baselines ; that is, we are given data from observations on two days, Day 96 and 97 at the two center frequencies , Hi and Lo ; and all these 4 data are calibrated and made correlation by two data handling pipelines CASA and HOPS, ,as expressed in the Table 3.

All 24 data are analyzed by MDFT (Modified Fourier transformation) methods following the procedures that are described in Sub Secs. 7.2 ~ 7.4, in detail. The selection of the orbiting period given in DRWP-Model as 30 parameters from 2100 sec to 2245 sec, has been made utilizing the defined SeInd as has been given in eq.(72). To form eq. (72), we search for two constants α_D and α_M as has been explained relating to eq.(66). With respect to α_M, significance is only limited for the numerical adjustment between two independently generated quantities; however, α_D has physical significance because the coefficient is tightly connected to the signal to noise ratio as details are explained in Appendix D. It is clarified that as given in Table 3, average α_D values of the results of AZ-SP , SM-SP and LM-SM baselines are 0.14, 0.2 and 0.26 respectively. By looking up the Table 4 (see Appendix D), then, we understand that the ratio of $\overline{P_s(\omega) * S(\omega)}$ to $N_L\overline{S(\omega)}$, i.e., representing the signal to noise ratio , are 3.5, 2.3 and 1.8 respectively for AZ-SP , SM-SP and LM-SM baseline data.

About results of the decided orbiting period of SMBHB by analyses in Sub. Secs. 7.2 ~ 7.5 for which the results are also listed in the Table 3, it is apparent that the differences in the obtained orbiting periods are caused by independently coexisting noises in each corresponding datum because the analyzed orbiting periods are resulted by the observations made at the same time and using same devices when we analyze the data of the same baseline of VLBI. To decide a stable proper orbiting period of the SMBHB, therefore, we are allowed to average the analyzed orbiting periods listed in Table 3. Thus, the result gives a period of 2193.3 sec with the standard deviation of 27.5 sec as the proper orbiting period of the existing SMBHB.

Table 4 α_D versus $\overline{P_s(\omega) * S(\omega)}$ and $N_L\overline{S(\omega)}$

$N_L\overline{S(\omega)}$	$\overline{P_s(\omega) * S(\omega)}$
	0.1	0.2	0.3	0.4	0.5	0.6	0.7	0.8	0.9	1
0.1	0.414	0.236	0.162	0.123	0.099	0.082	0.071	0.062	0.055	0.049
0.2	0.618	0.414	0.302	0.236	0.192	0.162	0.14	0.123	0.109	0.099
0.3	0.72	0.535	0.414	0.333	0.276	0.236	0.205	0.181	0.162	0.146
0.4	0.78	0.618	0.499	0.414	0.35	0.302	0.265	0.236	0.212	0.192
0.5	0.819	0.677	0.566	0.48	0.414	0.362	0.32	0.286	0.259	0.236
0.6	0.847	0.72	0.618	0.535	0.468	0.414	0.369	0.333	0.302	0.276
0.7	0.867	0.754	0.659	0.58	0.514	0.459	0.414	0.375	0.343	0.315
0.8	0.882	0.78	0.693	0.618	0.554	0.499	0.453	0.414	0.38	0.35
0.9	0.895	0.802	0.72	0.649	0.588	0.535	0.489	0.449	0.414	0.383
1	0.904	0.819	0.744	0.677	0.618	0.566	0.52	0.48	0.445	0.414

8. Discussion
8.1 Correctness of MDFT Method

As has been told about DSTW (Data Sampling Time Window) in Sec.6, the EHT-Data are characterized by unique data sampling timing with pauses that repeat in interval around 1000 sec to 1100sec (see Figure 4, for examples). Apparently this interval or DSTW itself contains its own information which appears as the convolution of spectra of DSTW together with the proper spectra for the physical phenomena. Hence, we are unable to find the proper spectra for the physical phenomena from simple Fourier transformation of the observed data. To assess this problem, in the present work, we employ random noises whose appearance is synchronized with DSTW that is called QRN-EHT (Quasi Random noise synchronized with EHT data

sampling time window) to produce the spectra S(ω) of DSTW as it has been described in Sec.6 also.

To use S(ω) (equivalent to average of the noise spectra $D_n(\omega)$) to separate the proper spectra $P_s(\omega)$ of the physical phenomena from the direct Fourier transformation D(ω) of the DSTW affected EHT -Data, we do not apply the deconvolution processes but instead use the method of the MDFTs (Modified Fourier transformation) which are expressed by eqs. (62) and (64), respectively as $|D(\omega)| / |S(\omega)|$ for the DSTW affected EHT-Data and $|Mod(\omega)| / |S(\omega)|$ for the DSTW affected DRWP-Model. Therefore, if there is no noise, to obtain the relation given by eq.(66) , in Sec.6, means that

$$\frac{|P_s(\omega) * S(\omega)|}{|D_n(\omega)|} = \alpha_M \frac{|Mod_p(\omega) * S(\omega)|}{|D_n(\omega)|} . \qquad (75)$$

where $Mod_p(\omega)$ is the proper spectra of DRWP-Model (see eq.(64) and Figure 11) .

In real cases, the EHT-Data contain almost equivalent level of noises modulated by the same DSTW then we are trying to approach the concept of this expression eq.(75) by adjusting α_D, in eq.(66) which are shown in Figures 15, 19, and 23. The point of discussion is whether we are able to conclude that $P_s(\omega)=\alpha_M Mod_p(\omega)$ or not by this procedure. When two results

of MDFT coincide for all discussing ω, no room is left to negate the coincidence $P_s(\omega)=\alpha_M Mod_p(\omega)$. The problem occurs when two MDFTs coincide partially, e.g.by 80% for an example. One of point to evaluate the coincidence of two MDFTs is to investigate the coincidence of remarkable peaks for occurring frequencies or periods. In this context, the MDFT has serious characteristic that the peaks are formed commonly both in MDFT for EHT- Data and that for DRWP-

Table 5 Effect of $1/D_n(\omega)$ for Evaluation of Coincidence

Baseline	Dn Dip	MDFT Peak	No Coincidence
SM-SP	11 (Figure 11)	17 (Figure 13)	2
AZ-SP	19 (Figure 17)	28 (Figure 20)	3
LM-SM	12 (Figure 21)	16 (Figure 24)	3
AZ-SM	11 (Figure 21)	12 (Figure 24)	3

Model at ω where $D_n(\omega)$ takes minimum. Therefore we are required to investigate the coincidence between two peaks of spectra of the MDFTs by confirming the existence of ω coresponding to coincidences of peeks which are independent to the dip of $D_n(\omega)$. For this context, we prepare Table 5 where relation of the existing numbers of dips in $D_n(\omega)$ and those in the resulted MDFTs for EHT-Data for the selected four cases of baselines. The results show that generally peaks in the spectra of MDFT are controlled
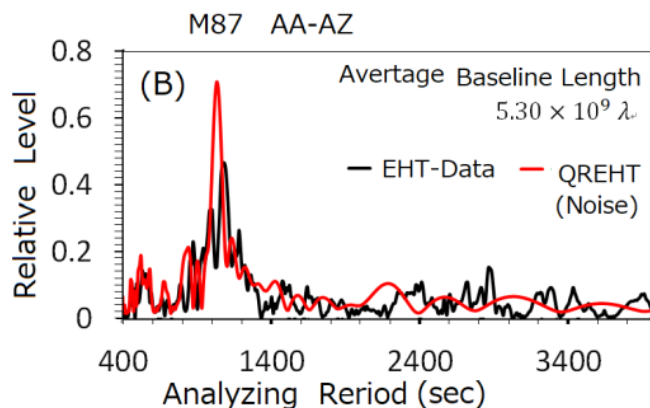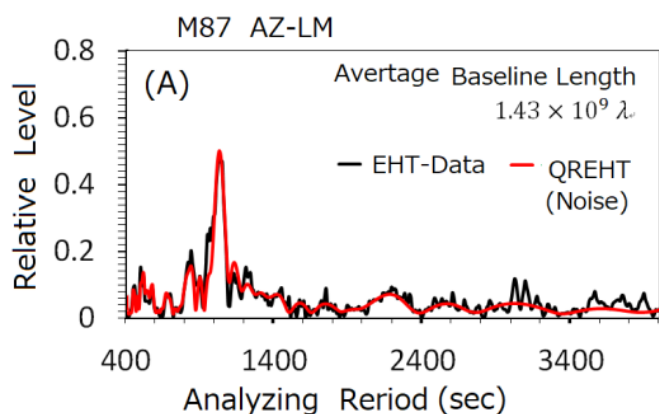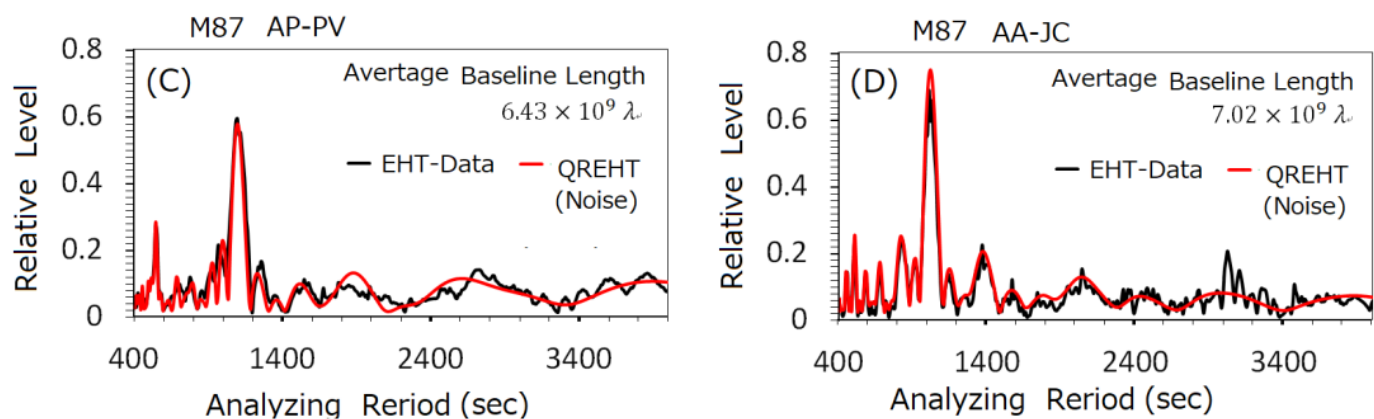
Figure 26. Comparison of Fourier transformed results (black data plots) of EHT-Data of M87* for observation of EHT campaign observation on April 6 in 2017 with the High frequency with data reduction pipeline, HOPS and Fourier transformed results (red data plots) for QRN-EHT (Quasi Random Noise sampled synchronized with DSTW of EHT-Data). In panels from (A), to (D), the cases for the baseline AZ-LM with the average baseline length (ABL) 1.43 G λ, for the baseline AA-AZ with ABL 5.30 G λ, for the baseline AP-PV with ABL 6.43 G λ and for the baseline AA-JC with ABL 7.02 G λ are displayed , respectively. In general, it is remarkable (with a few exception of minor spectra level) that the Fourier transformations for EHT data and for QRN-EHT coincide each other; that is, there are no VSCAT in M 87*.

by $D_n(\omega)$ as predicted; in the cases of long baseline around 8 G λ such the cases of SZ-SP and AZ-SP, however, coincidence of spectra which can attribute to the coincidence of the proper spectra are apparently indicated.

Based on above arguments then we realize that the role of MDFT to identify the EHT-Data and DRWP-Model is to provide the selection function by detecting the fitting parameter in the DRWP-Model to results the closest ω dependence of two MDFT functions rather than claim complete fitting of two proper spectra. In Figures 14, and 18, for the EHT-Data of SM-SP and AZ-SP respectively and in Figure 22 for two cases of EHT-Data of LM-SM and AZ-SM, we can see the effectiveness of MDFT for the DRWP-Model by providing role of the selection of orbiting periods of SMBHB that are given as parameters to form DRWP-Model which distributed around the MDFT of EHT-Data. In addition to the selection role of the searching orbiting period of SMBHB, - it has also important role that we can separate random noise component in the observed EHT-Data as indicated by eq. (66) in Sec.6.

8.2 Comparison with Time Variation of the EHT Observation Data for M87*

We are allowed to check, whether the method employed in the present study to analyze the VSCAT (Variation of Short Characteristic Time) in the data of SgrA* contains any self contradictory subjects or not because of the effect of the unique DSTW of EHT-Data by using the public released EHT-Data, for M87*, where the same DSTW (data sampling time window) was applied with the case of EHT-Data for SgrA*.

In Figure 26, we display the comparison of Fourier transformed results (black data plots) for the EHT-Data of M87* observed on April 6 in 2017 and Fourier transformed results (red data plots) for QRN-EHT (Quasi Random Noise sampled synchronized with DSTW of EHT-Data). As examples, we have selected EHT-Data from Hi-HOPS; in panels (A), (B), (C) and (D) in Figure 26, the cases for the baseline AZ-LM with the average

baseline length (ABL) 1.43 Gλ, the cases for the baseline AA-AZ with ABL 5.30 Gλ, the cases for the baseline AP-PV with ABL 6.43 Gλ and the cases for the baseline AA-JC with ABL 7.02 Gλ are displayed , respectively. In general it is remarkable (with a few exceptions associated with minor fractional deviations) that the Fourier transformations for EHT data and QRN-EHT coincide each other ; that is, remarkably there is no VSCAT in the data of EHT for M87*. For this context we find extreme difference with case of the SgrA* where the relation between the Fourier transformed results for EHT-Data and the Fourier transformation for the QRN-EHT change the feature dramatically with a baseline length threshold around 1~3 G λ. That is, in the case of the SgrA*, the component of the remarkable VSCATs appear independently to the DSTW as we can see in Figures 13, 17, 21, contrary to the case of short baseline length as given by Figure 25.

By analyzing the EHT observation data for M87*, we conclude that there is no remarkable spectra to consider any periodicity as effect of SMBHB. However, it is clarified that time variation spectra associated with M87* are generated with the DSTW due to the EHT observation procedure. The most apparent point of DSTW control is revealed as the pervading peaks around 1000~1100sec of the analyzing period of spectra which are confirmed as DSTW effects by the occurrence both for the EHT-Data and QRN-EHT simultaneously. Through entire portions of the present work, we have pointed out that EHT-Data are artificially modified by observation pauses which are repeated with period about 1000sec ~ 1100 sec. It is clearly disclosed that EHT-Data are largely altered from the prospect to search for the time variation of the radio emissions including the modulation of the orbiting SMBHB. Especially, the eclipse effects of the SMBHB that occur with the period 1098±14 sec are largely affected.

8.3 Relation to the Confirmation by Foregoing Work[17]
In this work, we have focused on the orbital motion of SMBHB concluded by DRWP study as a binary system, with an orbital period of 2200±50 sec (see review in Sub Sec.2.1 for other pa-

rameters). Regarding the possibility of a fast period around 2200 sec, we had reported confirmation in foregoing work where we interpreted the publish data by Fish et al [5]for the observations by the VLBI at wavelength 1.3mm. The main differences between foregoing work[17] and the present work for EHT-Data, are in two points. The first of the difference is in the utilized data of the foregoing work where only the absolute value of the visibility of the interferometer was concerned; therefore the DRWP-Model for comparison had no phase component. The second of the difference is baseline length of the observed data that were observed between California and Arizona, USA with average length becomes 0.60 Gλ. Because we utilized only selected data points of extremely large and high S/N ratio, we were able to identify the existence of SMBH at the SgrA,* only by coincidence of time varying power of VSCAT even with the baseline of the short length category. The result of the foregoing work then indicated the confirmation of the DRWP-Model with orbiting period of the possible SMBHB to be 2150±2.5 sec. The result of present work which give confirmation to the orbiting period of possible SMBHB to be 2193.3±27.5 sec, based on EHT-Data, is fairly closer to originally proposed period 2200sec ; furthermore the present result gives confirmation to orbit size and geometry of the orbital plane.

8.4 Constraining to Gravitational Wave Generation

It had already been discussed in the foregoing work[17], (given in Sub. Sec. 8.3) that the existence of the extreme SMBHB could be contradictory if we apply the current concept of the generation of gravitational waves from binaries of compact celestial objects such as neutron stars and star mass BHs. That is, due to radiation of the intense gravitational wave energy, it is impossible to exist such an extreme SMBHB described in the present work. If we apply the Landau Lifshitz equation [37] to the distance variation of the binary with parameters that we present (see Sub Sec 2.1 and Figure 1), the two bodies merge within 8 hours.

About this subject, we had published a paper in early 2023 [9] where we showed the theoretical model confirmed no gravitational waves from the orbiting SMBHB; the content are summarize below. The matter distribution of SMBHs becomes extremely tenuous compared with the cases of the star mass BHs, because the averaged matter density follows the inverse square law with respect to the BH mass. Though the energy of matter increases to extremely high level cocentrated inside regions of BH. About the inside matter of a supermassive rotating BH, we have described the dynamics via classical plasma physics (because matter density is not extremely high). That is, by selecting a coordinate close to the free-falling frame along the geodesics with respect to the interior matter of BH, we can identify the force balance state described with the formalism of modified Newtonian dynamics resulted via the Einstein's equation with the source term. Then, for a model of uniformly rotating matter where the main component of plasma rotates about a common axis with the same velocity close to the light velocity with a high Lorentz factor (gamma rate), it is concluded that the matter distribution is condensed to a region with a radius much smaller than that of the event horizon of the Kerr space time. The gravitational waves that are generated via the orbital motion of the SMBHB, from the condensed matter cease the propagation at the critical sphere in the vacuum region inside of the event hori-

zon of spinning Kerr space time. The ceased gravitational waves return back towards the source and encounter with forwarding waves. At the stage where returning waves encounter with foreword waves, the gravitational waves are deformed to standing waves that carry no energy outside of the event horizon. We conclude that no gravitational wave is radiated from the SMBHB.

9. Conclusion

By the observation of the DRWPs (decameter radio wave pulses) it is concluded that SgrA* consists of SMBHB (super massive black hole binary) with member BHs Gaa (temporally called with mass of (2.27±0.02)×10^6 M$_\odot$) and Gab (temporally called with mass of (1.94±0.01)×10^6 M$_\odot$) whose orbital velocities are 18% and 22% of the light velocity, respectively. The two black holes orbit at a distance around 4.1 ×10^{7}km and a period of 2200±50 sec. These parameters seem extraordinary from a typical celestial dynamics perspective; hence, we call this binary system an extreme SMBHB. After publication [8], this result was investigated by comparing it with the VLBI results observed via 1.3 mm-radio-waves for Sgr A*. By comparing these against the DRWP-Model constructed as a source of the 1.3 mm radio-wave emissions to reflect the radiation environment of the existing SMBHB, we find that the VSCAT (variation with short characteristic time) observed by 1.3 mm VLBI by Fish et al in 2009 [5] coincides with the DRWP-Model giving an orbital period of 2150±2.5sec.

Based on this background, the presence of an extreme SMBHB, as concluded by the DRWP observations, is further supported in the present study by using public data from the EHT where the full visibility data with timing, baseline length given by u, and v coordinate, amplitude and phase of visibility, together with sigma of observed values are listed both for observations on April 6 and April 7, in 2017. The data consist of high(229.1 GHz) and low (227.1GHz) observation frequencies observed by 8 antennas located at worldwide distributed stations are correlated to obtain the visibility data through two data handling pipelines rPICARD (CASA) and HOPS. Then we were able to use eight kind of visibility data from each pair of observation stations which make 24 pairs in total.

In the present study we did not use the visibility data as regular usages which have been originally planned for observation by the EHT; that is, instead to form the static map of radio wave emission sources we tried to find the time variations of the radio wave sources. From this perspective, we investigated the data observed by each baseline individually, rather than using as ensemble to form so called the dirty map.

To investigate the time variation, we morphologically categorized the EHT visibility data according to the observation baseline length; these are , the case of short baseline whose length is shorter than 3 Gλ, the case of medium baseline whose length is in a range from 3 Gλ to 6 Gλ , and long baseline whose length is longer than 6 Gλ. In the case of the short baseline, most visibilities exhibit long characteristic time variations with large amplitudes (of the order of Jy) and show discrete forms via the time passage; the associated short time period (of less than an hour) is only fractional. The morphological features of the EHT data change dramatically in the medium length baseline catego-

ry, where the data oscillate with P-P amplitudes below 2 Jy; we call this feature of the visibility the "spreading type visibility." The EHT report [33] indicates the existence of some systematic oscillation; however, principal understanding [33,34] concludes that the time variations are the random noises associated with intrinsic and stochastically stationary levels of emission from sources around Sgr A*, except for the orbital motion of the hot spot in the magnetized plasma.

Independently of the EHTC approach, we consider the oscillatory visibility of the VLBI EHT data to be a mixture of random noise and radio-wave emissions closely related to the orbital motions associated with existing SMBHBs. Owing to an orbit size of 4.1×10^7 km that is determined by DRWP observations, the observation for a baseline length of ~3 Gλ starts to show a correlated signal to be emitted from the area of orbiting SMBHB motions (SMBHB signal) when we estimate the distance of Sgr A* to be 8.3 kpc from the Earth. Through a morphological study for the cases of medium and long baselines, we roughly estimated the ratio of the SMBHB signal to random noise is to be a range about from 0.5 to 6.

For the confirmation of the existing SMBHB signal we made the model of the SMBHB signal, based on the parameters concluded from DRWP observations, that is detectable by 1.3mm wavelength VLBI of EHT; the model is called DRWP-Model through out present study. The direct comparisons between EHT observation data (EHT-Data) and DRWP-Model were made for three example cases of AP-SM, AZ-SP and SM-SP baselines of Hi CASA for 96-days observation. Within mixture state of SMBHB signal and random noise there appeared apparent components in EHT-Data which coincide with the DRWP-Model. Furthermore, we determined the unknown geometric parameter for SMBHB orbits in the constructed model, from the processes to find coincidences between the EHT-Data and DRWP-Model; that is, the orbital plane of the SMBHB was clarified as parallel to the Galactic plane with a margin of ±3° in the direction perpendicular to the Earth–Sgr A* line. In the direction of the Earth-SgrA* line there is tilt of the orbital plane by ±6° as has already been decided [17]. Though the direct comparisons of EHT-Data and DRWP-Model indicated apparent coincidence suggesting the existence of SMBHB, we took the process as a pilot role to confirm exact existence of the SMBHB, because we could not eliminate the disturbances of coexisting large fraction of random noise ,in the case of the direct comparison. Furthermore, EHT-Data have been sampled with unique DSTW (data sampling time window) with pauses of quasi periodic intervals around 1000 to 1100 sec. The DSTWs interfere with the direct comparison, especially when clarifying the existing periodic variation of the VSCAT.

Principal tasks to find the coincidences between EHT-Data and DRWP-Model (FCED) were carried out by utilizing the MDFT (Modified Fourier Transformation). In the present study it was clarified that in the case of usage of simple transformation of the EHT-Data, results were affected by DSTW as convolution of spectra of DSTW , S(ω) (as function of $\omega = 2\pi/T$ for analyzing period T). By applying the Fourier transformation to time series of random noises sampled with DSTW of EHT which are called

QRN-EHT (Quasi Random signal sampled with timing of EHT observation), we obtained S(ω). The MDFT was defined as Fourier transformed function divided by S(ω). Thus we compared the MDFT for EHT-Data and MDFT for DRWP-Model.

The MDFT method has two advantages. (1) It separates the random noise component from the observed EHT-Data. (2) The MDFTs for DRWP-Model reveals features that are extremely sensitive to the orbiting period of the SMBHB; thus, we were able to accurately select possible orbiting periods by finding the coincidence with the EHT-Data. In the present study, we showed real processes for managing FCED, utilizing the MDFTs for the EHT-Data and for DRWP-Model. The EHT-Data for FCED were selected as first step from Day 96 SM-SP Hi-CASA and Day 97 AZ-SP Hi-HOPS which belong to the category of the long baseline; and for Day 96 AZ-SM Hi HOPS and Day 97 LM-SM Hi CASA as medium baseline. By searching the orbital periods of possible SMBHBs in the period range 2100–2245 sec, we obtained the periods for the above data from the SM-SP, AZ-SP, AZ-SM, and LM-SM baselines, as 2190, 2180, 2125, and 2210 sec, respectively. To confirm that the variation of the resulting period is not real variation but a stochastic ambiguity attributable to existing noise, we analyzed all eight possible data for each baseline corresponding to SM-SP, AZ-SP, and LM-SM; and we averaged over the all 24 results obtained by applying the MDFT method. Thus obtained results give the orbital period of SMBHB to be 2193.3 sec with the standard deviation of 27.5 sec. We are able to state that time variations revealed by VLBI observation data of Sgr A* in the 2017 EHT campaign exhibit a periodicity whose period coincides with the presence of an extreme SMBHB within the error limit at Sgr A*, where a SMBHB orbits with a period of 2200 ± 50 sec and distance 4.1×10^7 km in the plane nearly parallel to the Galactic equatorial plane; we do not repeat the other already determined parameters for the SMBHB, instead referring to the foregoing publications [8,17].

Acknowledgement

References
1. Zhao, J. H., Young, K. H., Herrnstein, R. M., Ho, P. T. P., Tsutsumi, T., Lo, K. Y., ... & Bower, G. C. (2003). Variability of Sagittarius A*: Flares at 1 millimeter. The Astrophysical Journal, 586(1), L29.
2. Miyazaki, A., Tsutsumi, T., & Tsuboi, M. (2004). Intraday variation of Sagittarius A* at short millimeter wavelengths. The Astrophysical Journal, 611(2), L97.
3. Eckart, A., Schödel, Q. R., García-Marín, M., Witzel, G., Weiss, A., Baganoff, F. K., ... & Zensus, J. A. (2008). Simultaneous NIR/sub-mm observation of flare emission from Sagittarius A. Astronomy & Astrophysics, 492(2), 337-344.
4. Marrone, D. P., Baganoff, F. K., Morris, M. R., Moran, J. M.,

Ghez, A. M., Hornstein, S. D., ... & Bower, G. C. (2008). An x-ray, infrared, and submillimeter flare of Sagittarius A. The Astrophysical Journal, 682(1), 373.

5. Fish, V. L., Doeleman, S. S., Beaudoin, C., Blundell, R., Bolin, D. E., Bower, G. C., ... & Ziurys, L. M. (2011). The 1.3 mm wavelength VLBI of Sagittarius A*: Detection of time-variable emission on event horizon scales. The Astrophysical Journal Letters, 727(2), L36.

6. Fish, V. L., Johnson, M. D., Doeleman, S. S., Broderick, A. E., Psaltis, D., Lu, R. S., ... & Ziurys, L. M. (2016). Persistent asymmetric structure of Sagittarius A* on event horizon scales. The Astrophysical Journal, 820(2), 90.

7. Miyoshi, M., Shen, Z. Q., Oyama, T., Takahashi, R., & Kato, Y. (2011). Oscillation phenomena in the disk around the massive black hole Sagittarius A*. Publications of the Astronomical Society of Japan, 63(5), 1093-1116.

8. Oya, H. (2019). detection of decameter radio wave pulses from the center part of our galaxy suggesting sources at rotating super massive black hole binary. TERRAPUB e-Library, 1-50. http://hdl.handle.net/10097/00126480

9. Storey, L. R. O. (1953). An investigation of whistling atmospherics. Philosophical Transactions of the Royal Society of London. Series A, Mathematical and Physical Sciences, 246(908), 113-141.

10. Bell, T. F., & Buneman, O. (1964). Plasma instability in the whistler mode caused by a gyrating electron stream. Physical Review, 133(5A), A1300.

11. Brice, N. (1964). Fundamentals of very low frequency emission generation mechanisms. Journal of Geophysical Research, 69(21), 4515-4522.

12. Kennel, C. F., & Petschek, H. E. (1966). Limit on stably trapped particle fluxes. Journal of Geophysical Research, 71(1), 1-28.

13. Gurnett, D. A., & Frank, L. A. (1972). VLF hiss and related plasma observations in the polar magnetosphere. Journal of Geophysical Research, 77(1), 172-190.

14. Helliwell, R.A. (1997). Whistler, Discovery of the magnetosphere, Series: History of Geophysics ,Edited by Gillmor, C.S. & Spreiter ,J.R., Vol 7, pp 83.

15. Demekhov, A. G. (2011). Generation of VLF emissions with the increasing and decreasing frequency in the magnetosperic cyclotron maser in the backward wave oscillator regime. Radiophysics and Quantum Electronics, 53(11), 609-622.

16. Oya, H. (2023). No gravitational wave from orbiting Supermassive Kerr black hole—a model of matter distribution and propagation of gravitational waves inside the event horizon. Eart & Envi Scie Res & Rev, 6(1), 278-332.

17. Oya, H. (2022). Interpretation of time-varying radio emissions of SgrA* observed by 1.3 Millimeter-Wavelength VLBI---with parameters of The super-massive black Hole binary at SgrA* based on decameter radio wave pulse observations, Eart & Envi Scie Res & Rev.5(4) ,185-216.

18. Gillessen, S., Plewa, P. M., Eisenhauer, F., Sari, R. E., Waisberg, I., Habibi, M., ... & Genzel, R. (2017). An update on monitoring stellar orbits in the galactic center. The Astrophysical Journal, 837(1), 30.

19. Akiyama,K., Alberdi, A. Alef,W., Asada, K., Azulay,R ,Baczko,A.-K.,Ball,D.,Baloković,M.,Barrett,J.,Bintley,D.….& Ziurys, L. (2019). First M87 Event Horizon Telescope Results. I:The Shadow of the Supermassive Black Hole, The Astrophysical Journal Letters. 875,L1

20. Akiyama,K., Alberdi, A. Alef,W., Asada, K., Azulay,R ,Baczko,A.-K.,Ball,D.,Baloković,M.,Barrett,J.,Bintley,D.,…& Ziurys,L.(2019). First M87 Event Horizon Telescope Results. II: Array and Instrumentation, The Astrophysical Journal Letters, 875,L2

21. Akiyama,K., Alberdi, A. Alef,W., Asada, K., Azulay,R ,Baczko,A.-K.,Ball,D.,Baloković,M.,Barrett,J.,Bintley,D.,…& Yamaguchi,P. (2019). First M87 Event Horizon Telescope Results. III. Data Processing and Calibration,The Astrophysical Journal Letters, 875,L3

22. Akiyama, K., Alberdi, A., Alef, W., Asada, K., Azulay, R., Baczko, A. K., ... & Yamaguti, P. (2019). First M87 event horizon telescope results. IV. Imaging the central supermassive black hole. The Astrophysical Journal Letters, 875(1), L4.

23. Akiyama, K., Alberdi, A., Alef, W., Asada, K., Azulay, R., Baczko, A. K., ... & Zhang, S. (2019). First M87 event horizon telescope results. V. Physical origin of the asymmetric ring. The Astrophysical Journal Letters, 875(1), L5.

24. Akiyama, K., Alberdi, A., Alef, W., Asada, K., Azulay, R., Baczko, A. K., ... & Yamaguti, P. (2019). First M87 event horizon telescope results. VI. The shadow and mass of the central black hole. The Astrophysical Journal Letters, 875(1), L6.

25. Akiyama,K.,Alberdi,A.,Algaba,J.C.,Anantua,R., Asada, K.,Azulay,R.,Bach,U., Baczko ,A-K.,Mislav Baloković,M., John Barrett, J.….& Zeballos,M.(2022) First Sagittarius A* Event Horizon Telescope Results. I. The Shadow of the Supermassive Black Hole in the Center of the Milky Way, The Astrophysical Journal Letters, 930, L12

26. Akiyama, K., Alberdi, A., Alef, W., Algaba, J. C., Anantua, R., Asada, K., ... & Wouterloot, J.G.A. (2022). First Sagittarius A* event horizon telescope results. II. EHT and multiwavelength observations, data processing, and calibration. The Astrophysical Journal Letters, 930(2), L13.

27. Akiyama, K., Alberdi, A., Alef, W., Algaba, J. C., Anantua, R., Asada, K., ... & Zhao, S-S. (2022). First Sagittarius A* event horizon telescope results. III. Imaging of the galactic center supermassive black hole. The Astrophysical Journal Letters, 930(2), L14.

28. Akiyama, K., Alberdi, A., Alef, W., Algaba, J. C., Anantua, R., Asada, K., ... & Chang,D.O. (2022). First Sagittarius A* Event Horizon Telescope results. IV. Variability, morphology, and black hole mass. The Astrophysical Journal Letters, 930(2), L15.

29. Akiyama, K., Alberdi, A., Alef, W., Algaba, J. C., Anantua, R., Asada, K., ... & White, C. (2022). First Sagittarius A* event horizon telescope results. V. Testing astrophysical models of the galactic center black hole. The Astrophysical Journal Letters, 930(2), L16.

30. Akiyama, K., Alberdi, A., Alef, W., Algaba, J. C., Anantua, R., Asada, K., ... & Zhao, S-S. (2022). First Sagittarius A* event horizon telescope results. VI. Testing the black hole metric. The Astrophysical Journal Letters, 930(2), L17.

31. Miyoshi, M., Kato, Y., & Makino, J. (2022). The Jet and Resolved Features of the Central Supermassive Black Hole of M87 Observed with the Event Horizon Telescope (EHT). The Astrophysical Journal, 933(1), 36.

32. Fish, V. L., Johnson, M. D., Lu, R. S., Doeleman, S. S., Bou-

man, K. L., Zoran, D., ... & Vertatschitsch, L. E. (2014). Imaging an event horizon: mitigation of scattering toward Sagittarius A*. The Astrophysical Journal, 795(2), 134.

33. Wielgus, M., Marchili, N., Martí-Vidal, I., Keating, G. K., Ramakrishnan, V., Tiede, P., ... & Zhao, S-S. (2022). Millimeter Light Curves of Sagittarius A* Observed during the 2017 Event Horizon Telescope Campaign. The Astrophysical Journal Letters, 930(2), L19.

34. Wielgus, M., Moscibrodzka, M., Vos, J., Gelles, Z., Martí-Vidal, I., Farah, J., ... & Messias, H. (2022). Orbital motion near Sagittarius A*-Constraints from polarimetric ALMA ob-

servations. Astronomy & Astrophysics, 665, L6.

35. Event Horizon Telescope Collaboration. (2022). First Sagittarius A* Event Horizon Telescope results. Calibrated Data, Doi:10.25739/m140-ct59;

36. Eckart, A., Zajacek, M., Parsa, M., Fazeli, E. H. N., Busch, G., Shahzamanian, B., ... & Kamali, F. (2018). The Multifrequency Behavior of Sagittarius A*. arXiv preprint arXiv:1806.00284.

37. Landau, L. D., & Lifshitz, E. M. (1967). The Classical Theory of Fields Third Revised English Edition Course of Theoretical Physics, Pergamon Press, Oxford, New York, p325.

Appendix A

When we select INCL as first step in main text, we define a new Cartesian coordinate (x_6, y_6, z_6) with corresponding unit vectors ($\hat{x}_6, \hat{y}_6, \hat{z}_6$) to form system which can be obtained by the INCL process with inclination angle β (=6°). That is, corresponding to eqs. from (16) to (18) we have the relations, as

$$\hat{x}_6 = cos\beta\, \hat{x} + sin\beta\hat{z}, \qquad (A1-1)$$

$$\hat{y}_6 = \hat{y}, \qquad (A1-2)$$

$$\hat{z}_6 = -sin\beta\hat{x} + cos\beta\hat{z}. \qquad (A1-3)$$

Thus, we have relations between the Cartesian coordinate (x_{p2}, y_{p2}, z_{p2}) with corresponding unit vector $\hat{x}_{p2}, \hat{y}_{p2}$, and $\hat{z}_{p2}$ taking the ROTE step with rotation angle $\pm\alpha$. That is, unit vectors are given by

$$\hat{x}_{p2} = \hat{x}_6, \qquad (A2-1)$$

$$\hat{y}_{p2} = cos\alpha\, \hat{y}_6 - sin\alpha\hat{z}_6 \qquad (A2-2)$$

$$\hat{z}_{p2} = sin\alpha\, \hat{y}_6 + cos\alpha\hat{z}_6. \qquad (A2-3)$$

Then results are given by

$$\hat{x}_{p2} = cos\beta\, \hat{x} + sin\beta\hat{z} \qquad (A3-1)$$

$$\hat{y}_{p2} = sin\alpha\cdot sin\beta\hat{x} + cos\alpha\hat{y} - sin\alpha\cdot cos\beta\hat{z}. \qquad (A3-2)$$

$$\hat{z}_{p2} = -cos\alpha\cdot sin\beta\hat{x} + sin\alpha\hat{y} + cos\alpha\cdot cos\beta\hat{z}. \qquad (A3-3)$$

For comparison we repeat eqs from (20) to (22) as

$$\hat{x}_p = cos\beta\hat{x} + sin\alpha\cdot sin\beta\, \hat{y} + cos\alpha\cdot sin\beta\hat{z}. \qquad (A4-1)$$

$$\hat{y}_p = cos\alpha\, \hat{y} - sin\alpha\hat{z}. \qquad (A4-2)$$

$$\hat{z}_p = -sin\beta\hat{x} + sin\alpha\cdot cos\beta\, \hat{y} + cos\alpha\cdot cos\beta\hat{z}. \qquad (A4-3)$$

When we consider the α and β ranges less than 10° we have approximated relations with errors less than 3 %, as

$$\hat{x}_{p2} - \hat{x}_p \approx 0 \qquad (A5-1)$$

$$\hat{y}_{p2} - \hat{y}_p \approx 0 \qquad (A5-2)$$

$$\hat{z}_{p2} - \hat{z}_p \approx 0 \qquad (A5-3)$$

Then we can use eqs from (20) to (22) in main text as one of general expression in so far as small angle approximation for α and β.

By using eqs. (13), (14) and (15), also in main text, the real orbital plane of the SMBHB can be expressed with the coordinate system given by eqs. from (20) to (22) that can be expressed in the earth equatorial and the spring equinox coordinate with the unit vectors ($\hat{x}_e, \hat{y}_e, \hat{z}_e$) as belows:

$$
\begin{aligned}
\hat{x}_p = &cos\beta\big(cos\delta_{Sg}cos\phi_{Sg}\hat{x}_e + cos\delta_{Sg}sin\phi_{Sg}\hat{y}_e + sin\delta_{Sg}\hat{z}_e\big)\\
&+ sin\alpha\cdot sin\beta\big[(cos\delta_{Gp}sin\delta_{Sg}sin\phi_{Gp} - cos\delta_{Sg}sin\delta_{Gp}sin\phi_{Sg})\hat{x}_e\\
&+ (cos\delta_{Sg}sin\delta_{Gp}cos\phi_{Sg} - sin\delta_{Sg}cos\delta_{Gp}cos\phi_{Gp})\hat{y}_e\\
&+ (cos\delta_{Sg}sin\phi_{Sg}cos\delta_{Gp}cos\phi_{Gp} - cos\delta_{Sg}cos\phi_{Sg}cos\delta_{Gp}sin\phi_{Gp})\hat{z}_e\big]\\
&+ cos\alpha\cdot sin\beta\big[cos\delta_{Gp}cos\alpha_{GP}\hat{x}_e + cos\delta_{Gp}sin\alpha_{GP}\hat{y}_e + sin\delta_{GP}\hat{z}_e\big]
\end{aligned}
$$

$$=[cos\beta\ cos\delta_{Sg}cos\phi_{Sg} + sin\alpha \cdot sin\beta(cos\delta_{Gp}sin\delta_{Sg}sin\phi_{Gp} - cos\delta_{Sg}sin\delta_{Gp}sin\phi_{Sg}) + cos\alpha$$
$$.\ sin\beta cos\delta_{Gp}cos\alpha_{GP}]\hat{x}_e$$
$$+[\ cos\beta cos\delta_{Sg}sin\phi_{Sg} + sin\alpha sin\beta(cos\delta_{Sg}sin\delta_{Gp}cos\phi_{Sg} - sin\delta_{Sg}cos\delta_{Gp}cos\phi_{Gp}) + cos\alpha$$
$$.\ sin\beta cos\delta_{GP}sin\alpha_{GP}]\hat{y}_e$$
$$+[cos\beta sin\delta_{Sg} + \quad sin\alpha \cdot$$
$$sin\beta(cos\delta_{Sg}sin\phi_{Sg}cos\delta_{Gp}cos\phi_{Gp} - cos\delta_{Sg}cos\phi_{Sg}cos\delta_{Gp}sin\phi_{Gp}) + cos\alpha \cdot$$
$$sin\beta sin\delta_{GP}]\hat{z}_e \qquad\qquad (A6)$$

and

$$\hat{y}_p = cos\alpha[(cos\delta_{Gp}sin\delta_{Sg}sin\phi_{Gp} - cos\delta_{Sg}sin\delta_{Gp}sin\phi_{Sg})\hat{x}_e$$
$$+ (cos\delta_{Sg}sin\delta_{Gp}cos\phi_{Sg} - sin\delta_{Sg}cos\delta_{Gp}cos\phi_{Gp})\hat{y}_e$$
$$+ (cos\delta_{Sg}sin\phi_{Sg}cos\delta_{Gp}cos\phi_{Gp} - cos\delta_{Sg}cos\phi_{Sg}cos\delta_{Gp}sin\phi_{Gp})\hat{z}_e]$$
$$- sin\alpha[cos\delta_{Gp}cos\alpha_{GP}\hat{x}_e + cos\delta_{GP}sin\alpha_{GP}\hat{y}_e$$
$$+ sin\delta_{GP}\hat{z}_e],$$
$$= [cos\alpha \cdot (cos\delta_{Gp}sin\delta_{Sg}sin\phi_{Gp} - cos\delta_{Sg}sin\delta_{Gp}sin\phi_{Sg}) - sin\alpha cos\delta_{Gp}cos\alpha_{GP}]\ \hat{x}_e$$
$$+[cos\alpha \cdot (cos\delta_{Sg}sin\delta_{Gp}cos\phi_{Sg} - sin\delta_{Sg}cos\delta_{Gp}cos\phi_{Gp}) - sin\alpha \cdot cos\delta_{GP}sin\alpha_{GP}]\hat{y}_e$$
$$+[cos\alpha \cdot (cos\delta_{Sg}sin\phi_{Sg}cos\delta_{Gp}cos\phi_{Gp} - cos\delta_{Sg}cos\phi_{Sg}cos\delta_{Gp}sin\phi_{Gp}) - sin\alpha \cdot sin\delta_{GP}]\hat{z}_e$$
$$\qquad\qquad (A7)$$

We define here new coefficients for $\hat{x}_p$, as

$$\hat{x}_p = A_x\hat{x}_e + A_y\hat{y}_e + A_z\hat{z}_e. \qquad\qquad (A8)$$

where

$$A_x = cos\beta\ cos\delta_{Sg}cos\phi_{Sg} + sin\alpha \cdot sin\beta(cos\delta_{Gp}sin\delta_{Sg}sin\phi_{Gp} - cos\delta_{Sg}sin\delta_{Gp}sin\phi_{Sg}) + cos\alpha .$$
$$sin\beta cos\delta_{Gp}cos\alpha_{GP}, \qquad\qquad (A8\text{-}1)$$
$$A_y = cos\beta cos\delta_{Sg}sin\phi_{Sg} + sin\alpha sin\beta(cos\delta_{Sg}sin\delta_{Gp}cos\phi_{Sg} - sin\delta_{Sg}cos\delta_{Gp}cos\phi_{Gp}) + cos\alpha .$$
$$sin\beta cos\delta_{GP}sin\alpha_{GP} \quad , \qquad\qquad (A8-2)$$
$$A_Z = cos\beta sin\delta_{Sg} + \ sin\alpha\ sin\beta(cos\delta_{Sg}sin\phi_{Sg}cos\delta_{Gp}cos\phi_{Gp} - cos\delta_{Sg}cos\phi_{Sg}cos\delta_{Gp}sin\phi_{Gp})$$
$$+ cos\alpha \cdot sin\beta sin\delta_{GP}, \qquad\qquad (A8\text{-}3)$$

; and for $\hat{y}_p$,as

$$\hat{y}_p = B_x\hat{x}_e + B_y\hat{y}_e + B_z\hat{z}_e. \qquad\qquad (A9)$$

where

$$B_x = cos\alpha \cdot (cos\delta_{Gp}sin\delta_{Sg}sin\phi_{Gp} - cos\delta_{Sg}sin\delta_{Gp}sin\phi_{Sg}) - sin\alpha cos\delta_{Gp}cos\alpha_{GP} \quad , \qquad (A9-1)$$
$$B_y = cos\alpha \cdot (cos\delta_{Sg}sin\delta_{Gp}cos\phi_{Sg} - sin\delta_{Sg}cos\delta_{Gp}cos\phi_{Gp}) - sin\alpha \cdot cos\delta_{GP}sin\alpha_{GP} \quad , \quad (A9-2)$$

and

$$B_z = cos\alpha \cdot (cos\delta_{Sg}sin\phi_{Sg}cos\delta_{Gp}cos\phi_{Gp} - cos\delta_{Sg}cos\phi_{Sg}cos\delta_{Gp}sin\phi_{Gp}) - sin\alpha sin\delta_{GP}.$$
$$\qquad\qquad (A9\text{-}3)$$

Corresponding to the phase function $\Delta \boldsymbol{k}_{rot} \cdot (\boldsymbol{r}_m - \boldsymbol{r}_n)$ that is expressed by taking j in eq.(4) in main text as "Orb" meaning by orbits range of the SMBHB is given by

$$\Delta \boldsymbol{k}_{Orb} = (2\pi/\lambda)(L_{Orb}./L_{Sg}) \cdot (\hat{k}_1 + \kappa_r \hat{k}_2). \qquad\qquad (A10)$$

where $\hat{k}_1$ and $\hat{k}_2$ are unit vectors which rotate with orbiting angular velocities Ω_{Orb} and $2\Omega_{Orb}$ respectively, forming a bar connecting geometry between SMBH Gaa and Gab that results ecliptic effects at observation points; κ_r is a rate for giving the weight to eclipse effect compared with effects of spectra modulation due to the Doppler effects.

Then two unit vectors are expressed by

$$\hat{k}_1 = cos(\Omega_{Orb}t + \varphi_{Orb})\hat{x}_p + sin(\Omega_{Orb}t + \varphi_{Orb})\hat{y}_p . \qquad (A11)$$

and

$$\hat{k}_2 = cos(2\Omega_{Orb}t + \varphi_{Orb})\hat{x}_p + sin(2\Omega_{Orb}t + \varphi_{Orb})\hat{y}_p . \qquad (A12)$$

Then $\hat{k}_1 + \kappa_r\hat{k}_2$ terms that is essential to describe $\Delta\boldsymbol{k}_{Orb}$ as given by eq.(A 10) is expressed by

$$
\begin{aligned}
\hat{k}_1 + \kappa_r\hat{k}_2 = \{&[cos(\Omega_{Orb}t + \varphi_{Orb}) + \kappa_r cos(2\Omega_{Orb}t + \varphi_{Orb})]A_x \\
&+ [sin(\Omega_{Orb}t + \varphi_{Orb}) + \kappa_r sin(2\Omega_{Orb}t + \varphi_{Orb})]B_x\}\hat{x}_e \\
&+ \{[cos(\Omega_{Orb}t + \varphi_{Orb}) + \kappa_r cos(2\Omega_{Orb}t + \varphi_{Orb})]A_y \\
&+ [sin(\Omega_{Orb}t + \varphi_{Orb}) + \kappa_r sin(2\Omega_{Orb}t + \varphi_{Orb})]B_y\}\hat{y}_e \\
&+ \{[cos(\Omega_{Orb}t + \varphi_{Orb}) + \kappa_r cos(2\Omega_{Orb}t + \varphi_{Orb})]A_z \\
&+ [sin(\Omega_{Orb}t + \varphi_{Orb}) + \kappa_r sin(2\Omega_{Orb}t + \varphi_{Orb})]B_z\}\hat{z}_e
\end{aligned}
$$
$$(A13)$$

Appendix B

We start the mathematical manipulation with the phase function given in the main text by repeating here as

$$\mathcal{F} = cos\Theta . \qquad (B1)$$

with

$$\Theta = 2\pi\frac{L_{Orb}}{L_{Sg}}\left(\hat{k}_1 + \kappa_r\hat{k}_2\right) \cdot \frac{(\boldsymbol{r}_m - \boldsymbol{r}_n)}{\lambda} . \qquad (B2)$$

We also repeat $\boldsymbol{r}_m - \boldsymbol{r}_n$ vector given as eq.(29) in main text by referring the explanation of all symbols in equation to the main text, as

$$
\begin{aligned}
\boldsymbol{r}_m - \boldsymbol{r}_n = &\{(r_e + h_m)cos\delta_m cos[\Omega_e(t - t_0) + \phi_m] - (r_e + h_n)cos\delta_n cos[\Omega_e(t - t_0) + \phi_n]\}\hat{x}_e \\
&+\{(r_e + h_m)cos\delta_m sin[\Omega_e(t - t_0) + \phi_m] - (r_e + h_n)cos\delta_n sin[\Omega_e(t - t_0) + \phi_n]\}\hat{y}_e \\
&+[(r_e + h_m)sin\delta_m - (r_e + h_n)sin\delta_n]\hat{z}_e, \qquad (B3)
\end{aligned}
$$

From the standing point to investigate the time depending characteristic of the visibility of VLBI, we approximate the level of the observatory as

$$r_e \gg h_m . \qquad (B4)$$

Then eq.(B 3) is rewritten by

$$
\begin{aligned}
\boldsymbol{r}_m - \boldsymbol{r}_n = &r_e[(cos\delta_m cos\phi_m - cos\delta_n cos\phi_n)cos\Omega_e\tau - (cos\delta_m sin\phi_m - cos\delta_n sin\phi_n)sin\Omega_e\tau]\hat{x}_e \\
&+r_e[(cos\delta_m cos\phi_m - cos\delta_n cos\phi_n)sin\Omega_e\tau + (cos\delta_m sin\phi_m - cos\delta_n sin\phi_n)cos\Omega_e\tau]\hat{y}_e \\
&+r_e[sin\delta_m - sin\delta_n]\hat{z}_e \qquad (B5)
\end{aligned}
$$

By defining C_{mn} and D_{mn} as

$$C_{mn} = cos\delta_m cos\phi_m - cos\delta_n cos\phi_n , \qquad (B6)$$

and

$$D_{mn} = cos\delta_m sin\phi_m - cos\delta_n sin\phi_n , \qquad (B7)$$

$$\boldsymbol{r}_m - \boldsymbol{r}_n = r_e[C_{mn}cos\Omega_e\tau - D_{mn}sin\Omega_e\tau]\hat{x}_e$$

$$+r_e[C_{mn}sin\Omega_e\tau + D_{mn}cos\Omega_e\tau]\hat{y}_e$$

$$+r_e[sin\delta_m - sin\delta_n]\hat{z}_e \qquad (B8)$$

The phase Θ in eq.(B 1) is expressed with eq.(B 5) and eq.(A 12) in Appendix A , as

$$\Theta = 2\pi\frac{L_{Orb}}{L_{Sg}}\cdot\frac{r_e}{\lambda}\{[cos(\Omega_{Orb}t + \varphi_{Orb}) + \kappa_r cos(2\Omega_{Orb}t + \varphi_{Orb})](C_{mn}cos\Omega_e\tau - D_{mn}sin\Omega_e\tau)A_x$$

$$+[sin(\Omega_{Orb}t + \varphi_{Orb}) + \kappa_r sin(2\Omega_{Orb}t + \varphi_{Orb})](C_{mn}cos\Omega_e\tau - D_{mn}sin\Omega_e\tau)B_x$$

$$+[cos(\Omega_{Orb}t + \varphi_{Orb}) + \kappa_r cos(2\Omega_{Orb}t + \varphi_{Orb})](C_{mn}sin\Omega_e\tau + D_{mn}cos\Omega_e\tau)A_y$$

$$+[sin(\Omega_{Orb}t + \varphi_{Orb}) + \kappa_r sin(2\Omega_{Orb}t + \varphi_{Orb})](C_{mn}sin\Omega_e\tau + D_{mn}cos\Omega_e\tau)B_y$$

$$+[cos(\Omega_{Orb}t + \varphi_{Orb}) + \kappa_r cos(2\Omega_{Orb}t + \varphi_{Orb})](sin\delta_m - sin\delta_n)A_z$$

$$+[sin(\Omega_{Orb}t + \varphi_{Orb}) + \kappa_r sin(2\Omega_{Orb}t + \varphi_{Orb})](sin\delta_m - sin\delta_n)B_z \quad (B9)$$

Taking the mathematical manipulation eq.(B 6) is further rewritten as

$$\Theta = 2\pi\frac{L_{Orb}}{L_{Sg}}\cdot\frac{r_e}{\lambda}\{[cos(\Omega_{Orb}\tau + \xi_{Orb})cos\Omega_e\tau + \kappa_r cos(2\Omega_{Orb}\tau + \eta_{Orb})cos\Omega_e\tau]A_x C_{mn}$$

$$-[cos(\Omega_{Orb}\tau + \xi_{Orb})sin\Omega_e\tau + \kappa_r cos(2\Omega_{Orb}\tau + \eta_{Orb})sin\Omega_e\tau]A_x D_{mn}$$

$$+[sin(\Omega_{Orb}\tau + \xi_{Orb})cos\Omega_e\tau + \kappa_r sin(2\Omega_{Orb}\tau + \eta_{Orb})cos\Omega_e\tau]B_x C_{mn}$$

$$-[sin(\Omega_{Orb}\tau + \xi_{Orb})sin\Omega_e\tau + \kappa_r sin(2\Omega_{Orb}\tau + \eta_{Orb})sin\Omega_e\tau]B_x D_{mn}$$

$$+[cos(\Omega_{Orb}\tau + \xi_{Orb})sin\Omega_e\tau + \kappa_r cos(2\Omega_{Orb}\tau + \eta_{Orb})sin\Omega_e\tau]A_y C_{mn}$$

$$+[cos(\Omega_{Orb}\tau + \xi_{Orb})cos\Omega_e\tau + \kappa_r cos(2\Omega_{Orb}\tau + \eta_{Orb})cos\Omega_e\tau]A_y D_{mn}$$

$$+[sin(\Omega_{Orb}\tau + \xi_{Orb})sin\Omega_e\tau + \kappa_r sin(2\Omega_{Orb}\tau + \eta_{Orb})sin\Omega_e\tau]B_y C_{mn}$$

$$+[sin(\Omega_{Orb}\tau + \xi_{Orb})cos\Omega_e\tau + \kappa_r sin(2\Omega_{Orb}\tau + \eta_{Orb})cos\Omega_e\tau]B_y D_{mn}$$

$$+[cos(\Omega_{Orb}\tau + \xi_{Orb}) + \kappa_r cos(2\Omega_{Orb}\tau + \eta_{Orb})](sin\delta_m - sin\delta_n)A_z$$

$$+[sin(\Omega_{Orb}\tau + \xi_{Orb}) + \kappa_r sin(2\Omega_{Orb}\tau + \eta_{Orb})](sin\delta_m - sin\delta_n)B_z \quad (B10)$$

where τ is defined as $\tau = t - t_0$;and ξ_{Orb} and η_{Orb} are defined , respectively as $\xi_{Orb} = \varphi_{Orb} + \Omega_{Orb}t_0$ and $\eta_{Orb} = \varphi_{Orb} + 2\Omega_{Orb}t_0$. Each term in eq,(B 10) consists of product of two sinusoidal functions of arguments $\Omega_{Orb}\tau + \xi_{Orb}$ and $\Omega_e\tau$ or arguments $2\Omega_{Orb}\tau + \eta_{Orb}$ and $\Omega_e\tau$. We can make these products to addition or subtraction of two sinusoidal functions ; for an example the term $cos(\Omega_{Orb}\tau + \xi_{Orb})cos\Omega_e\tau$ at the top of eq. (10) can be written as

$$cos(\Omega_{Orb}\tau + \xi_{Orb})cos\Omega_e\tau = \frac{1}{2}\{cos[(\Omega_{Orb} + \Omega_e)\tau + \xi_{Orb}] + cos[(\Omega_{Orb} - \Omega_e)\tau + \xi_{Orb}]\}. \quad (B11)$$

Then applying the same category of the mathematical manipulation we can rewrite eq.(B 7) to the following form:

$$\Theta = \pi\frac{L_{Orb}}{L_{Sg}}\cdot\frac{r_e}{\lambda}[\![K_c\{cos[(\Omega_{Orb} + \Omega_e)\tau + \xi_{Orb}] + \kappa_r cos[(2\Omega_{Orb} + \Omega_e)\tau + \eta_{Orb}]\}$$

$$+K_s\{sin[(\Omega_{Orb} + \Omega_e)\tau + \xi_{Orb}] + \kappa_r sin[(2\Omega_{Orb} + \Omega_e)\tau + \eta_{Orb}]\}$$

$$+L_c\{cos[(\Omega_{Orb} - \Omega_e)\tau + \xi_{Orb}] + \kappa_r cos[(2\Omega_{Orb} - \Omega_e)\tau + \eta_{Orb}]\}$$

$$+L_s\{sin[(\Omega_{Orb} - \Omega_e)\tau + \xi_{Orb}] + \kappa_r sin[(2\Omega_{Orb} - \Omega_e)\tau + \eta_{Orb}]\}$$

$$+M_c[cos(\Omega_{Orb}\tau + \xi_{Orb}) + \kappa_r cos(2\Omega_{Orb}\tau + \eta_{Orb})]$$

$$+M_s[sin(\Omega_{Orb}\tau + \xi_{Orb}) + \kappa_r sin(2\Omega_{Orb}\tau + \eta_{Orb})]]\!] \qquad (B12)$$

where 6 coefficients $K_c, K_s, L_c,$ L_s, M_c and M_s are given as follows:

$$K_c = [(A_x - B_y)C_{mn} + (A_y + B_x)D_{mn}]$$

$$K_s = [(A_y + B_x)C_{mn} - (A_x - B_y)D_{mn}]$$

$$L_c = \left[(A_x + B_y)C_{mn} + (A_y - B_x)D_{mn} \right]$$

$$L_s = \left[(-A_y + B_x)C_{mn} + (A_x + B_y)D_{mn} \right]$$

$$M_c = (sin\delta_m - sin\delta_n)A_z$$

$$M_s = (sin\delta_m - sin\delta_n)B_z$$

In eq.(B 12) we see 6 pair of the cosine and sine function with angular frequency, $\Omega_{Orb} - \Omega_e$, Ω_{Orb}, $\Omega_{Orb} + \Omega_e$, $2\Omega_{Orb} - \Omega_e$, $2\Omega_{Orb}$, and $2\Omega_{Orb} + \Omega_e$. For these pair of cosine and sine functions we have a sinusoidal function for each as indicated by an example :

$$K_c cos[(\Omega_{Orb} + \Omega_e)\tau + \xi_{Orb}] + K_s sin[(\Omega_{Orb} + \Omega_e)\tau + \xi_{Orb}]$$
$$= \sqrt{K_c^2 + K_s^2} cos[(\Omega_{Orb} + \Omega_e)\tau + \Phi_K]. \qquad (B13)$$

where Φ_K is given by

$$\Phi_{K\xi} = \xi_{Orb} - tan^{-1}\left(\frac{K_s}{K_C}\right)$$

Then by rewriting eq.(B 12) with newly defined 6 coefficients we have the results of Θ as

$$\Theta = \sum_{i=1}^{6} \Theta_i . \qquad (B14)$$

where Θ_i for i from 1 to 6 are given by

$$\Theta_1 = \pi \frac{L_{Orb}}{L_{Sg}} \cdot \frac{r_e}{\lambda} \sqrt{K_c^2 + K_s^2} cos\left[(\Omega_{Orb} + \Omega_e)\tau + \Phi_{K\xi} \right] \qquad (B14-1)$$

$$\Theta_2 = 2\pi \frac{L_{Orb}}{L_{Sg}} \cdot \frac{r_e}{\lambda} \sqrt{M_c^2 + M_s^2} cos\left[\Omega_{Orb}\tau + \Phi_{M\xi} \right] \qquad (E14-2)$$

$$\Theta_3 = \pi \frac{L_{Orb}}{L_{Sg}} \cdot \frac{r_e}{\lambda} \sqrt{L_c^2 + L_s^2} cos\left[(\Omega_{Orb} - \Omega_e)\tau + \Phi_{L\xi} \right] \qquad (B14-3)$$

$$\Theta_4 = \pi \frac{L_{Orb}}{L_{Sg}} \cdot \frac{r_e}{\lambda} \kappa_r \sqrt{K_c^2 + K_s^2} cos\left[(2\Omega_{Orb} - \Omega_e)\tau + \Phi_{K\eta} \right] \qquad (B14-4)$$

$$\Theta_5 = 2\pi \frac{L_{Orb}}{L_{Sg}} \cdot \frac{r_e}{\lambda} \kappa_r \sqrt{M_c^2 + M_s^2} cos\left[2\Omega_{Orb}\tau + \Phi_{M\eta} \right] \qquad (B14-5)$$

$$\Theta_6 = \pi \frac{L_{Orb}}{L_{Sg}} \cdot \frac{r_e}{\lambda} \kappa_r \sqrt{L_c^2 + L_s^2} cos\left[(2\Omega_{Orb} + \Omega_e)\tau + \Phi_{L\eta} \right] \qquad (B14-6)$$

with $\Phi_{K\xi}$, $\Phi_{M\xi}$, $\Phi_{L\xi}$, $\Phi_{K\eta}$, $\Phi_{M\eta}$ and $\Phi_{L\eta}$ which are given below:

$$\Phi_{K\xi} = \xi_{Orb} - tan^{-1}\left(\frac{K_s}{K_C}\right). \qquad (B14-7)$$

$$\Phi_{M\xi} = \xi_{Orb} - tan^{-1}\left(\frac{M_s}{M_C}\right). \qquad (B14-8)$$

$$\Phi_{L\xi} = \xi_{Orb} - tan^{-1}\left(\frac{L_s}{L_C}\right). \qquad (B14-9)$$

$$\Phi_{K\eta} = \eta_{Orb} - tan^{-1}\left(\frac{K_s}{K_C}\right). \qquad (B14-10)$$

$$\Phi_{M\eta} = \eta_{Orb} - tan^{-1}\left(\frac{M_s}{M_C}\right). \qquad (B14-11)$$

and

$$\Phi_{L\eta} = \eta_{Orb} - tan^{-1}\left(\frac{L_S}{L_C}\right). \qquad (B14-12)$$

With these angles defined from eq.(B-1) to eq.(B14-6) then,we can find time dependence of the phase part of the visibility, considering eq.(B14), as

$$cos\Theta = cos(\Theta_1 + \Theta_2 + \Theta_3 + \Theta_4 + \Theta_5 + \Theta_6) \qquad (B15)$$

By defining angle $\Theta_{1k} = \sum_{i=1}^k \Theta_i$ we have the following iteration relation, as

$$cos\Theta_{12} = cos\Theta_2 cos\Theta_1 + sin\Theta_2 sin\Theta_1 \qquad (B16-1C)$$
$$sin\Theta_{12} = sin\Theta_2 cos\Theta_1 + cos\Theta_2 sin\Theta_2 \qquad (B16-1S)$$

$$\cdots\cdots\cdots\cdots\cdots\cdots\cdots\cdots\cdots\cdots\cdots$$

$$cos\Theta_{1k+1} = cos\Theta_{1k} cos\Theta_{k+1} - sin\Theta_{1k} sin\Theta_{k+1} \qquad (B16-kC)$$
$$sin\Theta_{1k+1} = sin\Theta_{1k} cos\Theta_{k+1} + cos\Theta_{1k} sin\Theta_{k+1} \qquad (B16-kS)$$

$$\cdots\cdots\cdots\cdots\cdots\cdots\cdots\cdots\cdots\cdots$$

$$cos\Theta_{16} = cos\Theta_{15} cos\Theta_6 - sin\Theta_{1k} sin\Theta_6 \qquad (B16-6C)$$

Using this relation then,we have relation that consists of individual $cos\Theta_k$ and $sin\Theta_k$ (k=1~6) as given in eq.(36) in main text.

As an example, first, we rewrite $cos\Theta_1$, that is given by eq.(B14-1); that is

$$cos\Theta_1 = cos\left\{\pi\frac{L_{Orb}}{L_{Sg}}\cdot\frac{r_e}{\lambda}\sqrt{K_c^2 + K_s^2}cos\left[(\Omega_{Orb} + \Omega_e)\tau + \Phi_{K\xi}\right]\right\}. \qquad (B17)$$

.

By setting

$$\zeta_1 = \pi\frac{L_{Orb}}{L_{Sg}}\cdot\frac{r_e}{\lambda}\sqrt{K_c^2 + K_s^2}\,, \qquad (B17-1)$$

and

$$\mu_1 = (\Omega_{Orb} + \Omega_e)\tau + \Phi_{K\xi}\,, \qquad (B17-2)$$

$cos\Theta_1$ given by eq. (B13) is rewritten using the Bessel functions as

$$cos\Theta_1 = cos(\zeta_1^B cos\mu_1) = J_0(\zeta_1) - 2J_2(\zeta_1)cos2\mu_1 + 2J_4(\zeta_1)cos4\mu_1 - \cdots\cdots (B18)$$

When we apply the similar expression for Θ_i given by eqs.(B14-1) to (B14-6) as

$$\Theta_i = \zeta_i cos\mu_i\,, \qquad (B19)$$

all member terms in eq.(B15) are expressed by combinations of $cos\Theta_i$ and $sin\Theta_i$ as given in main text are expressed as

$$cos\Theta_i = cos(\zeta_i cos\mu_i) = J_0(\zeta_i) - 2J_2(\zeta_i)cos2\mu_i + 2J_4(\zeta_i)cos4\mu_i - \cdots\cdots (B20)$$

and

$$sin\Theta_i = sin(\zeta_i cos\mu_i) = 2J_1(\zeta_i)cos\mu_i - 2J_3(\zeta_i)cos3\mu_i + \cdots\cdots \qquad (B21)$$

Looking eq.(B 12) together with eqs,(B 20) and B 2 1) we recognize that the time variation of the phase part of the visibility Model of EHT VLBI is extremely complicated subjects where the six basic time varying components with angular frequencies of

$\Omega_{Orb} - \Omega_e$, Ω_{Orb} , $\Omega_{Orb} + \Omega_e$, $2\Omega_{Orb} - \Omega_e$, $2\Omega_{Orb}$,and $2\Omega_{Orb} + \Omega_e$ produce higher harmonics (shorter periods phenomena) and mutually coupled each other.

Appendix C

Corresponding four equations from eqs.(45) to (48) in main text, we rewrite the arguments as

$$u = \alpha_N S_N . \tag{C1}$$

and

$$v = \alpha_N S_S \tag{C2}$$

Considering eq.(48) in main text, eq.(45) is expressed by

$$u + \kappa_e v = 0.35 , \tag{C3}$$

Further, eqs. (46) and (47) are rewritten by

$$xu + v = 7(u + v), \tag{C4}$$

and

$$xu + \kappa_e v = 0.74 . \tag{C5}$$

The signal to noise ratio R_{sp} in the case of AZ-SP baseline observation is then given by

$$R_{sp} = \frac{\kappa_e v}{u} . \tag{C6}$$

Then,by subtracting eq.(C4) from eq.(C5) in each side of the equation we arrive at a set of linear equations for two unknown quantities u and v. That is,

$$u + \kappa_e v = 0.35$$
$$7u + (\kappa_e + 6)v = 0.74 . \tag{C7}$$

Then we have solutions

$$u = \frac{0.065 \cdot \kappa_e - 0.35}{(\kappa_e - 1)} , \tag{C8}$$

and

$$v = \frac{0.285 \cdot \kappa_e}{(\kappa_e - 1)} . \tag{C9}$$

From eq.(C5) then x is obtained as

$$x = \frac{0.74 - \kappa_e v}{u} . \tag{C10}$$

The signal to noise ratio R_{Jc} for the case of the AZ-JC baseline observation is estimated as

$$R_{Jc} = \frac{\kappa_e v}{xu} = \frac{\kappa_e v}{0.74 - \kappa_e v} . \tag{C11}$$

Appendix D

We repeat the core part of MDFT for EHT-Data given by eq.(62) in main text, as

$$\frac{|D(\omega)|}{|S(\omega)|} = \frac{|P_s(\omega) * S(\omega)|}{|D_n(\omega)|/N_L} + A(\omega) + N_L . \qquad (D1)$$

where

$$A(\omega) = \{|P_s(\omega) * S(\omega) + N_L S(\omega)| - (|P_s(\omega) * S(\omega)| + N_L|S(\omega)|)\}/|S(\omega)|$$
$$(D2)$$

In this Appendix, we follow the explanation in main text for all utilized symbols. We also repeat here the current to find the coincidence of the MDFT for EHT-Data and the MDFT for DRWP-Model as given in eq.(65) in main text, as

$$\frac{|D(\omega)|}{|S(\omega)|} - (A(\omega) + N_L) = \frac{|Mod(\omega)|}{|S(\omega)|} . \qquad (D3)$$

Because the level of EHT-Data, amplitude of DRWP-Model and amplitude of QRN-EHT are independently generated quantities, we should adjust the level and amplitudes by multiplying coefficients as possible to be close as each other. Then, we set the two parameters α_D and α_M to achieve eq.(D3) as

$$\frac{|D(\omega)|}{|D_n(\omega)|} - \alpha_D = \alpha_M \frac{|Mod(\omega)|}{|D_n(\omega)|} . \qquad (D4)$$

where

$$\alpha_D = 1 + \overline{A(\omega)}/N_L . \qquad (D5)$$

At this point, we estimate α_D taking averaged value in the concerned ω range and express all quantities normalized by $\overline{D(\omega)}$. Further, for phase functions of $S(\omega)$ given in eq.(58) in main text, we should consider the characteristics of the spectra of the random noise which has all possible phase shift randomly. Then we can understand that $S(\omega)$ that is expressed by the complex quantity can take all phase from 0 to 2π. Therefore it follows, from eq.(D2), that,

$$\frac{\overline{A(\omega)}}{N_L} = \{|\overline{P_s(\omega) * S(\omega)} + N_L\overline{S(\omega)}| - (|\overline{P_s(\omega) * S(\omega)}| + N_L|\overline{S(\omega)}|)\}/(N_L|\overline{S(\omega)}|)$$

$$= \sqrt{\left(\frac{\overline{P_s(\omega) * S(\omega)}}{N_L|\overline{S(\omega)}|}\right)^2 + 1} - \frac{\overline{P_s(\omega) * S(\omega)}}{N_L|\overline{S(\omega)}|} - 1 \qquad (D6)$$

Then from eq.(D5), we have the result of α_D, as

$$\alpha_D = \sqrt{\left(\frac{\overline{P_s(\omega) * S(\omega)}}{N_L|\overline{S(\omega)}|}\right)^2 + 1} - \frac{\overline{P_s(\omega) * S(\omega)}}{N_L|\overline{S(\omega)}|} . \qquad (D7)$$

The results are given in Table 4 in main text where α_D is given versus $\overline{P_s(\omega) * S(\omega)}$ and $N_L|\overline{S(\omega)}|$ normalized by $\overline{D(\omega)}$